Spring 5-15-2021

Magnetic Gradient-Based Magnetic Tweezer System for 3D and Swarm Control of Microswimmer

Xiao Zhang
xiaozhang@smu.edu

MAGNETIC GRADIENT-BASED MAGNETIC TWEEZER SYSTEM FOR 3D AND SWARM CONTROL OF MICROSWIMMER

Approved by:

_____
Prof. Min Jun Kim
Professor of Mechanical Engineering

_____
Prof. Ali Beskok
Professor of Mechanical Engineering

_____
Prof. Paul Krueger
Professor of Mechanical Engineering

_____
Prof. Edmond Richer
Associate Professor of Mechanical Engineering

_____
Prof. Pia Vogel
Professor of Biological Sciences

MAGNETIC GRADIENT-BASED MAGNETIC TWEEZER SYSTEM FOR 3D AND SWARM CONTROL OF MICROSWIMMER

A Dissertation Presented to the Graduate Faculty of the

Lyle School of Engineering

Southern Methodist University

in

Partial Fulfillment of the Requirements

for the degree of

Doctor of Philosophy

with a

Major in Mechanical Engineering

by

Xiao Zhang

B.S., Aircraft Design and Engineering, Northwestern Polytechnical University

M.S., Mechanical Engineering, University of Massachusetts Amherst

May 15, 2021

ACKNOWLEDGMENTS

This work would not have been possible without the guidance, patience, and mentorship of my advisor, Dr. Min Jun Kim, along with his many colleagues in the Department of Mechanical Engineering here at SMU. My deepest appreciation goes to my wife Yang Jie for always being with me with magnificent support. I am also forever grateful to my parents and sister for their love over the last twenty-nine years as I grow up and all the way up to my Ph.D. I would like to thank my committee members: Dr. Ali Beskok, Dr. Edmond Richer, Dr. Paul Krueger and Dr. Pia Vogel for their guidance on my Ph.D. track on both coursework and research. Furthermore, I would like to express my appreciation to all my collaborators across the United States, with special praise to Dr. Hoyeon Kim for all his guidance and help during the first two years in my Ph.D. I would like to thank Southern Methodist University for the excellent research environment it provides. I am also deeply grateful to all my friends in BAST lab: Dr. Louis William Rogowski, Jugal Saharia, Bin Peng, Samuel Sheckman, Dr. Jung Soo Lee, Jiannan Tang, Anuruddha Bhattacharjee, Gokhan Kararsiz, Matthew O'Donohue and everyone else who left an impact on me over the last five years. Finally, I would like to thank all my friends that grew up with me since middle school and those from Northwestern Polytechnical University Soccer Team and Dallas Dragon Soccer Team, you guys remind me to take time to enjoy life on this hard journey and help me build and maintain the spirit of sportsmanship, from which I will benefit for the rest of my life, you all are my friend for life! Without all of you and your combined support, I would not be able to achieve any of this. Thank you all.

Xiao Zhang B.S., Aircraft Design and Engineering, Northwestern Polytechnical University
M.S., Mechanical Engineering, University of Massachusetts Amherst

Magnetic Gradient-Based Magnetic Tweezer System For 3D and Swarm Control of Microswimmer

Advisor: Dr. Min Jun Kim

Doctor of Philosophy conferred May 15, 2021

Dissertation completed April 21, 2021

Microscale manipulation has very promising potential in medical applications such as drug delivery, minimal and invasion surgery. Contactless control is preferable as remote manipulation is necessary for *in vivo* applications. Among different control methods, magnetic power source is more suitable and robust for the applications mentioned above. Presented here is a magnetic tweezer system, which manipulates microscale magnetic particles using magnetic forces created by magnetic field gradient. The proposed system has three advantages: First, force applied by the magnetic tweezer system does not contact with the target object and can be generated in different directions. Second, the magnetic tweezer system can apply strong force to accomplish more operations like cell penetration. Third, magnetic forces can be applied specifically to the magnetic particles as most biological materials are free from magnetic influence. The design, development, simulation, and experiment demonstration are presented, and future work combined with haptics for teleoperation is illustrated, which will be very promising for remote surgery and drug delivery applications. The system introduced in this dissertation is able to achieve a magnetic gradient field

as high as 0.8 T/m and capable of exciting micromanipulation with open/closed loop control in 2D/3D. The integration with haptic interface also allows the magnetic tweezer system to perform more micromanipulation tasks such as dynamic path planning and object transportation through real-time teleoperation.

TABLE OF CONTENTS

LIST OF FIGURES

LIST OF TABLES

This work is dedicated to my family, my friends, and my mentors who helped and guided me to this path. May we all thrive in the unknown future.

CHAPTER 1 INTRODUCTION

Microrobotics is firstly known from the famous speech by Dr. Feynman on his “There is plenty of room at the bottom” [1] speech in 1959 during the APS meeting, where he predicts that an enormous number of technical applications will thrive from this small scale field. Similar concepts also came out in the film industry envisioning the potential in microrobotics industry, such as ‘The Fantastic Voyage,’ ‘Innerspace’ and ‘Big Hero 6. During the past several decades, the rapid development of microfabrication, mechatronics and microscopy made it possible for microrobots in the medical field to evolve into various forms with different actuation mechanisms [2, 3], and the development for medical applications such as cell penetration [4-8], drug delivery [9-19], minimal and almost innocuous invasion surgery [20-24] has since become very promising [25-32].

Micromanipulation mechanisms to control microrobots can be classified as generating an external force [33-35] or applying a rotating control signal to generate magnetic torque [36, 37] to manipulate a target for designated operation. On the microscale, methods to generate force and momentum are limited to optical, mechanical, electrical, and magnetic methods, with developed applications such as photonic force microscopy (PFM), electromagnetic coils, microcantilevers in atomic force microscopy (AFM), optical tweezers, and magnetic tweezers being widely utilized in the fields of microrobots, biophysics and cell biology [34, 36, 38-43].

AFM requires the use of a probe having direct, unbroken contact with the sample, causing sample distortion and contamination during experimentation [44]. Optical tweezer uses optical

force to capture the target with a strongly focused laser beam, which can produce extraordinarily high forces for optically based systems (10~100 pN) [34, 45], however, control on a swarm of microrobots to perform bulk drug delivery together using optical actuation method is still in its infancy [46]. The other disadvantage of optical tweezers is that for *in vivo* applications, it will capture anything with a refractive index that differs from the background, resulting in that they will not only control the microrobots, but they will also affect the surrounding biological tissues and thus bring disturbances to further operation [34, 45, 47]. For example, when manipulating microrobots through a cell, if the difference between microrobot and cell composition diminishes, control commands will also have influence on the cell and bring potential harm to the integrity of the organisms.

3D Helmholtz coil systems generate a rotating uniform magnetic field, which induces a torque interaction between the system and the controlled magnetic object. Control of the microrobots, in this case, follows two basic mechanisms for motion in a Newtonian fluid [48-50]: chirality (helical structure swimmers, etc.) and flexibility (such as sperm-like swimmers) [51-62]. The coil system configuration is relatively simple, while the transformation of rotating magnetic field into actual swimming motion is more complex, as motion is highly impacted by the shape, rigidity, and magnetism of the microrobots.

Magnetic tweezer system, which manipulates microscale magnetic particles using magnetic force created by a magnetic gradient field, has three advantages among all those tools mentioned above according to [34, 39, 40, 63-69]. First, the force applied by the magnetic tweezer system does not contact with the target object and can be generated in different directions, thus the target object is not damaged by invasive behaviors, such as penetration by the cantilever in AFM. Second, compared to electromagnetic coil system, a magnetic tweezer system does not require the

chirality of the microrobot to have a nonreciprocal motion to swim in low Reynolds number environment and can apply a stronger force to achieve more operations like cell penetration [70]. Third, unlike the drawback of optical tweezers, magnetic forces can be applied specifically to the magnetic particles as most biological materials are free from magnetic influence [38, 41, 71].

During the past decades, similar systems have been developed by other research groups for different purposes of actuation and measurement [26-28, 33, 34, 38, 39, 64-69, 72-81]. The gradient of the magnetic field is necessary for a magnetic tweezer system to generate the magnetic force on the magnetic particles. Hence, the magnetic tweezer system usually employs magnetic coils to produce high magnetic flux near the sharp tips of magnetic poles, which could produce high magnetic gradient field near the poles, but also cause considerable heating under high current [71, 82] for *in vivo* applications. Here we manufactured the magnetic yoke by 3D printing using ferromagnetic material to elevate the performance while maintaining current input at low levels so that the heating issue within the working space can be significantly alleviated. To induce adequate force, sharp-tipped magnetic poles with high magnetic field saturation should be required so that the magnetic flux generated from the electromagnetic coil can be strongly released outward from the tip, then a high magnetic gradient field will be formed around the proximity of the pole tip and the magnetic force can be produced by dipole interaction with a magnetic microrobot [71]. As magnetic field strength decreases drastically away from the pole tip [71, 83, 84], high power output is necessary for generating sufficient magnetic gradient field within a large working space. Also, as one magnetic pole can only apply single direction force, one needs to have multiple magnetic poles oriented in different directions in order to generate forces in multiple directions. To make 2D control, 3 or 4 poles symmetrically placed in the same plane is necessary [79] while a six-pole structure with three poles on each of the top and bottom plane can lead to 3D control [85, 86]. So

far, most of the developed magnetic tweezer systems have a very small working space and a limited range of magnetic force due to low power output. However, the magnetic tweezer system we developed shows superior performance compared to the designs from other research groups. For power generation, each of the coils has 527 turns and can provide up to 630 Ampere-turn (with current input of 1.2 A) to generate the magnetic field. The effective working space from simulation results and experimental experience is about 1.5 mm × 1.5 mm on the *x*-*y* plane and 0.5 mm on *z*-direction, enabling experimentation with larger groups of microrobots. The six magnetic poles are aligned naturally on a tilted Cartesian coordinate system so that computation for rotation between actuation and measurement coordinates is simplified [76, 85, 87, 88]. 3D printing technology was utilized for this system design as it allowed fabrication of the hexagonal magnetic yokes with ferromagnetic material that makes the yokes lighter and easier to machine. The utilization of magnetic material for the yoke also introduces high magnetic permeability to further strengthen the generated magnetic gradient field, while other designs [76] only used non-magnetic material for the fabrication. For other parts, 3D printing also introduces more flexibility during design and construction stage, such as the design we achieved to make the placement and extraction of samples more convenient. The magnetic tweezer we implemented in this work was designed to have a stronger magnetic gradient field so that it is able to generate high magnetic force for controlling a swarm of microrobots to perform 3D swarm motion. This is a valuable capability not available in other systems. Swarm motion of microrobots could be important for applications like drug delivery and cell therapy, as the ability to carry drug or other payload of a single microrobot is usually limited, so bulky transportation is necessary.

Though some other groups have designed similar systems, their work usually concentrate on the simulation part and just did simple experimental demonstrations to show how the system

works. However, we deployed the system totally for complex experiments with microrobotics. Through the design, simulation, implementation, and experimentation of our 3D magnetic tweezer system, we demonstrate that the system can navigate microrobots on the desired trajectories with swarm motion in 2D and 3D. We proved that the suggested magnetic tweezer has enough power and the controllability to manipulate microrobots in both Newtonian and non-Newtonian fluid environments. The power source is integrated into the magnetic tweezer system through control algorithms based on MATLAB and LabVIEW; image processing was used for 2D and 3D real-time tracking as well as post-analysis of experiment data. The numerical magnetic field profile was simulated, and the results were compared with experimental measurement of the actual magnetic field in the designed system, which shows the relatively larger working space and force generation ability compared to other designs. Several tasks were accomplished, such as open loop trajectory control, obstacle avoidance, movement against micro-flow, 2D and 3D closed loop control, and swarm motion. The system was also optimized to be integrated with a haptics platform for long distance teleoperation and the final goal is to deploy it into *in vivo* based environments.

CHAPTER 2 DESIGN AND MODELLING

2.1 Magnetic Tweezer System Hardware Integration

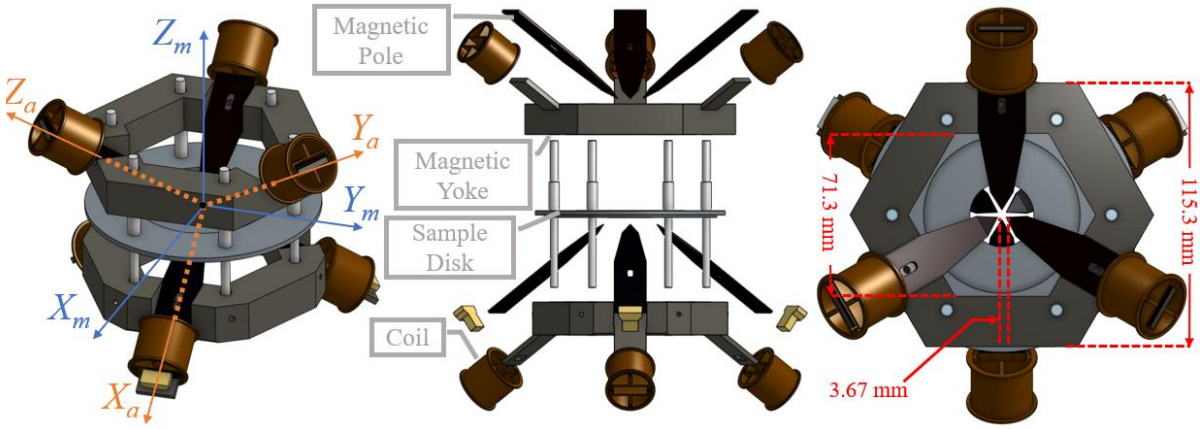

Fig. 2-1. Magnetic tweezer CAD model with illustration of measurement and actuation coordinate systems.

High magnetic permeability and magnetic saturation material are necessary for the poles to achieve the high-power output by the generated magnetic field from the pole tips. The poles were made of cobalt iron (VACOFLUX 50 from VACUUMSCHMELZE GmbH & Co.KG) that has a high saturation (2.35 T) feature and functional machinability for manufacturing of the sharp-tipped shape. The electromagnetic coils were made from AWG-25 heavy-built insulation coating copper wire with 527 turns for each coil. Six magnetic coils were positioned on the two yokes at the end of each pole, as shown in Fig. 2-1 [39, 41, 86]. Sharp pole tips were fabricated using laser cutting technology by Polaris Laser Laminations, LLC for the coarse shape. Further improvement of the tip shapes was individually optimized through machining. The tip shape uniformity is very

easy to be broken due to the extremely small dimension (average tip radius is about 40 μm as shown in Fig. 2-2 [40]) and machining resolution limitations. Six magnetic poles are fixed in pairs on top and bottom yokes to form an inclined Cartesian coordinate system, which is the actuation

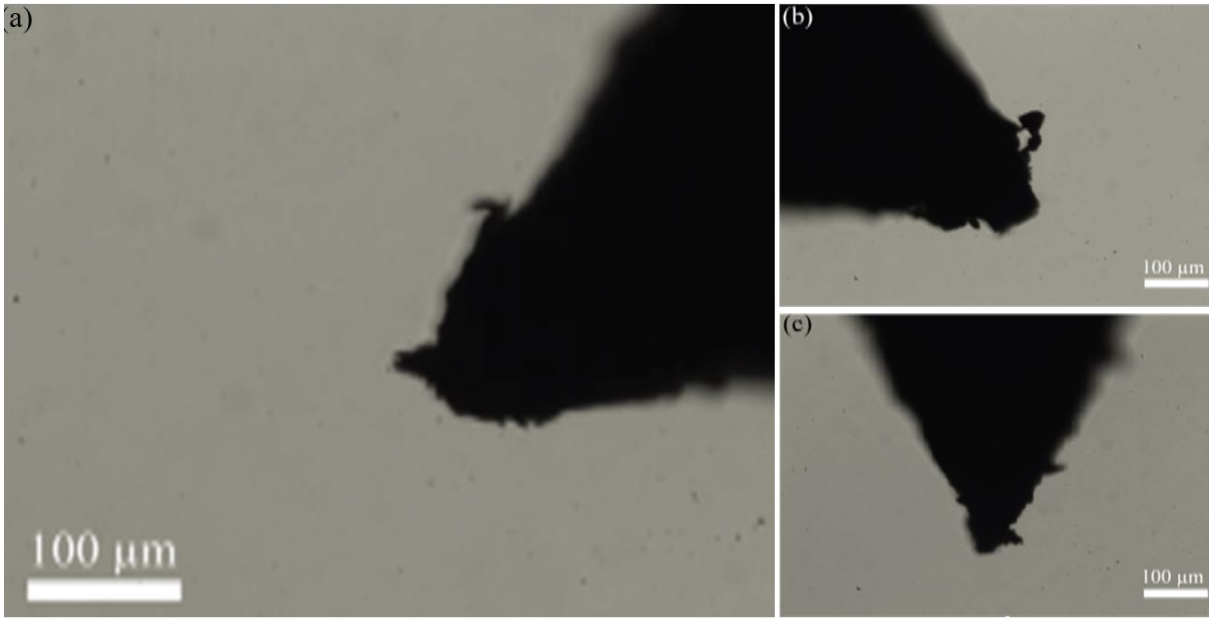

Fig. 2-2. Magnetic tweezer tips of the top assembly (a) Right tweezer tip, (b) Left tweezer tip, (c) Upward located tweezer tip. The scale bar is set to 100 μm.

coordinate system shown in Fig. 2-1. Through coordinate rotation, the measurement coordinate system is obtained. The angle between X_a and X_m is 35.26°, Y_a and Y_m is 45.00°, Z_a and Z_m is 54.74°.

The 3D printed hexagonal magnetic platform can form a closed magnetic circuit in the system to reduce the exciting current [40, 85] necessary for generating the magnetic field gradient and improve the efficiency of the magnetic field generation ability, which also helped reduce heating issues [40, 87]. The sample disk, which is also 3D printed, was installed on the microscope platform to connect upper and lower yokes as well as holding the whole system onto the microscope. Fig. 2-3 [41, 89] illustrates the system connections setup and data flow.

The integrated magnetic tweezer system was installed on an Olympus IX50 inverted system microscope. A color camera (Pixelink D734CU-T) and an Olympus 40× objective lens were installed on the microscope for image acquisition and visualization. Three power sources (GW Instek Programmable Digital AC/DC Power Supply) were connected with three relays (AXICOM D3023), respectively. Each relay controls the current output direction of one pair of coils that is co-axially aligned through the National Instruments SCB-68A Connector Block, which accepts and sends control signals from the customized control algorithm to generate a magnetic field in arbitrary directions [39-41, 86, 89]. Through simulation results and experimental

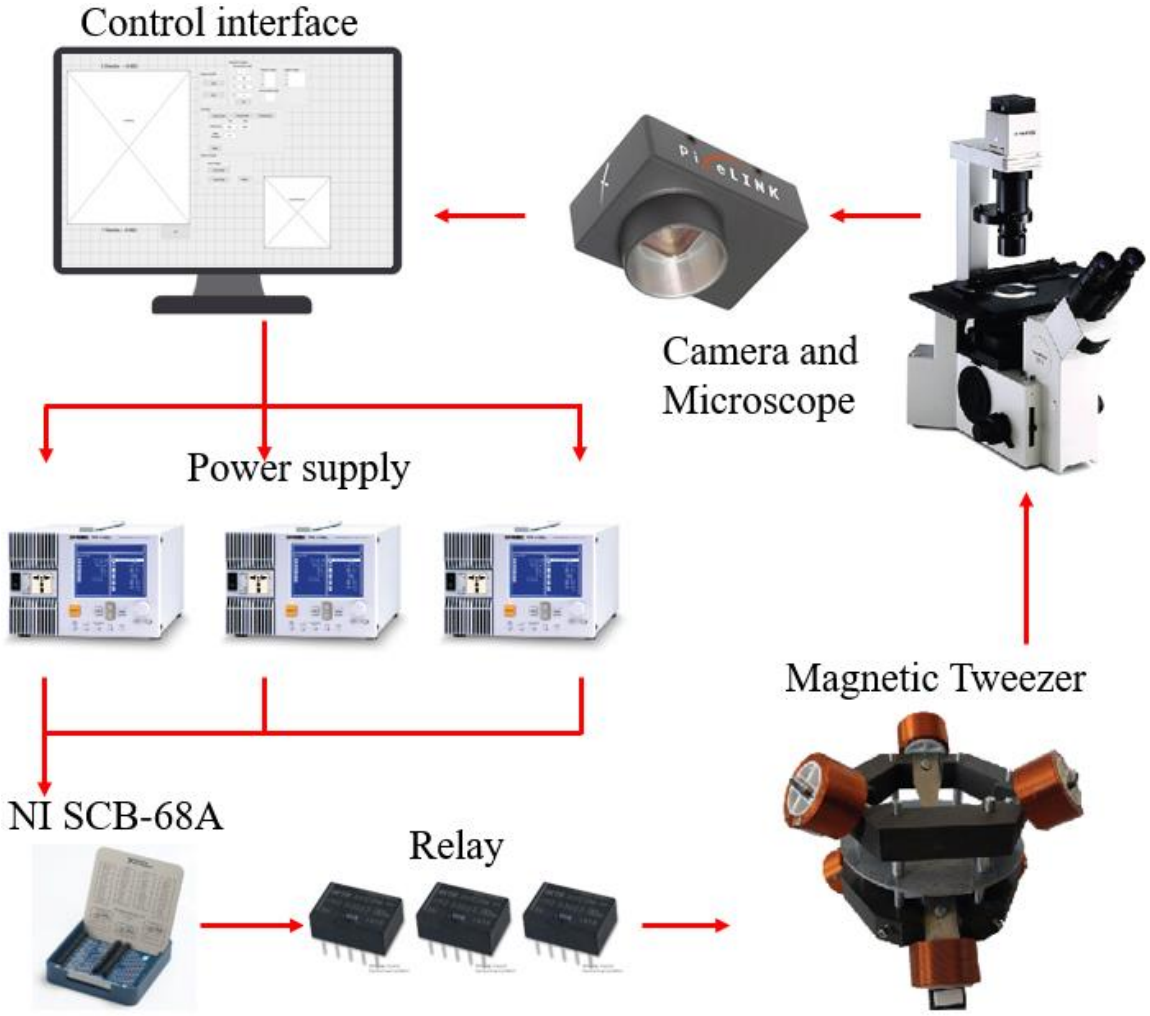

Fig. 2-3. Magnetic tweezer system setup, blue line represents power output, black line represents control signals and orange line represents final control output.

experience, the effective working space is about 1.5 mm × 1.5 mm × 0.5 mm. A polydimethylsiloxane (PDMS) chamber with dimension of 1.5 mm × 1.5 mm is used in the working space on the sample disk for the solution samples for experiments.

As this system utilizes a magnetic field gradient mechanism directly to generate magnetic force, it will not require a high current frequency to produce a rotating magnetic field like electromagnetic coil system [36, 51, 55]. Even though the hysteresis effect is presented in this material, which will cause considerable heat during high-frequency operation, it still fulfills our demand as the system is designed to be operated within 15 Hz and the heating issue caused by the poles is negligible [87]. As such, natural convection is more than satisfactory for the regular experiment, which can be seen from the temperature measurement data in Fig. 2-4 [86]. We used a Fluke 51 ii digital thermometer with probe dimeter of 0.9 mm to attach to different components for measurement. For the measurement on magnetic poles, we placed the probe near the sharp tip to get measurement as close as possible while avoiding damage to the tip. The results are recorded with a time scale of 10 minutes with different current inputs, which are the regular time length for our experiment. Coil temperature increases quickly under high current while the temperatures in magnetic poles and the sample chamber are negligible. Under this situation, the system does not need an extra cooling method as natural heat dissipation is sufficient for the experiment purpose.

After eliminating the production and position error during the installation process, each pole on the same plane has a gap of 3.67 mm, the distance between the top and bottom planes are 2.04 mm. The magnetic tweezer system we built surpasses the other research groups' configurations in terms of working space, power generation ability and 3D printing using magnetized material. A comparison is also shown in Table 1 [39, 71, 76, 82, 85]. While our new magnetic tweezer system has higher or equivalent magnetic field strength, it is achieved through a

much longer distance from the pole to the center, which means the effective working space is larger. Moreover, the working space and number of coil turns are considerably larger than the others, which will bring more potential in the further exploration of research tasks such as cell penetration, and object transportation.

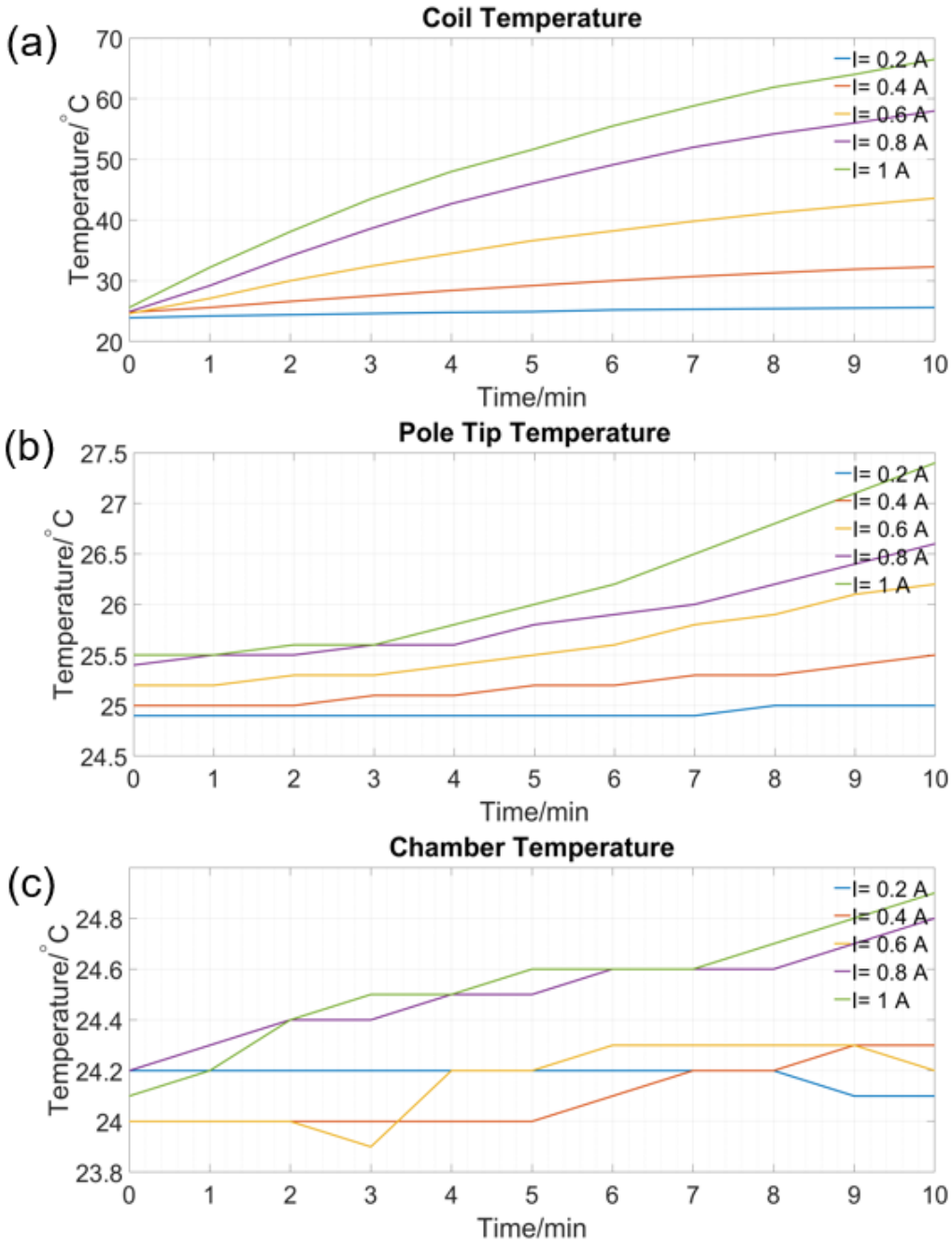

Fig. 2-4. Temperature increases under different currents on each part of magnetic tweezer system.

Table 1. Comparison of Different Groups Work

Property	Our group	Menq's group [71, 85, 87]	Krause's group [76]
Coil Turns	527	50	240
Magnetic field strength	6 mT in the center	3 mT in the center	8 mT in the center
Working Space (X×Y×Z)	1.5×1.5×0.5 mm^3	Less than 0.9×0.9×0.5 mm^3	60×60 μm^2

2.2 Fabrication of Microrobot

Microrobots were fabricated by mixing the Streptavidin Coated Ferromagnetic Particles (commercially available from SpheroTech with diameters of 4.21 μm or 10.6 μm) with 20% w/v NaCl or 0.5% w/v synthetic mucus to get a 1% v/v concentration sample solution for different experiments. Mucus is primarily composed of mucin glycoproteins, DNA, lipids, salts, cells, and cellular debris. It exists throughout a living animal's body, with very distinct viscoelastic properties. Mucin is the primary component of mucus responsible for non-Newtonian effects with shear thinning property [48, 55, 56, 61]. The viscosity in the synthetic mucus was not homogenous and there were a lot of bulky particles existing in the flow, which provide excellent conditions for simulating *in vivo* environments [48, 90]. Thus, we used a solution of 0.5% synthetic mucus (Sigma-Aldrich M2378-100G mucin extracted from a porcine stomach and mixed with deionized water at concentrations of 3-5%) for demonstrating the motion in a non-Newtonian fluid environment as well as obstacle avoidance. The solution is vortexed with a VWR Vortex mixer for ~30 seconds and then magnetized by approaching a permanent magnet for ~15 seconds before injecting into the experiment chamber [39-41, 86, 89]. Microbeads in the solution may randomly

combine with each other in the solution to from multi-bead microrobots through magnetic dipole interaction. The chamber was then covered by a thin glass slide to protect the solution from disturbances caused by air flow and vaporization, and to prevent it from contaminating the poles.

For microrobots composed of multiple beads, chain structures are formed due to the magnetic dipole interaction of the beads, which provides a sufficiently strong connection for the motion under magnetic field gradient, but it can be easily broken under sudden external control signal change, such as fast spinning and fluid dynamic resistance caused by a high viscosity fluid. Randomly mixing the microbeads leads to microrobots with different lengths. For our experiment

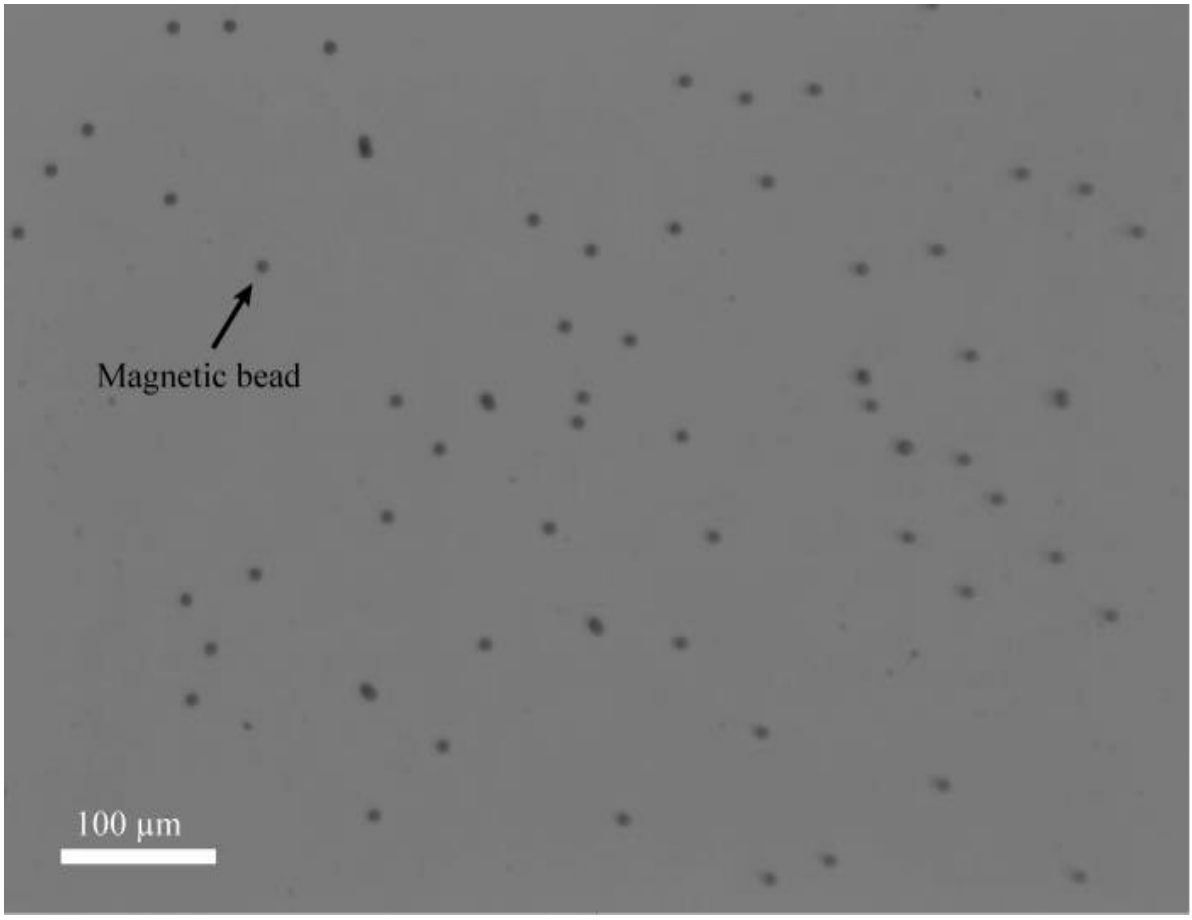

Fig. 2-5. Spheric magnetic beads in fluidic environment. The beads have diameter of ~10.6 μm.

demonstration, we mainly focus on microrobots composed of equal to or less than 3 beads [37]. Fig. 2-5 shows the distribution after mixing.

2.3 Modeling for Force Generation

The force modeling contains three parts: direction vector normalization, coordinate transformation, and voltage input amplification for power output. A minimal number of three different direction orthogonal forces are necessary for 3D control [39-41, 71, 86, 89]. The localization of magnetic poles in the actuation coordinate system can be simply understood by imagining a face-centered cubic structure [40, 88] where the face centers are the accurate positions for all the poles. The measurement coordinate system is arbitrarily defined as indicated in Fig. 2-1 that also shows the magnetic tweezer system CAD model. The transformation matrix from the measurement coordinate system to the actuation coordinate system is computed as in Eq. (2-1)

$$
\begin{aligned}
{}^{a}_{m}\boldsymbol{R} &= [\boldsymbol{R_x}(45°)]\left[\boldsymbol{R_y}(35.26°)\right] \\
&= \begin{bmatrix} 0.8165 & 0 & -0.5774 \\ 0.4082 & 0.7071 & 0.5774 \\ 0.4082 & -0.7071 & 0.5774 \end{bmatrix}
\end{aligned}
\tag{2-1}
$$

where $\boldsymbol{R_x}$ and $\boldsymbol{R_y}$ are the rotation matrices for space-fixed coordinate transformation around *x*-axis and *y*-axis, respectively. When the direction vector, $\boldsymbol{X_m}$, in the measurement coordinate system is given from the user or the closed loop control algorithm, ${}^{a}_{m}\boldsymbol{R}$ will transform it into vector $\boldsymbol{X_a}$ in the actuation coordinate system as in Eq. (2-2):

$$
\boldsymbol{X_a} = \begin{bmatrix} x_a \\ y_a \\ z_a \end{bmatrix} = {}^{a}_{m}\boldsymbol{R} \cdot \begin{bmatrix} x_m \\ y_m \\ z_m \end{bmatrix} = {}^{a}_{m}\boldsymbol{R} \cdot \boldsymbol{X_m} \tag{2-2}
$$

$$\widehat{\boldsymbol{X}}_{\boldsymbol{a}} = \frac{\boldsymbol{X}_{\boldsymbol{a}}}{|\boldsymbol{X}_{\boldsymbol{a}}|} \tag{2-3}$$

Once $\boldsymbol{X}_{\boldsymbol{a}}$ is obtained, the control algorithm will normalize it into $\hat{\boldsymbol{X}}_{\boldsymbol{a}}$ to get the unit output ratio, it then is combined with gain parameter given by user to generate the power supply output. Depending on the magnitude of the gain parameter set by user, an amplifying factor K_g is applied to $\hat{\boldsymbol{X}}_{\boldsymbol{a}}$. A compensation vector $\boldsymbol{K}_{\boldsymbol{c}}$ for current input which was determined through experimental calibration with value of $[0.04\ 0.01\ 0.01]^{\mathrm{T}}$ (Ampere), is also taken into consideration to compensate the power output error caused by the deviation of pole shapes, resistances on different coils and the corresponding circuits. The final current output $\boldsymbol{I}_{\boldsymbol{f}}$ in each direction is shown in Eq. (2-4).

$$\boldsymbol{K}_{\boldsymbol{c}} = \begin{bmatrix} K_{cx} \\ K_{cy} \\ k_{cz} \end{bmatrix}, \boldsymbol{I}_{\boldsymbol{f}} = \begin{bmatrix} I_x \\ I_y \\ I_y \end{bmatrix} = K_g \cdot \widehat{\boldsymbol{X}}_{\boldsymbol{a}} + \boldsymbol{K}_{\boldsymbol{c}} \tag{2-4}$$

Currents from the power supplies will flow through the relays instantly and be directed to appropriate coils for charging depending on the signs of each component in $\hat{\boldsymbol{X}}_{\boldsymbol{a}}$, which causes in the microrobot to move along desired direction in the measurement coordinate system. According to [71], the magnetic field generated from three poles can be expressed as

$$\boldsymbol{B} = \sum_{i=1}^{3} \frac{4\pi}{\mu_0} \frac{q_i}{r_i^2} \boldsymbol{u_i}, \tag{2-5}$$

$$\begin{aligned} \boldsymbol{Q} &= [q^1\ q^2\ q^3]^{\boldsymbol{T}}, \\ \boldsymbol{Q} &= \frac{N_c}{\mu_0 \Re_a} \boldsymbol{I}_{\boldsymbol{f}} \end{aligned} \tag{2-6}$$

$\boldsymbol{B}$ is the magnetic flux density, r_i is the distance from the magnetic pole tip to the magnetic microrobot, μ_0 is the permeability of free space (vacuum), q_i is the magnetic charge defined by q

=Φ/μ_0, Φ is the magnetic flux, and $\boldsymbol{u_i}$ is the unit vector pointing from the magnetic charge to the magnetic microrobot. $\Re_a$ is the reluctance between the pole tip and the working space center, and N_c is the number of turns of the coil. As the six poles in our system are not connected to the same yoke as in [71] , the $\boldsymbol{K_I}$ matrix in the vector of magnetic charges $\boldsymbol{Q}$ can be neglected. At the same time, there will only be 3 magnetic poles at most that are activated, which leads to $\boldsymbol{Q} = [q_1\, q_2\, q_3]^T$. From Eq. (2-5) and Eq.

(2-6), the force generated from a single pole on a single bead can be expressed as [40, 91]

$$\boldsymbol{F} = (\boldsymbol{m} \cdot \boldsymbol{\nabla})\boldsymbol{B} \tag{2-7}$$

$$\text{with} \quad \boldsymbol{m} = \frac{\pi d^3}{2\mu_0}\left(\frac{\mu - \mu_0}{\mu + 2\mu_0}\right)\boldsymbol{B} \tag{2-8}$$

where $\boldsymbol{m}$ is the magnetic moment of the microrobot, μ is the permeability of microrobot, and d is the effective diameter of microrobot. A stronger magnetic moment can be obtained if a microrobot is composed of more microbeads as the effective diameter will be larger. For locations far from the pole tips, the resultant force can be expressed as the superposition of force vectors in three directions. To get a stronger force generation, it is essential to increase the power input or manipulate microrobots composed of more particles as the generated magnetic force is related to both magnetic gradient field and magnetic moment of the microrobot.

When the system is activated, microrobot will reach steady state rapidly, thus we can also calculate the magnetic force by computing the viscous drag force. By using modified Stoke's law [81], we can get the viscous drag force as

$$\boldsymbol{F}_{\boldsymbol{viscous}} = \boldsymbol{F}_{\boldsymbol{magnetic}} = 6\pi\eta r\boldsymbol{v}(1 + \frac{9r}{16h}) \quad (2\text{-}9)$$

where η is the viscosity of the solution, r and $\boldsymbol{v}$ are the radius and speed of the microrobot, respectively, and h is the distance between the centroid of microrobot and the chamber wall Since h is much larger than r, the last term in Eq. (2-9) can be neglected. Also, the magnitues of the gravitational and the buoyancy forces are similar for the type of particle we used in 20% w/v NaCl solution and are much lower compared with the magnetic force, so both can be considered negligible. Therefore, viscous drag will directly equal the magnetic force produced by the magnetic tweezer system and we can utilize this relationship for force analysis in post-experiment data analysis.

The force generation model shown above is embedded in the LabVIEW-based system for open loop control and the MATLAB-based system for closed loop control. By receiving the direction and magnitude input from the user or feedback control algorithm and observing the motion by the camera, the computed control input will manipulate power supplies and relays to generate the corresponding current output. Then, the arbitrary magnetic gradient field will be generated and direct microrobots for different tasks.

2.4 Magnetic Tweezer System Control Software Illustration

There are two different control software configurations developed specifically for our magnetic tweezer system, one for manual control, developed in LabVIEW, and the other one for feedback control, programmed with MATLAB, both of which require integration with 3rd party drivers provided by the camera and power supply manufacturers.

2.4.1 Open Loop Control

The manually controlled algorithm consists of three major parts shown in Fig. 2-6(a) [39]. The controller itself utilizes a proportional control mechanism to give control output from power

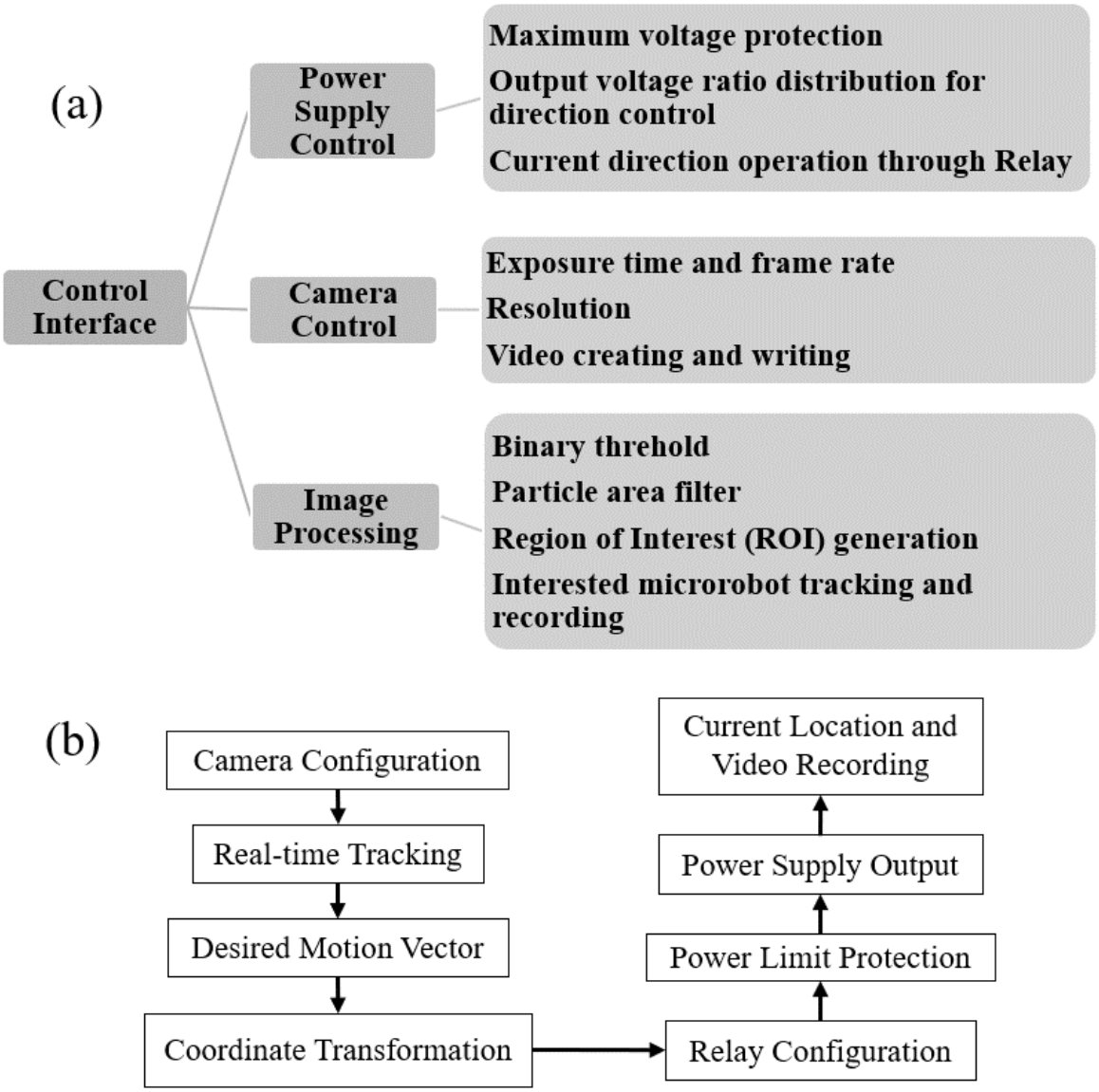

Fig. 2-6. (a) Functions of open loop control interface. (b) Open loop control diagram.

supplies based on the gain magnitude given by user. As shown in Fig. 2-6(b), the desired motion vector is given by user through the interface as user observes microrobot motion in real-time. The motion vector is then amplified by the gain parameter set by user and sent to power output control

part. The power supply control operates the three power supplies based on the output vector obtained from motion vector and the relays redirect current to the different coils for each pair based on the negative or positive sign of the power output vector. Camera control functionality configures image capture specifications, such as image type, exposure time, frame rate and resolution. Normally high resolution and exposure time will set limitations on the frame rate. The experimental video is recorded during every experiment and saved afterward. Real-time image processing presets tracking parameters such as the threshold for the binary image, targeted microrobot area size, and a region of interest of the recorded area. It then automatically records necessary information during the experiment, including object trajectory, time, corresponding power output and so on for post-experiment data analysis.

2.4.2 Closed Loop Control

The closed-loop control interface was created using a MATLAB graphical user interface. Fig. 2-7 [41, 89] illustrates the flow of the control algorithm. We deployed a proportional controller with the gain parameter adjustable by the user during the experiment. The equation of motion is expressed as

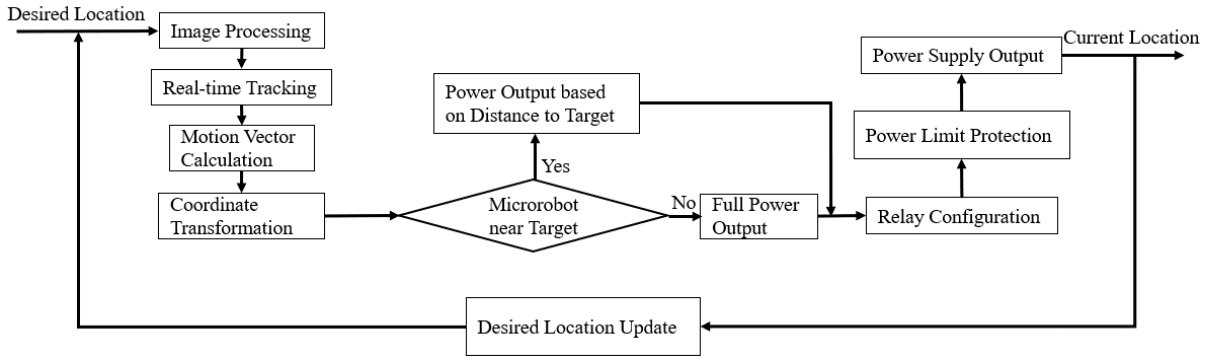

Fig. 2-7. Magnetic tweezers system closed-loop control diagram.

$$m\ddot{\boldsymbol{x}} = \boldsymbol{f}_m - \boldsymbol{f}_d \tag{2-10}$$

with $\boldsymbol{f}_d$ as drag force in the fluid and $\boldsymbol{f}_m$ as magnetic force from Eq. (2-4) to Eq. (2-8) given by controller. Drag force will be balanced by magnetic force at steady state and thus the microrobot can move steadily in the chamber. After the desired location is given by the user, the algorithm will process the images captured from the camera to get the direction vector and area information of the target microrobot using real-time tracking. The algorithm then calculates the motion vector based on the direction vector as shown in Eq. (2-11), where P_t and P_c are target point and current

$$\boldsymbol{X_m} = \boldsymbol{P_t} - \boldsymbol{P_c} \tag{2-11}$$

point, respectively. The motion vector in measurement coordinate system is converted to coordinates in the actuation coordinate system and is normalized as shown in Eq. (2-2) and Eq. (2-3). Then the algorithm will check if the microrobot is within 50 pixels from the target. If yes, the power output magnitude will be decreased proportionally based on the distance to the target and this magnitude is applied based on the normalized motion vector for actuation to avoid overshooting. If microrobot is still far from the target, the power output gain parameter will be fully applied to the normalized motion vector. Once the final power output is confirmed, the relays will activate one of the coils in each pair by comparing the negative or positive sign of the force vector and direct the current to the appropriate magnetic poles on the magnetic tweezer system. The power supplies have a preset output limit to protect the coils and circuit from overheating.

2.5 Conclusion

In conclusion, this chapter illustrated the hardware design, fabrication of microrobots, system force modelling, control software development and implementation of the hexagonal 3D magnetic tweezer system. Hardware components and their integration to the system were described. The material and methods for fabricating microrobots were explained in detail.

Temperature performance of the system was investigated. Mechanisms of open loop and closed loop control algorithms were illustrated in the software development part to clearly define the workflow of how the system operates in real-time. The fundamental principles of force modelling for 3D magnetic force generation with coordinate transformation between the actuation coordinate system and the measurement coordinate system were presented. All parts mentioned above constitute the magnetic tweezer system we built for the investigation of wireless manipulation of microrobots.

CHAPTER 3 SIMULATION AND MEASUREMENT COMPARISON

To validate the magnetic field profile of magnetic tweezer system, we compared the simulation and experimental results. The force generation model derived in the previous chapter was utilized for simulation analysis. The CAD model shown in Fig. 2-1 was imported into COMSOL Multiphysics to perform a magnetostatic linear simulation. In the simulation, only one pole was activated with an input current of 1 A. Also, to assure correspondence between simulation and experiment, the magnetic pole tip shape in the CAD model was adjusted by measuring the tip radius in the actual system before we proceeded with the simulation. All the other specifications, such as air permeability and density, conductance of coils and poles, were chosen under room temperature and standard pressure. For measuring the magnitude of the magnetic field in the experimental setup, a Metrolab THM1176-HFC magnetometer probe was used, the probe has measuring range of μT to 14 T, DC to 1 kHz with ±1% accuracy. The position of the measuring point was located by a Deltron 2202 XY Linear Translation Stage with a resolution of 0.01 mm for *x*-*y* plane measurement, and an Edmund Coarse/Fine Movement, ¼-20 w/ Rotation, Rack & Pinion with resolutions of 0.25 mm (coarse) and 0.03 mm (fine) for vertical motion to measure different *z*-direction layers. The power input was set to be the same current value with the one in simulation applied to the pole for the positive direction of X_a.

3.1 Experimental Measurement

The measured magnetic fields on three *x*-*y* planes of z = 0.5 mm, 1.6 mm and 2.5 mm are shown in Fig. 3-1(a). A total of 21 points were chosen on each plane following the measuring

trajectory in Fig. 3-1(b). Each point was measured for 15 seconds with sampling rate of 100 Hz and then the average value was computed. The hexagon shape represents the top view of the magnetic tweezer system and the six corners are the poles on top and bottom planes. The overall measured area was selected to be larger than the effective working space in order to acquire the global magnetic field distribution, which enables us to have enough data for further comparison with simulation results. The longest measuring distance was 5 mm, which is between point 9 and 13.

In Fig. 3-1(a), we can see that as the activated pole was located on the bottom plane, so the magnetic field strength on those planes decreases as the distance increases. In addition, on symmetric points such as points 1 and 3, points 4 and 8, points 9 and 13, the absolute values of magnetic field are almost the same, and this indicates that the generated magnetic field is symmetric about the axis of the activated pole, which follows the physics in general. The magnetic

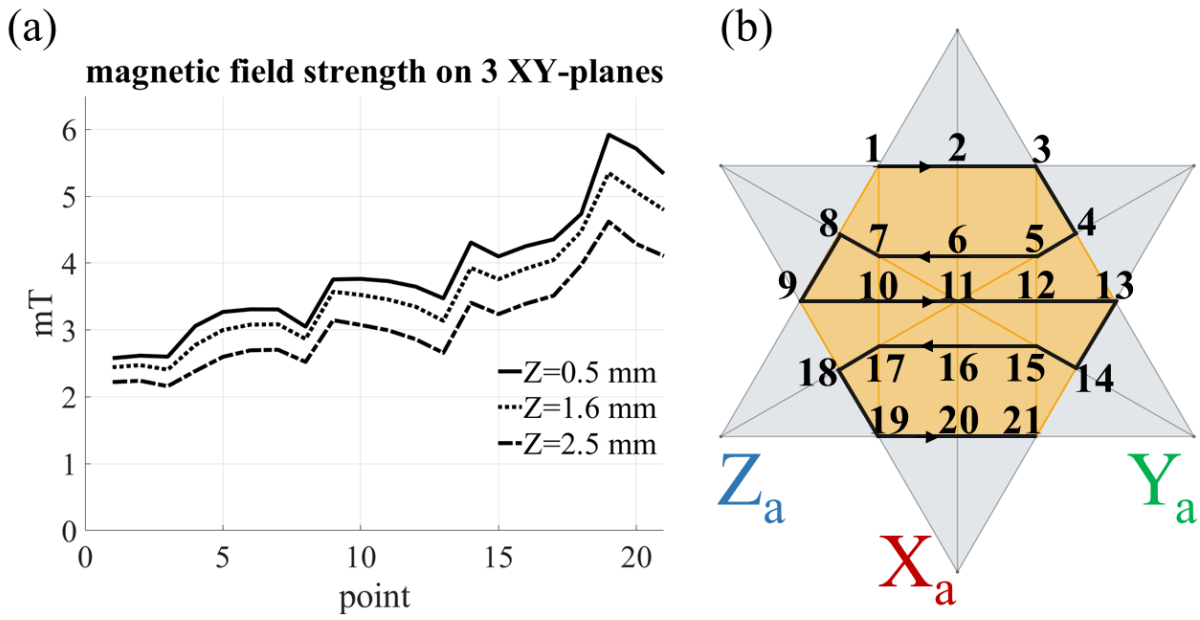

Fig. 3-1. Magnetic field measured under a 1 A current. (a) magnetic field strength in X_a positive direction. (b) measuring trajectory for data collection.

field in the center achieved by single magnetic pole can reach up to 6 mT under this current input When the input current is increased or decreased, the magnetic field strength and gradient will simultaneously be higher or lower.

3.2 Magnetic Field on *x-y* Planes

In Fig. 3-2, a color map of the three-dimensional magnetic field distribution in the working space is constructed for both the experiment and the simulation to give a clear comparison and understanding. The obtained experimental data were numerically interpolated to get the full profile of the magnetic field over the working space, which is shown in Fig. 3-2(c) and (d). Fig. 3-2(a)

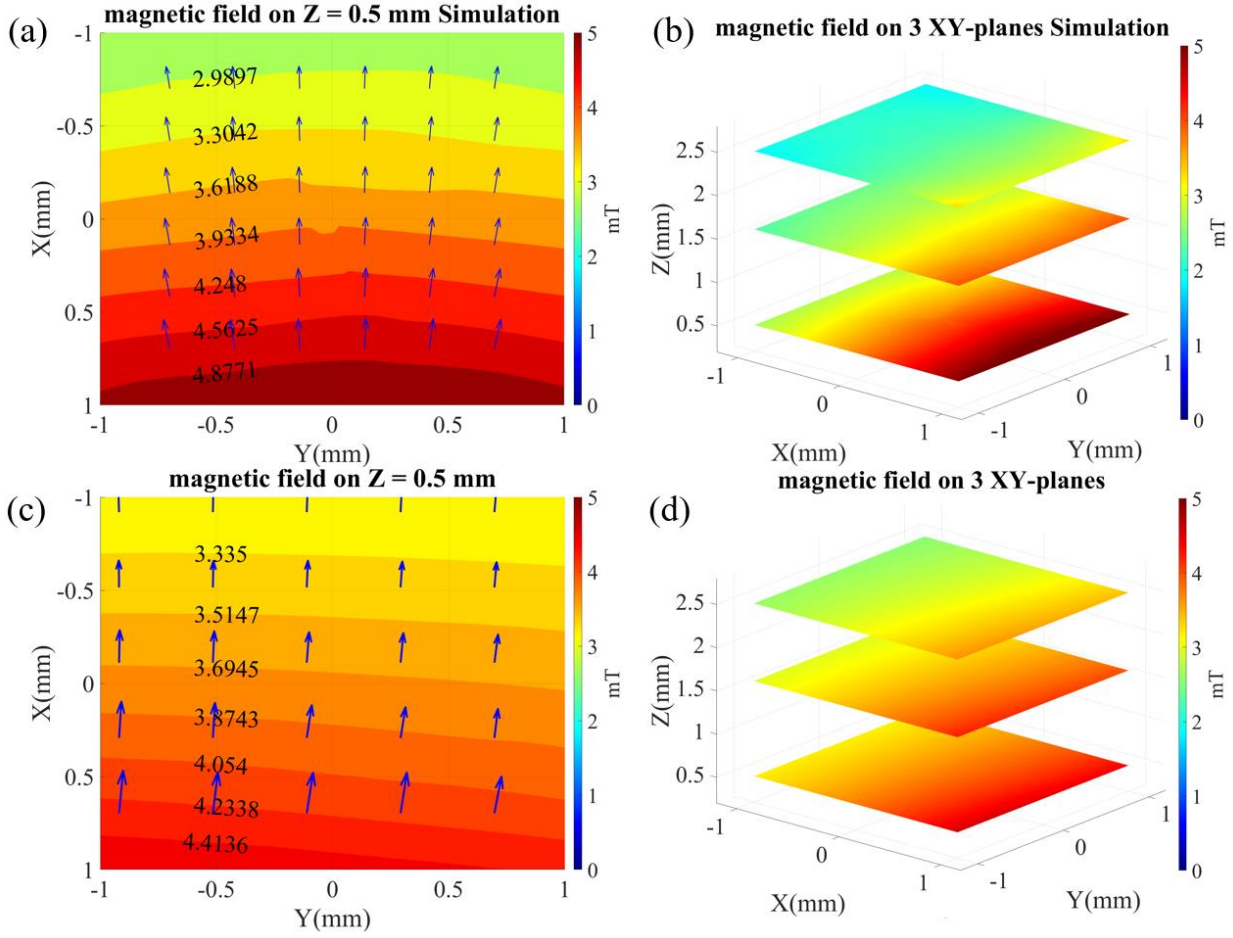

Fig. 3-2. Magnetic field comparison between simulation and experiment on *x-y* plane. Blue arrows in contours indicate the magnetic flux direction. (a) simulation result on z = 0.5 mm, (b) simulation 3D view result. (c) experiment result on z = 0.5 mm, (d) experiment 3D view result.

and (b) shows the corresponding simulation results. When the distance in the *z*-direction is too far from the pole, the generated magnetic field will be relatively unchanged in the working space, which results in the magnetic field gradient being diminished as shown in the top plane in Fig. 3-2(b) and (d). Therefore, the effective working space along the *z*-direction is set to be 0.5 mm for evaluating the data. In the central area of the working space, the magnetic gradient field is smoothly and uniformly distributed, which indicates that the magnetic field gradient will also have the same property and produce uniform magnetic force. The simulation result shows a few tooth-shape changes in the center, which is caused by the meshing limitation of the pole tip in the simulation model. Because the dimension of the tip is extremely small compared to the overall system shape, and the configuration of meshing size across the whole object cannot have a tremendous deviation, it is necessary to find the balance between suitable meshing size of the CAD model and acceptable simulation time. As a result of data analysis, the magnetic field gradient between -0.75 mm and 0.75 mm along the *x*-axis is uniformly distributed with a strength of 0.8 T/m in the direction of the released magnetic flux from the activated pole.

The uniform magnetic field gradient in the working space provides consistent magnetic force and makes it adaptable to deploy the force model into our control algorithm for microrobot manipulation. To study the important relationship between the experiment and the simulation for validating the feasibility of implementing a theoretical control model into a practical system setup, a detailed comparison of the experiment and simulation results is shown in Fig. 3-3. Three lines at $z = 0.5$ mm parallel with the activated pole were chosen to find the magnetic field values on them. Left ($y = –0.75$ mm) and right ($y = 0.75$ mm) lines in Fig. 3-3 represent the effective working space boundaries on both sides. The magnetic field strengths show strong matches with an error variance of less than 8% within effective working space between simulation and experiment results. The

decreasing trend of the magnetic field is linear with the distance from the pole, illustrating the

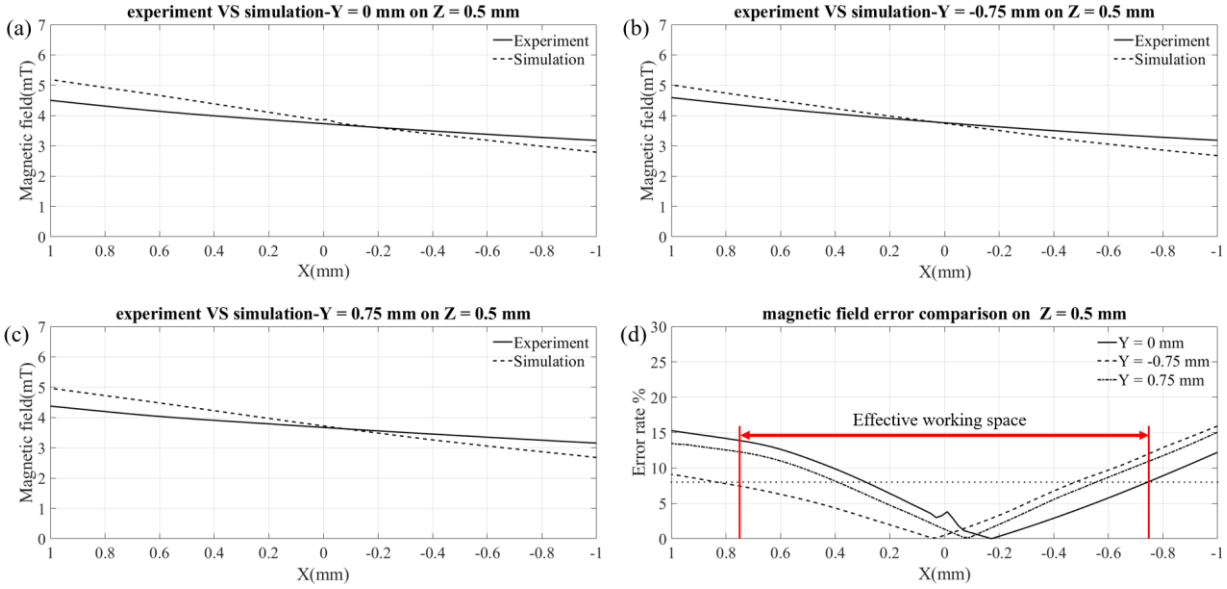

Fig. 3-3. Magnetic field quantitative analysis on center, left and right lines on z = 0.5 mm in the effective working space. Magnetic field strength on (a) center line (y = 0 mm). (b) left line (y = -0.75 mm). (c) right line (y = -0.75 mm). (d) error rate between experiment and simulation, flat dotted line is the 8% error rate, effective working space range is in red.

uniform magnetic field gradient distribution seen in the contours in Fig. 3-2. For the comparison between theoretical and experimental results, the slope of the relationship between the magnetic field and the distance from the pole in the simulation is slightly steeper on all three lines. The variance might be caused by the difference of air properties between actual experiment and simulation, as well as the magnetic pole manufacturing limitation, which shows acceptable deviations for implementing the design into the actual system as the error rate shown in Fig. 3-3(d) is low in our desired working space range. The left and right lines have a relatively smaller magnetic field magnitude as the locations in those two areas are always further than that on the center line from the pole.

3.3 Magnetic Field on *x*-*z* Plane

The magnetic field along vertical direction was also analyzed to investigate the effective working space range. Three planes with y= –1, 0, 1 mm were selected for extracting data from the simulation result. In the case of experimental measurements, there was a limitation to measure with respect to *z*-direction because of the difficulty to access the specific position using the probe. However, according to the analysis in section 3.1 on *x*-*y* planes, it is acceptable to assume similar matching result between the measurement and simulation result for *z* plane. The 3D magnetic field shown in Fig. 3-4(a) implies that magnetic fields on all the planes have a uniform distribution, even in a longer distance between the measuring *x*-*z* planes comparing to our effective working space. Thus, the distribution within this area must be similar in the *z*-direction. The contours in Fig. 3-4(b) show that the magnetic field gradient distribution on all *x*-*z* planes are uniform, the force model we introduced in the system can also follow the same trend as what we learned from Fig. 3-2. By superposing the force generated from several activated poles through the direction vector we arbitrarily set as the input in the force generation model, precise and versatile resultant force can be generated in the effective working space.

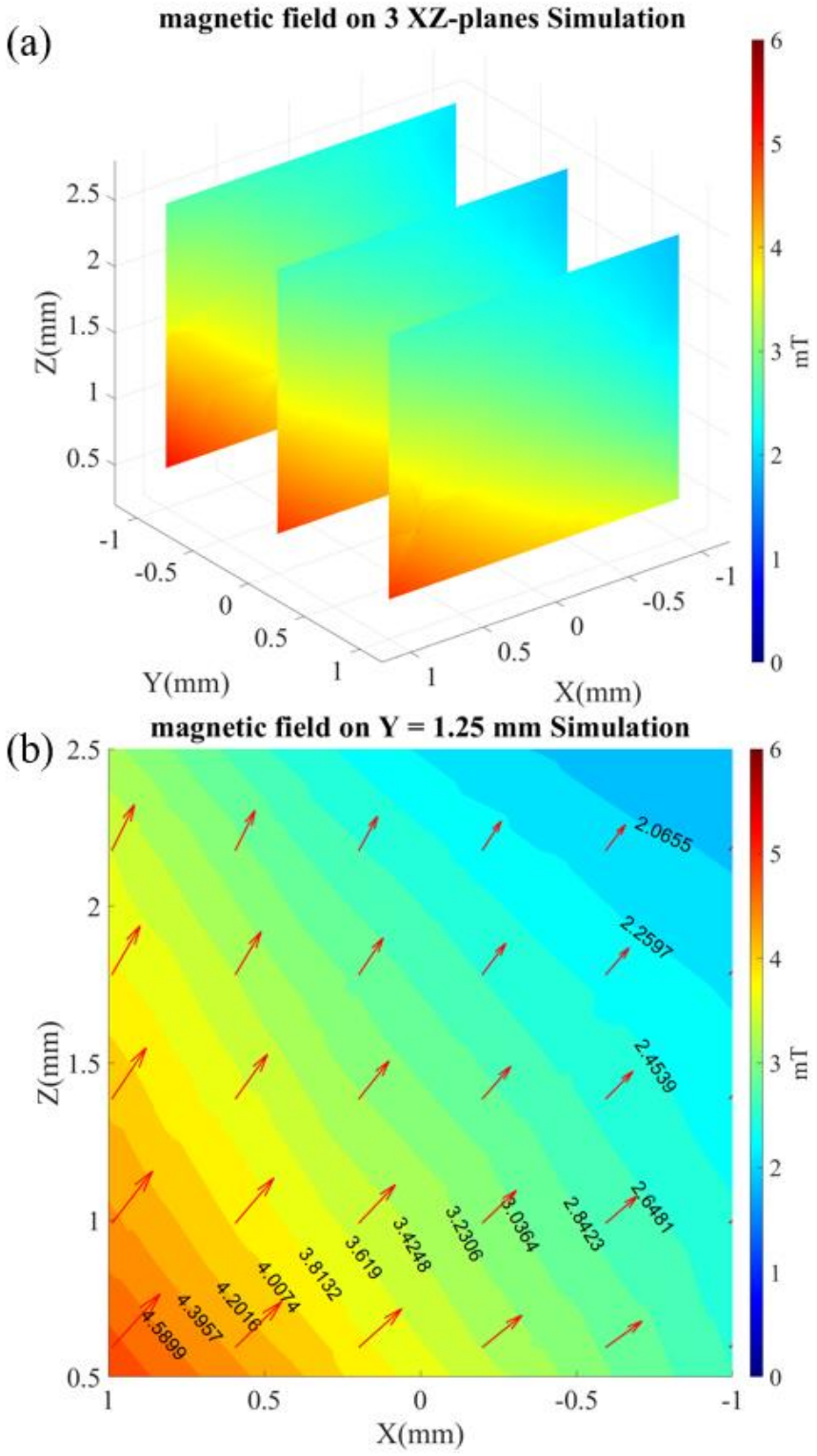

Fig. 3-4. Magnetic field of simulation on *x*-*z* planes with $y = -1$, 0, and1 mm. (a) Magnetic field on three *x*-*z* planes. (b) Magnetic field on y = 1.25 mm simulation. Red arrows in (b) indicate the magnetic flux direction.

3.4 Conclusion

In this chapter, magnetic tweezer system performance is validated through comparison between simulation and experimental data. Actual magnetic field strength was measured and interpolated to build up the magnetic field map within working space, which was then compared to the simulation results conducted under same working parameters, such as magnetic pole location and current input magnitude. The error rate between simulation and experiment was calculated and considered under acceptable range. The main purpose for the comparison between simulation and experiment is for validating the system performance. After validating the simulation results for an ideal system, we can then forecast the magnetic distribution in the actual results systems based on simulation for magnetic field estimation for locations that cannot be easily measured physically, such as locations along *x*-*z* planes. The simulation results match with our measurement results closely, which indicates the designed system is well developed with proper magnetic gradient field generation ability.

CHAPTER 4 EXPERIMENT RESULTS AND DISCUSSION

4.1 Relationship between Speed and Current

By adjusting the focal plane and examining the 20% NaCl sample solution in the central area, a 10.6 μm single bead microrobot was chosen to collect the velocity data under the actuation of a single pole. The experiments were proceeded by varying the voltage from 1 V to 10 V with a linearly increasing current trend from 0.11 A ~ 1.33 A. Then the velocity was measured from recording the swimming motion for more than 35 s under the same current. Using image processing

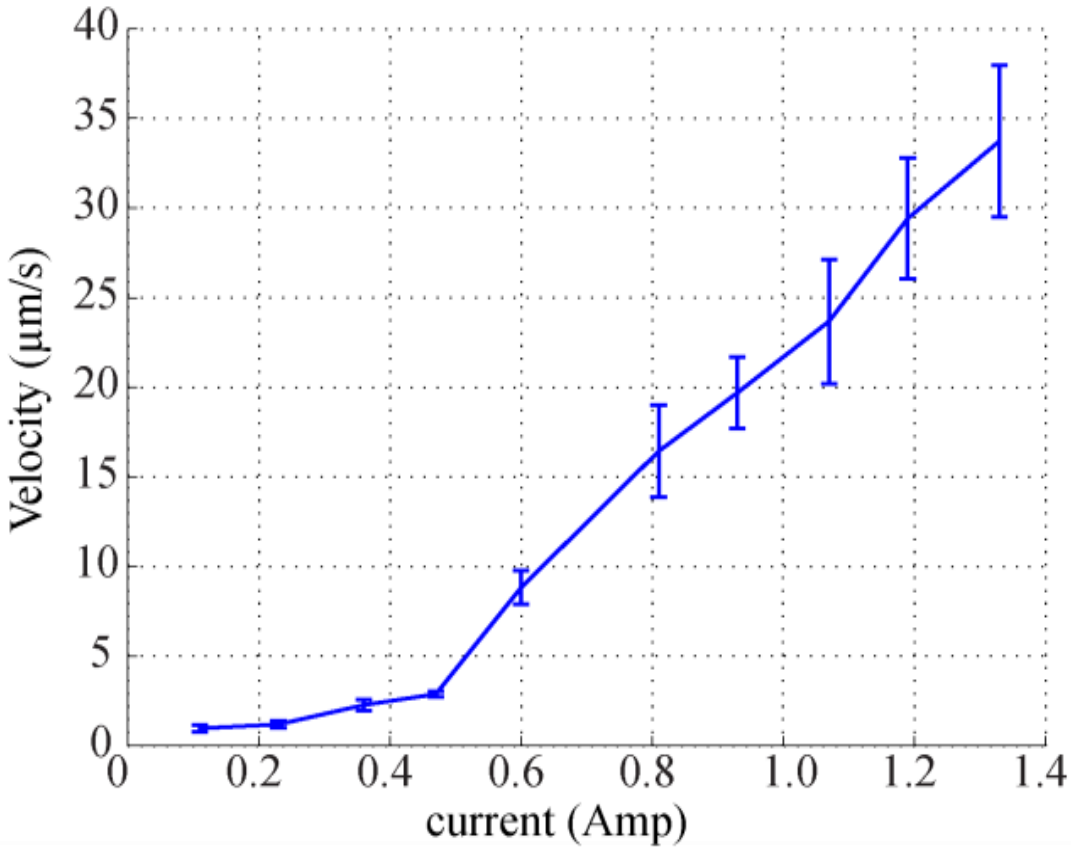

Fig. 4-1. The relationship between velocity of a single magnetic microbead and applied current. The error bars indicate the standard deviation of velocity data in each test.

and object tracking, the trajectory of the motion was obtained to get the mean and error along with the current relationship. After every experiment was performed, the microrobot was navigated back to the original location to ensure the same condition of surroundings except the control input current. According to Fig. 4-1, velocities of the microrobots stay almost to zero when current is under 0.38 A, which is the exciting current needed to overcome the resistance of surface friction when particles settle to the bottom of substrate. After the system passes the exciting current, the relationship between velocity and current is nearly linear, which is consistent with the relationship between current input and magnetic force if all other parameters in Eq. (2-7) are constant. With current input known, we will be able to estimate the magnitude of the magnetic field, while the relationship mentioned here can serve as an intuitive reference between current input and expected velocity for 2D motion for future development of this work.

4.2 Motion Control Validation

In order to measure the control flexibility, such as microrobot force output and 3D motion, we introduced single bead and multi-bead microrobots into the NaCl solution and synthetic mucus samples. Both samples act as a mechanism to check the control algorithm capability and microrobot performance when placed in a different medium. Through 2D motion experiments, the directional control matches accurately with the microrobot heading direction with rapid response. In 3D motion preliminary testing, SU-8 structures (epoxy-based negative photoresist, non-magnetic) from microfabrication were deployed on the bottom of the sample acting as reference objects to indicate the focal plane change. When the magnetic gradient field is activated in the working space, the SU-8 structure will remain still on the bottom while microrobots moved upward against the gravity force and finally be out of the focal plane. The relationship between the area

size of a microrobot in binary image processing and *z* axis displacement from the focal plane is then collected and utilized for real-time 3D tracking and closed loop control.

4.2.1 Control Flexibility and Obstacle Avoidance - Open loop

Complex trajectories could be achieved by operating the open loop control interface to manipulate a single bead microrobot. In this case, we used it to spell out the initials of our Biological Actuation, Sensing & Transport Laboratory in 20% w/v NaCl solution. Once completed, the results were stitched together via object tracking and image processing. The 'SMU BAST' lab trajectories are shown in Fig. 4-2. The currents vary in range on the three power

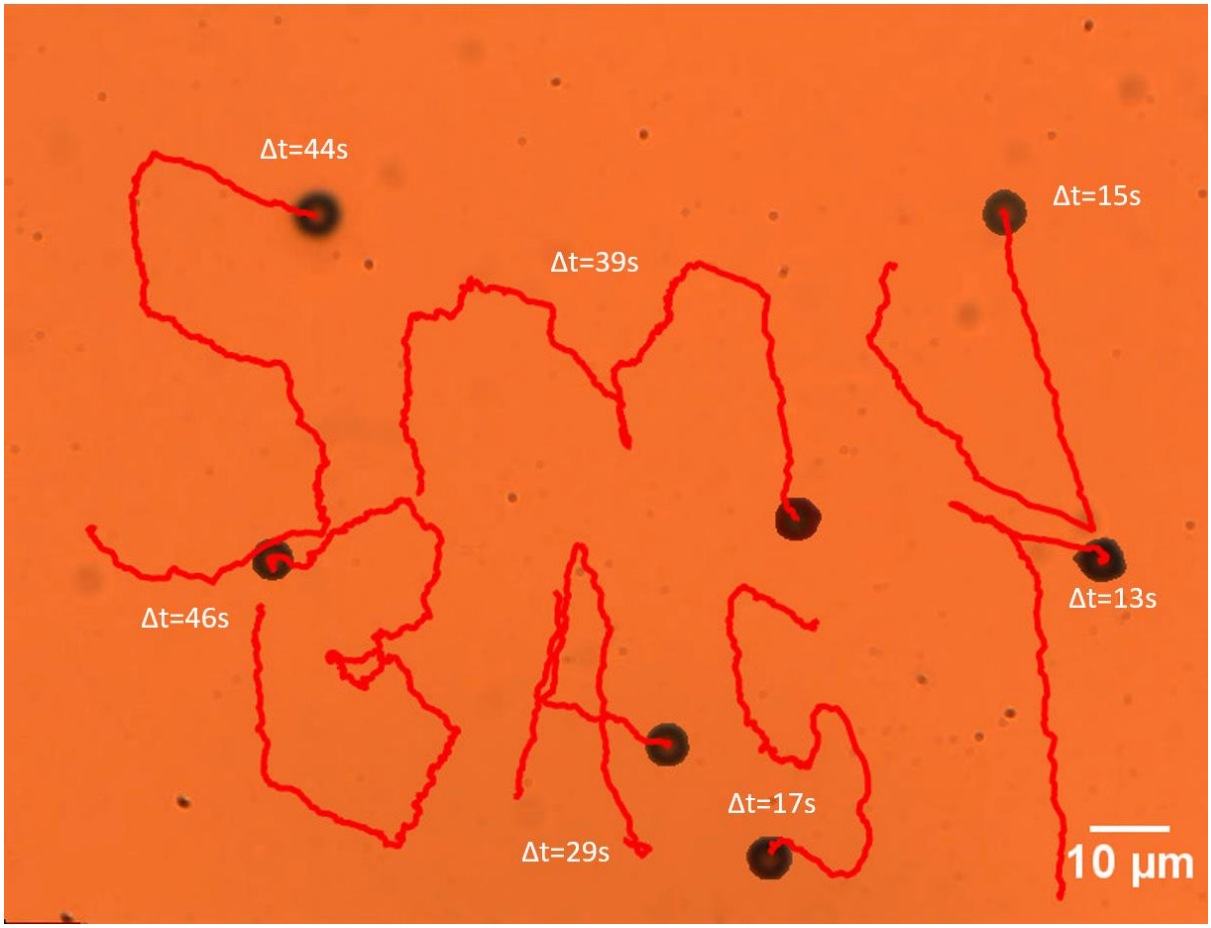

Fig. 4-2. SMU BAST lab trajectory. This is the same bead completing multiple trajectories which were then superimposed into a single image. Δt represents total time used for each trajectory.

supplies between 0 A- 1.2 A, limited by the voltage protection preset in the control algorithm to protect the system. During experimentation, user was able to visually recognize the microrobot through the camera. Microrobots were then controlled by the desired way points given by the user to move in the presence of external disturbances like Brownian motion and foreign substances. Each trajectory was finished within 50 s with closely matched direction between the desired motion vector and the output motion direction. This fundamental experiment proves the potential of advanced control in the magnetic tweezer system to perform more complex operations such as closed loop control and obstacle avoidance [88].

In Fig. 4-3(a), we used a solution of 0.5% synthetic mucus for the obstacle avoidance demonstration. The viscosity of the solution was measured as between 0.1-0.02 Pa/S with shear rate ranging between 1-100 (1/s) through preliminary work in [92]. We manipulated a two-bead microrobot for the experiment, which produced a larger magnetic moment to generate stronger magnetic force when compared to single bead microrobots. In comparison to the 20% NaCl solution from Fig. 4-2, it is obvious that the traveling time for the relative path length in synthetic mucus was higher. This is mainly caused by high and randomly varying viscosities and bulky substances. When the microrobot became immobile due to the high viscosity or microstructures inside the flow, we rotated the controllable magnetic gradient field direction while increasing the power input to make the microrobot suddenly ‘jump’ or crawl (Left side of Fig. 4-3(a) and Fig. 4-3(b): the microrobot performed crawling several times, which are shown as the trajectory direction changes drastically with corresponding high velocity and distinctive deviations). The microrobot then successfully escaped from that area and continued the task with more stable velocity profile. The two-bead microrobot traveled freely within the working area with a relatively

slow average speed about 4 μm/s. Still, it is likely that with a higher power input and more optimal control strategy, the speed performance can be substantially improved.

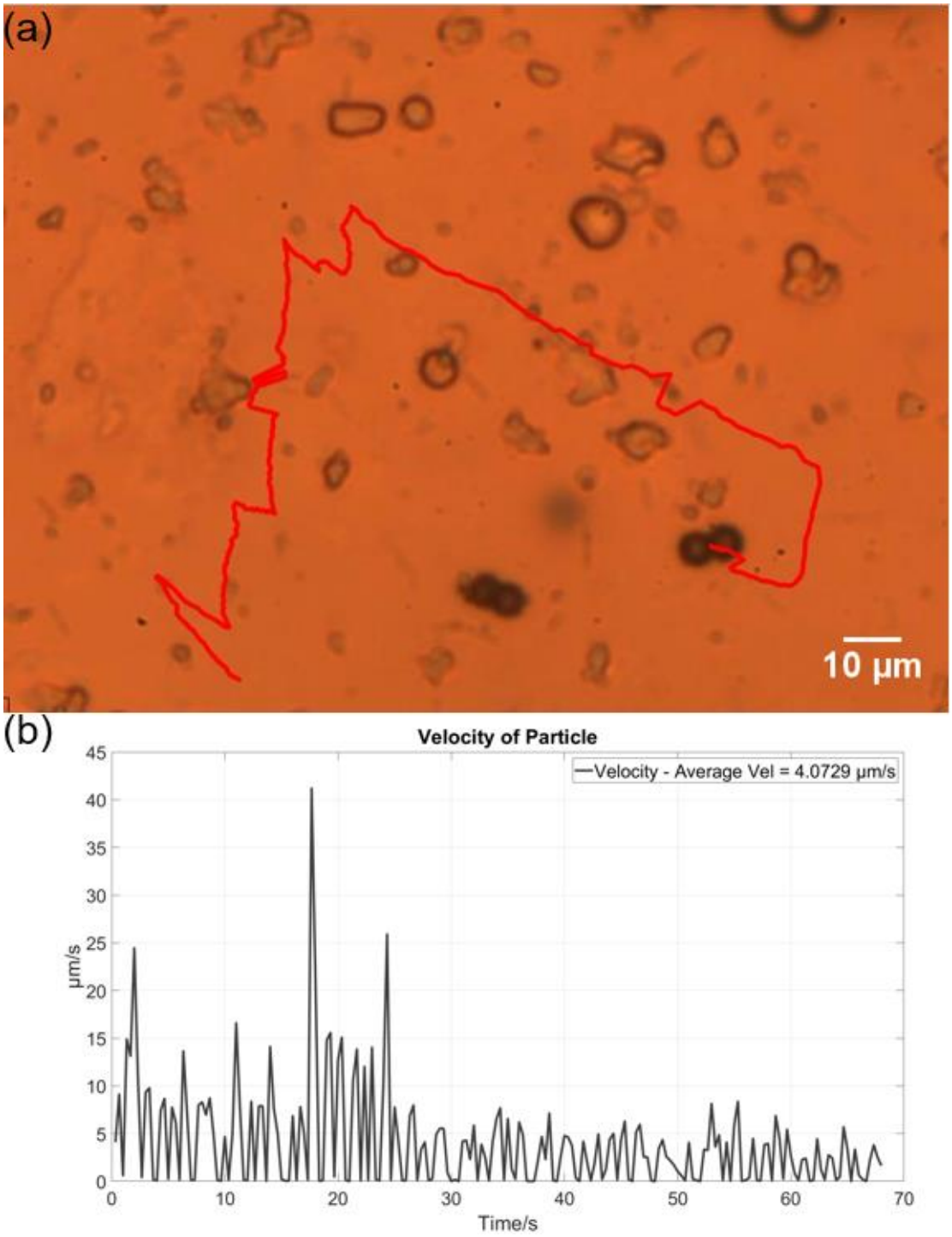

Fig. 4-3. (a) Controlled microrobot moving from bottom left to top first and then moving toward the bottom right to avoid bulk particles in synthetic mucus. (b) velocity analysis in for motion in (a).

4.2.2 Magnetic Force against Microflow - Open loop

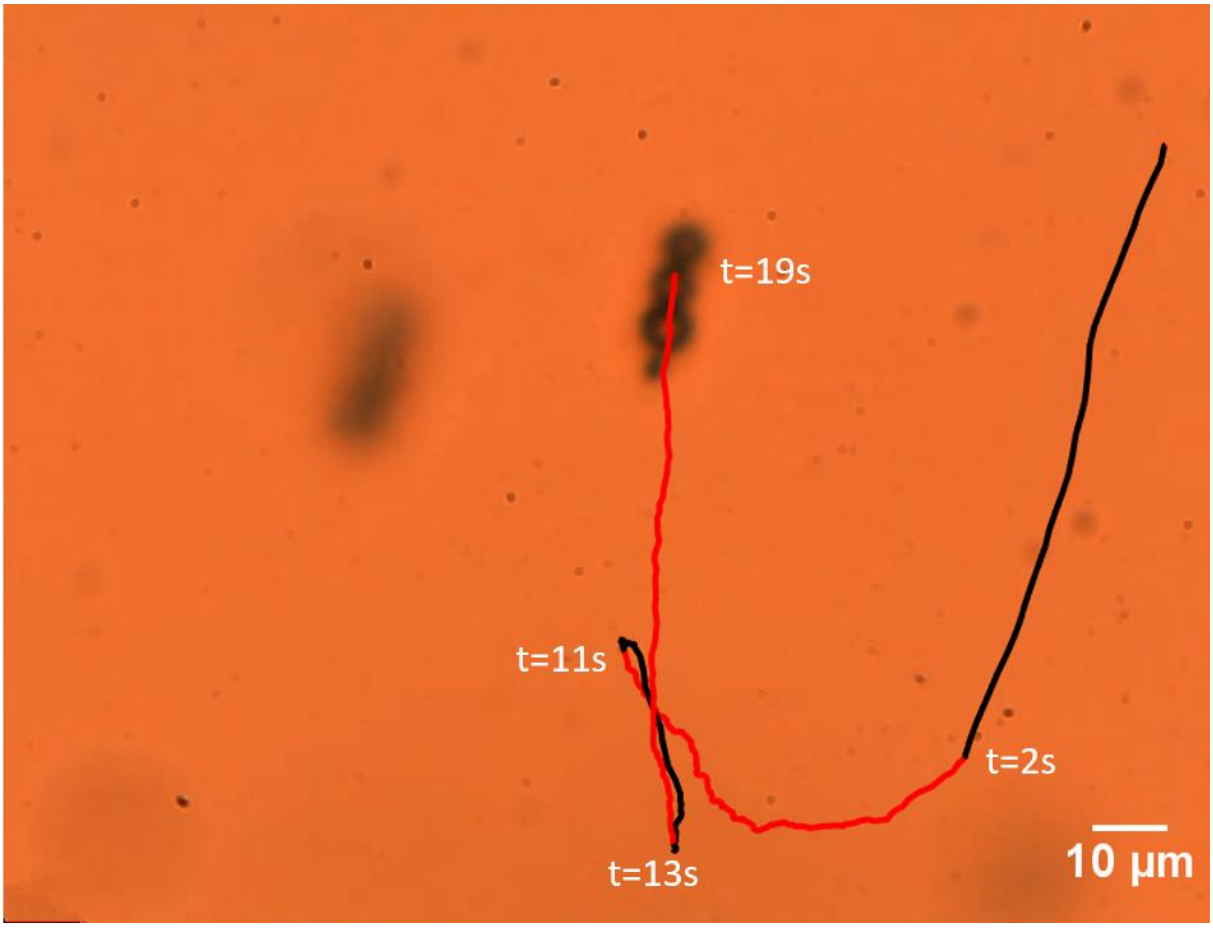

Fig. 4-4. microrobot trajectory with background microflow. Black trajectories are swimming with microflow, red trajectories are swimming against microflow under control input.

Presence of microflows is a very critical issue in microrobot applications due to its power in disrupting microrobot motion, and microflows exist everywhere in *in vivo* environments. It is noteworthy that swimming within microflows under controllable maneuverability is a challenge that researchers need to overcome for further *in vivo* applications. To prove the performance of our magnetic tweezer system, a three-bead microrobot shown in Fig. 4-4 was first freely drifting downward without any control input, following the microflow in the chamber, which is indicted as the vertical black trajectory on the right. After 2 s, the control started to engage, giving a

direction control to the upper left corner with an increasing power input, which is shown as the curved red trajectory on the bottom. The microrobot first maintained its motion downward while also moving to the left. As power increases, direction of motion changed gradually and then finally reversed. At 11 s, the control input was turned off and the microrobot drifted again for 2 s before the control input was turned back on at 13 s. This is shown as the vertical short black and red trajectories on the bottom. The microrobot then continued to move upward against the microflow for another 6 s. By comparing the microrobot performance with/without control input, it can be seen that the force generation provides enough power to actuate the microrobot in complicated fluid environment.

4.2.3 2D Control for Specific Trajectory - Closed loop

Closed-loop 2D control using the magnetic tweezers system was achieved by controlling a single particle microrobot to navigate to several way points on the *x*-*y* plane. The microrobot was first navigated to a specific location before each experiment. Then it followed the arbitrary user defined way points in sequence.

Fig. 4-5 shows the trajectories 'SMU' conducted from three experiments. The regular power output was set to 1.5 A, allowing the microrobots to translate quickly while keeping the temperature of the system low. In all cases, the microrobots could reach their intended destination in a reasonable amount of time. The average speed for 2D motion was around 2.6 μm/s for single bead microrobots. One thing worth mentioning is that at the beginning and end of the magenta trajectory in '**S**', the microrobot struggled to move under the applied control signal. This may have been caused by the excessive surface friction and the presence of microflows. However, the microrobot did eventually overcome these obstacles, guided by the control algorithm, and proceeded to the target position. When the microrobot almost arrived at the junction between the

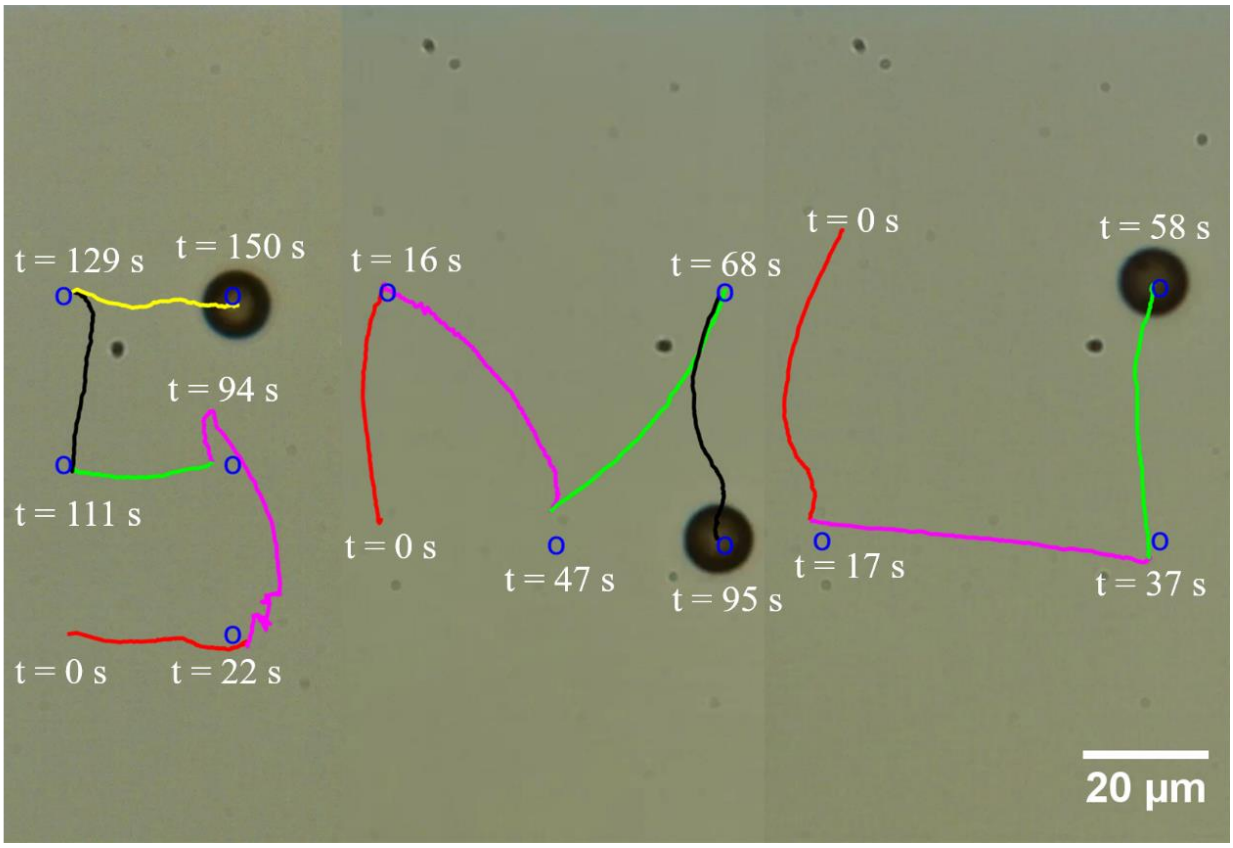

Fig. 4-5. 2D trajectory of 'SMU'. Blue circles represent the desired locations for each trajectory. Different colors represent each trajectory between every two desired way points.

magenta and green trajectories, it went beyond the target position, but then was controlled back automatically. This may be due to the limitation of the controller for not being able to adjust the gain parameter adaptively when the user applies excessive power for control. Even with the mechanism to decrease the power proportionally with decreased distance to target, overshooting may still happen near the target as the approaching velocity is too high. However, this can be addressed in the future with adaptive control or PID control to achieve more stable and precise motion. A similar situation also occurred in trajectory '**M**' at the junction of the magenta and green trajectories This was corrected by retroactively changing the target destination. Aside from these two deviant situations, the system could accurately guide the particles to their intended positions. Trajectory '**U**' shows a very stable motion in its trajectory since the fluid environment within this

experiment sample was not influenced by microflows and the microrobot was not exposed to excessive surface friction. The resulting trajectory was smooth and the microrobot maintained a stable velocity.

In 2D motion, the error between microrobot location and the desired location was maintained at less than 1.6 μm on all the target points, which is almost seven times smaller than the size of the microrobot. To achieve a closer and more precise route to the target, we can set a sequence of way points with short gap or use other control strategies with state control of both location and velocity. This experiment demonstrates that the performance of the closed-loop controller that minimizes the distance between microrobot and target location was very precise.

4.2.4 3D Motion Analysis

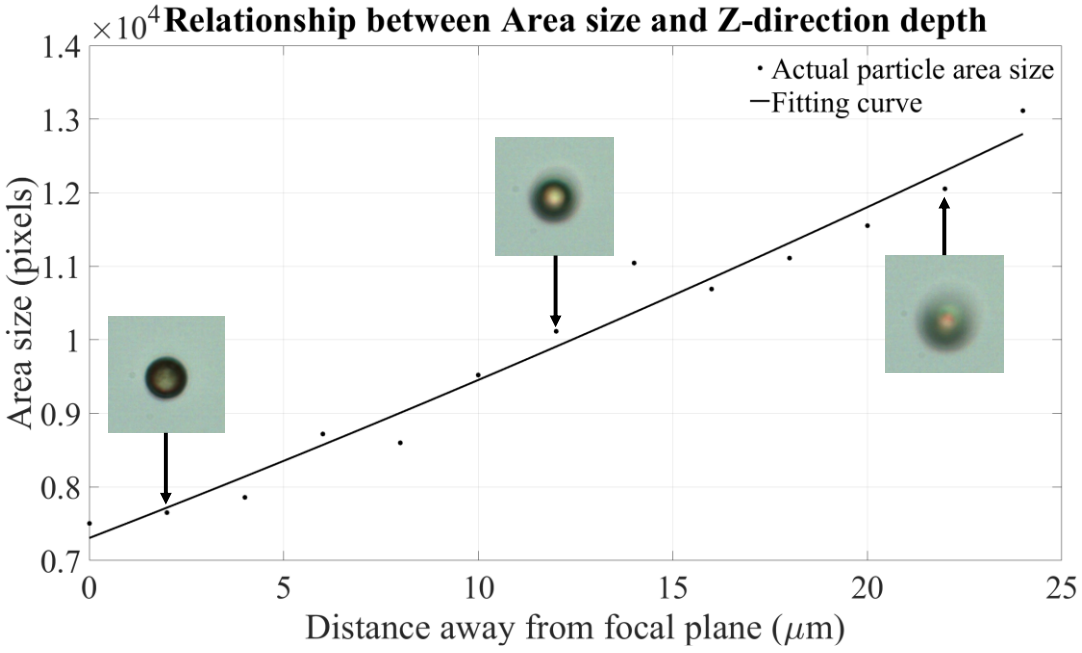

Fig. 4-6. Relationship between *z*-axis location and area size of a microrobot.

The 3D motion evaluation will provide evidence of additional capabilities of the microrobots to complete versatile tasks in practical applications within both *in vitro* and *in vivo*

environments. The current 3D motion phenomena achieved by the magnetic tweezer system can be distinguished indirectly as there is only one camera mounted on the microscope. Location information on the *x*-*y* plane can be obtained, so another method is required to get the *z*-location of the microrobot [90, 93]. As the microscope has the feature to move the stage in a 2 μm resolution, we collected the area size difference data of the microrobot under different focal planes, then a quadratic relationship between area size *S* and *z* direction displacement is found and shown in Fig. 4-6, in which the collected data points closely match to the fitted curve relationship. When the camera starts capturing images from the bottom (z = 0 μm) focal plane, the area size is at the minimum, as microrobot is moving upward away from the focal plane, the area size $S(\mu m^2)$ will increase, and the displacement Δz can be calculated as

$$S = \mathrm{a}z^2 + \mathrm{b}z + \mathrm{c} \tag{4-1}$$

$$S_{up} - S_{bottom} \tag{4-2}$$

$$= \mathrm{a}\left(\mathrm{z_{up}} - z_{bottom}\right)\left(z_{up} + z_{bottom}\right) + \mathrm{b}(z_{up} - z_{bottom})$$

where constants a (dimensionless) and b (μm) are obtained from the relationship in Fig. 4-6 with values of 0.2684 and 9.3746, respectively, and c is neglected as it will be canceled out as shown in Eq. (4-2) when the bottom and top areas are compared. For all 3D motion experiments, the bottom focal plane is arbitrarily set as $z_{bottom} = 0$, thus

$$S_{up} - S_{bottom} = \mathrm{a}z_{up}^2 + \mathrm{b}z_{up} \tag{4-3}$$

$$\text{with} \quad z_{up} = \frac{-\mathrm{b} + \sqrt{\mathrm{b}^2 + 4\mathrm{a}(S_{up} - S_{bottom})}}{2\mathrm{a}} \tag{4-4}$$

The area sizes *S* are known from real-time tracking and image processing.

We first applied this algorithm to pre-collected data to extract the 3D motion information. In the video frames in Fig. 4-7, SU-8 microstructures of the average diameter of 10 μm were imported into the sample and sank onto the bottom as reference for *z*-axis direction recognition. When adjusting the microscope focal plane away from the SU-8 objects, their patterns became blurry and their imaged area increased [90]. Several directional vector inputs that included positive *z*-direction control were then configured one by one to control the microrobot motion on *x*-*y* plane while performing vertical motion, the *x*-*y* plane motion in this task is just for easier observation for the microrobot at different time points. As we kept adjusting the microscope to focus on the microrobot, the blurred background and increased SU-8 substance area size indicate that microrobot has 3D motion and was able to overcome its own gravitational force to move upward.

At the beginning of the experiment, the microrobot (4.21 μm microbead) was placed on the bottom surface of the experimental substrate with SU-8 obstacles, the microscope's focal plane was adjusted to the surface manually. Control inputs were then configured to navigate the microrobot so that it moved upward in *z*-direction while also moving left and right on an *x*-*y* plane to stay in the field of view. The 3D tracking method utilized in the post-image processing is based on the relationship between *z*-direction distance and particle area size when defocused [90, 93]. The extracted 3D motion information is shown in Fig. 4-7(a), in which the green, black, and blue dash lines represent the projections of the 3D trajectory (red solid line) on *x*-*y*, *x*-*z*, and *y*-*z* planes, respectively. As the experiment continued, it was clear that the microrobot moved vertically from the original focal plane in Fig. 4-7(b). The blurred background and obstacles with their increased size indicate that microrobot was moving up, and the obtained 3D trajectory shows that the movement in *z*-direction is comparable with the motion on a horizontal plane. The analysis from

this testing result concludes that the generated magnetic force was strong enough to overcome the friction on the substrate surface and microrobot's own gravity force to move it upward.

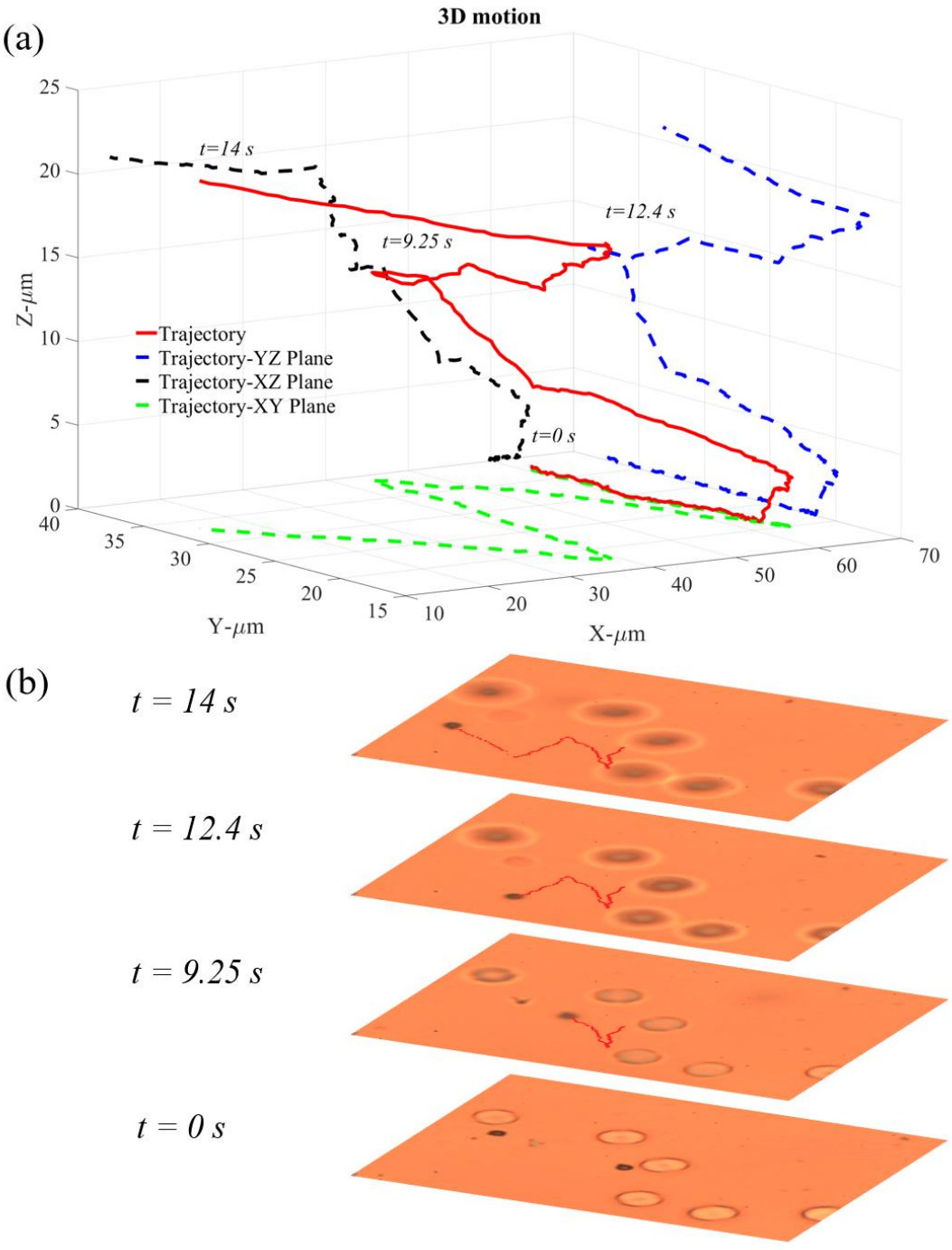

Fig. 4-7. 3D motion of single bead microrobot. (a) trajectory of microrobot. (b) experimental images at the different times shown in (a). Small black circular object is the microrobot, and the large white circular objects represent SU-8 reference structures.

4.2.5 3D Control for Specific Trajectory - Closed loop

3D closed loop control is more difficult and complicated than 2D and open loop control since randomly distributed microflows play a larger role in influencing the motion of the microrobot. Likewise, Brownian motion will also introduce noise to the 3D real-time tracking algorithm at such a small scale. After testing and evaluating the 3D motion evaluation in the previous section, we implemented it into our real-time closed loop control algorithm for 3D control. The power output in 3D control was set to 1.5 A. In Fig. 4-8, microrobots were oriented to move in 3D space for different patterns, with the corresponding 3D trajectories shown under each pattern. It is evident that the microrobot is moving in the positive *z*-direction due to its area dilation during focal plane transitions.

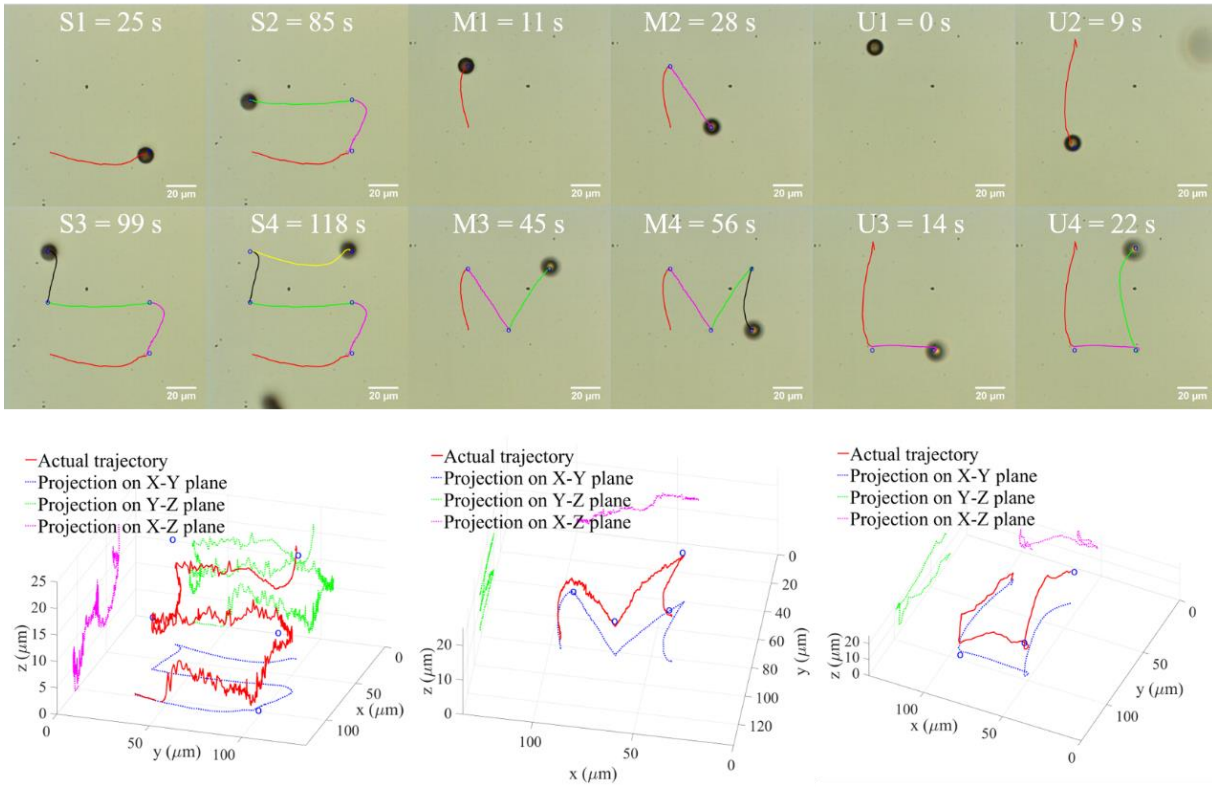

Fig. 4-8. 3D closed-loop control of trajectory '**SMU**'. Blue circles represent the desired locations on each trajectory. Different colors represent each trajectory between each pair of desired locations. The three bottom figures illustrate the specific trajectory above them with the projection on all three planes.

In trajectory '**S**', due to the relatively complicated pattern, the completion time was significantly longer than the other two patterns. We can see that the trajectory fluctuates heavily when the microrobot leaves the bottom plane. In the beginning, the microrobot stayed at $z = 0$ μm, but midway to the first desired point, it suddenly went up. The control strategy then directed it to move downward to reach the first target position. The height of the second desired point was set to 10 μm above the surface; the projection along *x*-*z* plane shows that the microrobot climbed to that height as well as moved towards the desired coordinate on *x*-*y* plane (magenta). It then maintained a height of 10 μm while moving along negative *y* direction (green) to reach the next point. The microrobot's position fluctuated periodically due to Brownian motion. However, when the microrobot was directed to climb to $z = 20$ μm, an external disturbance caused a drastic downward motion of the microrobot to a height of $z = 5$ μm; after that it started to climb up again and reached $z = 16$ μm while the coordinate on *x*-*y* plane was perfectly aligned. This can be seen at the junction of green and black trajectories in 'S3' of Fig. 4-8. The final target was set to have a height of $z = 20$ μm. While the microrobot maintained upward motion, it would often descend several micrometers at various points. Interestingly, the particle moved directly upward and reached the desired height only after approaching the destination in the *x*-*y* plane. This was the result of a greater force being applied in the positive *z*-direction to overcome the descending motion that happened randomly as the microrobot was approaching the target, which means the force components in the *x*-*y* plane were decreased and force component along *z*-direction was increased. Comparing to the '**S**' trajectory in 2D, this 3D trajectory has a better motion along the *x*-*y* plane; this may be a benefit from the absence of surface friction, however, the vertical motion from 10 μm to 20 μm was not ideal since microflows created excessive deviations from the desired

response. One thing needs to be pointed out here is that the trajectory variations between each way point can be improved by setting a shorter distance between each point or using a different control strategy with state control of both location and velocity.

4.2.5.1 Magnetic Force Analysis

The forces generation ability is investigated by applying Eq. (2-9) with data obtained from the experiments that had a stable fluid environment without the influence of microflow. From above, it is known that the 3D control of trajectory '**M**' is the most stable one, thus our calculation and analysis proceeded using this case. The black dashed vertical lines in each graph of Fig. 4-9 represent a change in the desired way point. Fig. 4-9(a) shows the current history during the whole experiment period, in which the current on the pair of coils in x_a was led in the negative direction for most of the time. By looking at the coordinate system in Fig. 2-1 and comparing it with Fig. 4-8 for '**M**', it is easy to find out that the main moving direction of the microrobot has a direction component along negative x_m, after coordinate transformation, the force vector in x_a is also negative, and the other two terms will change sign depending on the ongoing direction of motion. The current history alone can also indicate the ongoing motion based on the sign of each current component. The current, velocity, and force magnitudes drop at the dashed lines. This is because the microrobot approached the desired location and the controller decreased the power input proportionally as described in the previous discussion of the closed loop control. The maximum velocity of 6.2 μm/s happened on the black trajectory in 'M4' in Fig. 4-8. With a total input current of less than 2.5 A from the three power supplies, our magnetic tweezers produced a magnetic force as high as 800 pN using Eq. (2-9); this is much stronger than the force generation abilities demonstrated from other designs [71, 77, 79, 81] (200 pN or below) while still providing the large working space.

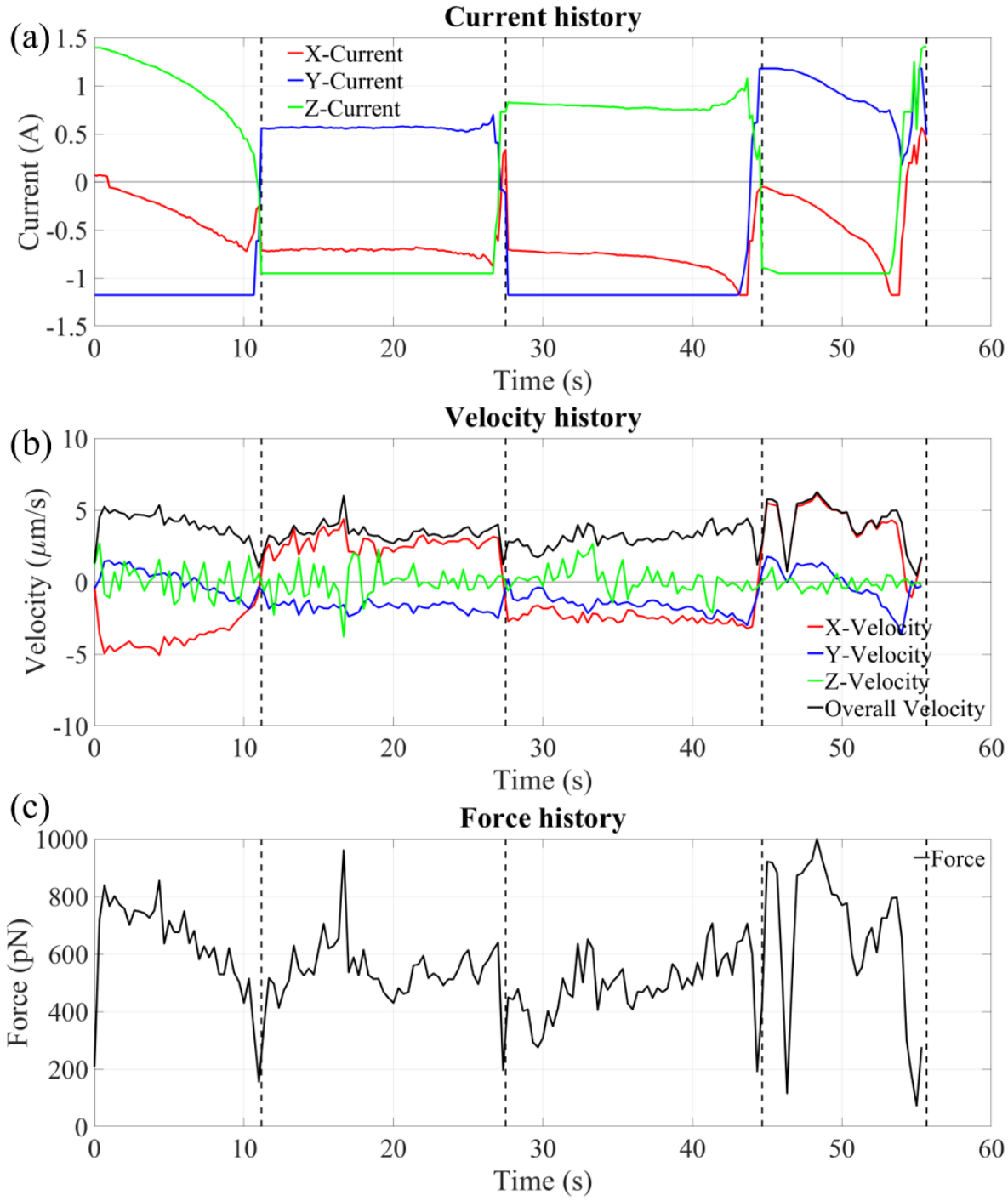

Fig. 4-9. 3D trajectory 'M' (a) Current history. (b) Velocity history. (c) Force history. Black dashed vertical lines represent a change in the desired way point by user.

4.2.6 Swarm Motion Control - Closed loop

As a necessary step towards deploying microrobots for applications like drug delivery, cell therapy and noninvasive surgery, the control and navigation of microrobot swarms towards a target location is not only required, but also fundamental to future research, especially for circumstances that require bulky payload to be transported wirelessly. A common method to produce microrobot swarm manipulation is to apply an external force or torque on the microrobot swarm with specific size or shape so that they can show homogenous or hetergenous behaviors as needed. In our work, microrobot swarm control using the magnetic tweezer system was proceeded by selecting one of the microrobot in the swarm and navigating it through the working space. As the properties such as size, weight and magnetization of the single bead microrobots were almost identical, they showed similar behaviors under the same magnetic gradient field, though there still exist deviations due to the uncertainties within the fluid medium.

For each test, three microrobots were selected and their trajectories were marked in three different line colors. The 3D swarm control trajectories in 3D view were also generated to represent the thorough motion of each microrobot. For each experiment shown below, the steered microrobot usually started on the bottom of the substrate unless specifically mentioned, while the other two may not have started on the same focal plane. For microrobots with same material but of different geometric sizes, the larger ones will generate a higher magnetic force due to a greater magnetic dipole.

Fig. 4-10 shows the overview of microrobot swarm control process. A swarm of microrobots is detected in the working space at the starting point and marked by image processing and a tracking module. The tracking location can be obtained by either using one microrobot's centroid in the swarm or considering the center of mass for the whole swarm as the centroid. The

controller provide a controlled power output to generate the specific force vector correlated to the target locations until microrobots reach to that position. On the way to the target, Brownian motion and microflow will constantly affect the motion of the swarm, but the control algorithm will continuously self-correct the force vector to assure the microrobots continue moving in the right direction. Finally they end up in the final target location and process is completed.

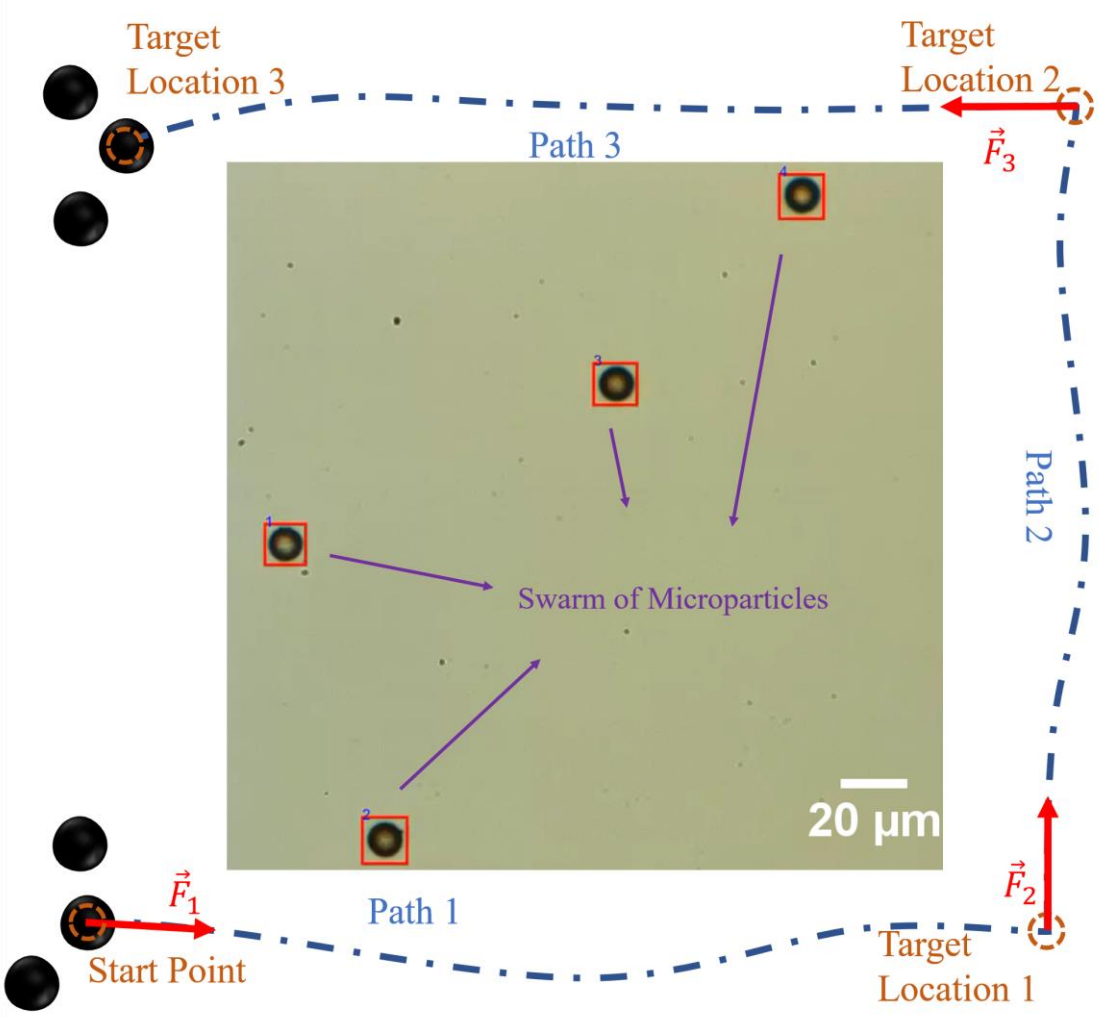

Fig. 4-10. Swarm control experiment overview. The swarm of microrobots departs from the starting point, where the force vectors $\vec{F}_i$ are updated according to the given target location. The central figure shows the detail of a real-time experiment image. All detected microrobots are enclosed in the red box with index number on its upper left corner for recognition. The swarm is then guided to a series of arbitrary target coordinates that can be set by the user in all three dimensions.

4.2.6.1 2D Swarm Motion-closed loop

The total size of field of view from the camera is 278 × 278 μm^2 in the *x*-*y* plane, with a trackable *z*-direction of about 30 μm. Some of the microrobots are not on the same focal plane throughout the experiment, however, the magnetic field gradients act as uniform inputs within the working space [39]. Fig. 4-11 shows the 2D swarm control result of navigating a microrobot swarm to follow specific patterns of 'L', 'o', 'v' and 'e'. This was chosen in honor of Valentine's day. The target locations in each pattern were set such that the turning points were on the *x*-*y* plane and the *z*-component was equal to zero. The control power input was set such that it did not exceed 1.5 A in each power supply. This value was determined from experiments in earlier work to prevent the temperature in the working space from overheating as well as providing enough power to allow microrobos to move at a suitable speed.

The swarm of microrobots in pattern 'L' shows excellent uniformity as all three microrobots have nearly identical routes, which indicates the existence of stable fluid environment and proves the uniform magnetic force generated within the working space when microrobot have homogeneous properties. In the 'o' pattern, most of the trajectories followed the shape, where the only obvious difference is at the end of the navigation. The magenta microrobot went through its original location and moved to the right for a short distance, while the green one stopped exactly at its starting point and the blue one experienced insufficient motion to reach to the final point. This motion above indicates the diversity of behavior when microrobots with heterogeneous properties respond to same magnetic gradient field. The overall routes in the letter 'v' also follow the shape, but one thing that should be noted is that the blue microrobot's path is slightly longer than the other two, this is due to the density profile along *z* direction in the medium. Tween 20 solution (a Newtonian surfactant used to decrease the friction on substrate surface, Brookfield

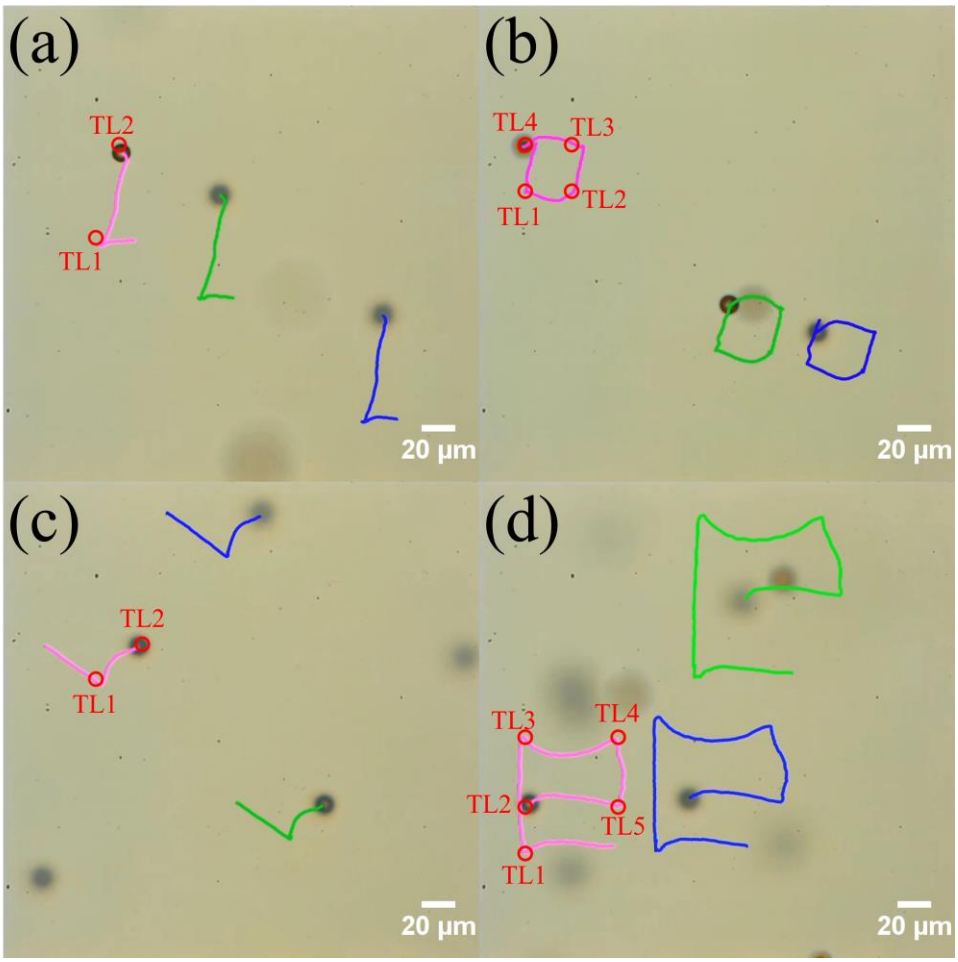

Fig. 4-11. 2D swarm control trajectory of 'Love' in (a)-(d). The finishing time for each pattern is 59 s, 80 s, 24 s and 166 s, respectively. 'TL' refers to target location. All particles were able to perform similar trajectories, with deviations resulting from internal flows or height differences in the sample.

Viscosity ranges between 370-430 cps (25 °C, neat)) has higher density and naturally sinks to the bottom of the test domain, resulting in higher drag force within that area. Because the blue microrobot is in a higher position than the other two microrobots, and experiencing an equal amount of magnetic force, we can infer that its velocity is faster than those located in the lower layer according to Eq. (2-9) as Tween 20 on the bottom has higher viscosity. For pattern 'e', the magenta microrobot is the lowest and the green microrobot is the highest in terms of depth. The difference in height again reflects the trajectory shape difference. The trajectory length of the green microrobot has the longest path followed by the blue and magenta microrobot trajectories in

decreasing length. However, all trajectories still form the distinctive pattern on the control level, and this heterogeneity of velocity profile depending on the depth of microrobots in the swarm can be utilized in future more complex control tasks, such as navigating heterogeneous microrobots with a sequence of steps to reach to different target based on their velocity difference. The closed-loop control performance in 2D always showed good navigation and could manipulate a microrobot swarm through a desired pattern.

4.2.6.2 3D Swarm Motion-closed loop

Closed-loop control in 3D is more complex than in the 2D case, due to the inclusion of *z*-direction motion. Also, Brownian motion, combined with the existence of random microflows, leads to a very unstable surrounding environment that can affect the movement of microrobots significantly. The same maximum current output of 1.5 A was also applied to the experiments in 3D. The recorded video frames and relevant 3D trajectory analysis are shown in Fig. 4-12, in which the way points are labelled as black circles.

The movement of 'L' was set to move to z = 5 μm at the corner and then go up to z = 10 μm. The selected microrobot in the swarm was at first slightly higher than 5 μm, but it dropped down around that height while also approaching the target *x-y* plane. The other two followed the same trend and showed similar motion. The magenta microrobot had a relatively longer path in 'L' due to the higher starting point and larger particle size. All the trajectories were smooth and stable as shown in the 3D view plot Fig. 4-12(a).

In 'o' trajectory, the influence of a microflow emerged. The starting point of the chosen microrobot was at 10 μm level with the rest in the swarm below it. When the first target location with z = 15 μm (left-bottom corner on *x-y* plane) was reached, the swarm had some fluctuations

but soon was stabilized and then headed to the next desired point with z = 20 μm. The third target point was on the same level with the second one, and the swarm reached to as high as 26 μm at the halfway point, but then lowered to the expected point, from where it then set off to the original point at the 10 μm level. We can clearly see that red microrobot surpass the other two in total route length as it started in a higher position. The swarm proceeded to the preset points even though there were disturbances on the way.

Pattern ‘v’ was comparative simpler than the ‘L’ in the experimental data. All three individuals in the swarm started from the bottom plane in this case. The first desired point was at z = 5 μm, to lead the microrobot moving to the bottom center in Fig. 4-12(c). The swarm then navigated to the height of 20 μm. The final motion was oscillating and down but the microrobots all ended up between 22 to 24 μm in the z-direction. Each of the trajectories had almost same length as shown in t4 = 42 s in Fig. 4-12(c).

The letter ‘e’ was the most complicated pattern to achieve as it had the most turns on the route with longest length. The first two way points were on the z = 0 μm plane. The swarm was then guided to the height of 20 μm directly to the upper-left corner. The rest of the trajectories were stable and showed the swarm of microrobots passing through the last two target points at z = 10 μm. The whole movement has better performance than the one displayed in ‘o’ as there was no drastic bouncing motion and fluctuations only happened at the beginning of the operation.

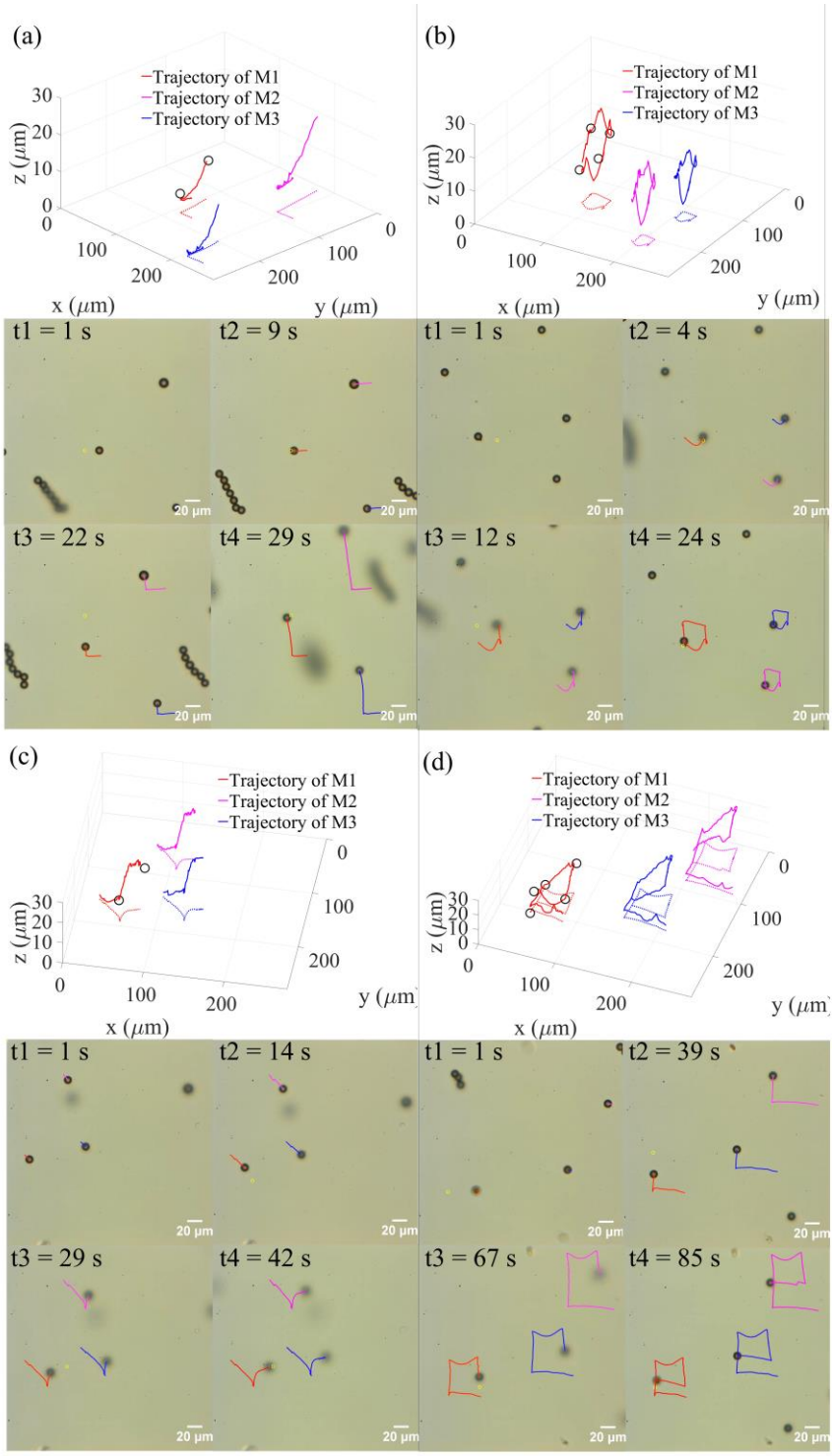

Fig. 4-12. 3D swarm control trajectory of 'Love' in (a)-(d) with 3D trajectory plots above each of them. Below each 3D plot are four images that show the steps of trajectories. Black circles shown in each 3D trajectory are the target locations at each step. The projection of each trajectory is shown on the bottom of the *x*-*y* plane in each 3D plot. 'M1'- 'M3' refers to microrobots 1-3. The trajectory colors in 3D view figures are consistent with the experimental image representing them below. t1-t4 represent time points.

4.2.6.3 Discussion

According to Fig. 4-11 and Fig. 4-12, it is apparent that the time used in 3D swarm control to produce similar patterns was less than half of that in 2D under same power output restriction. This was achieved by the lack of drag force far from the surface. However, the 2D motion had the benefit of having a steadier trajectory. The performance of the *x-y* plane motion in both assignments can be considered satisfactory, and swarms can reach to the designated height within acceptable error range of less than 4 μm.

This section illustrated experiments involving microrobot swarm control in both 2D and 3D. 3D views of microrobot swarm motion trajectories were created using a focal plane area analysis of the microrobots and were displayed alongside real-time experimental data. This work has major benefits for swarm control related tasks, showing that not only can similar microrobots act homogeneously under a uniform input, but can also be reliably actuated to perform arbitrary 3D motion. While there were some issues with internal flows and fluidic heterogeneity, the microrobot swarms performed quite well in achieving their desired trajectories. Furthermore, the results can guide future development of control systems for microrobotics and advance towards practically controllable magnetically actuated microrobots in *in vivo* environment for drug delivery and cell therapy applications.

4.3 Conclusion

In this chapter, various experiments with different purposes were completed. The controllability and force generation capability of magnetic tweezer system with multiple directional magnetic forces was demonstrated in Newtonian and non-Newtonian fluid environments.

For open loop and closed loop control of individual microrobot, experiments of single and multi-bead microrobots performing desired 2D/3D trajectories, obstacle avoidance in non-Newtonian, and opposing microflows under the magnetic force were conducted. Generally, for the same type of magnetic microbead, microrobots formed of more microbeads generated higher magnetic force together with the magnetic tweezer system. In experiments for both 2D and 3D control, the results were analyzed to illustrate the flexible controllability and powerful force generation capabilities. Force generation capability was shown through the phenomena of resisting microflow and theoretical calculation using Stoke's law.

For closed loop swarm control, the demonstration was proceeded by showing experiments involving microrobot swarm in both 2D and 3D. 3D views of the microrobot swarm motion trajectories were created using a focal plane area analysis of the microrobot and were displayed alongside real-time experimental data. This work has major benefits for swarm control related tasks, showing that while similar microrobots act homogeneously under a uniform input, they can also be reliably actuated to perform arbitrary 3D motion.

Comparing with works from other groups, this work is the first to thoroughly concentrate on microrobotics field and extensively investigate the magnetic field simulation of the magnetic tweezer system, conduct the 2D/3D motion control of microrobot in both Newtonian and non-Newtonian fluid environments with open loop and closed loop control strategies, and explore the performance of swarm control of microrobots with the magnetic tweezer system.

CHAPTER 5 OTHER RELATED WORK

5.1 Haptics Integration with A Magnetic Tweezer System for Teleoperation

5.1.1 Introduction

Microrobot applications in both *in vitro* and *in vivo* environments have been interesting topics in the biomedical research field since they have the potential to revolutionize the healthcare industry [29-32, 39]. When microrobots are combined with wireless control techniques, applications like *in situ* sensing, cell therapy, micromanipulation, and targeted/localized drug delivery can be achieved to transform the processes of minimally invasive surgery, drug delivery, and biopsy procedures. Wireless control within such a small scale is limited to optical, electrical, and magnetic techniques, which have been deployed in many implementations such as electromagnetic coil systems, photonic force microscopy, optical tweezer systems, and magnetic tweezer systems [34, 36, 41, 60].

Currently, most microrobot systems concentrate on the control performance of the microrobot while the human interaction aspect is not well investigated, which is essential in biomedical applications as medical professionals or researchers play a vital role in the operations [94, 95]. It is important to build up the interaction between control systems and human operators so that one can give guidance to the operation when the other one is confronted with problematic scenario.

Haptic force feedback techniques enable users to feel the operation physically and intuitively with their hands and has been verified to be a significant tool to achieve teleoperation

of robotic systems [94-102]. Advantages of a haptic system have been confirmed in cardiothoracic procedures [103, 104], microneedle positioning [105], telerobotic catheter insertion [106], palpation [107], cell injection [108, 109], and even micro-manipulation [110-113]. Multiple haptic feedback devices have also been developed so far to control and manipulate microrobot systems. Haptic sensations from interaction between a self-folding soft magnetic gripper and its environment were investigated in [113], where the human operator intuitively controlled a magnetic gripper using a haptic interface. In terms of visual sensing by the haptic device, Pacchierotti *et al.* [111] employed a haptic interface for a user to remotely control self-propelled microrobots to target a goal with particle-filter visual sensing that visually tracks the position of the microrobots. Asgari *et al.* [114] provided a haptic force generation method for a microrobotic cell injection procedure. A 3D particle-based model was proposed to simulate the deformation of the cell membrane and corresponding cellular forces. Faroque *et al.* [115] proposed a large-scale virtual reality training system with a haptic device, in which virtual fixtures and force feedback was generated for the microrobotic cell injection procedure to guide the user for virtual micropipette operations by force feedback. So far, the usability and reliability of haptic interactions with the microrobot system have been significantly advanced for potential human operators. However, most of the existing techniques provide haptic force feedback through either an ambient interaction or direct contact force with the targeted object. Moreover, onsite interactions have been typically prioritized, while remote operations over large distances have not been thoroughly explored, despite the fact that remote control of the microrobot applications with haptic interactions is crucial to extending the utility of remote therapy and surgery.

In this work [116], we constructed a microrobot control framework using haptic interaction based on the networked teleoperation between our magnetic tweezer system and a haptic interface

located in Washington, D.C.. Haptic guidance force for near-optimal path following and haptic force feedback for real-time interactions with the environments were implemented in teleoperation settings over two facilities more than 2000 km apart. An attractive force is utilized to achieve haptic guidance for path following and obstacle avoidance, while a repulsive force based on the potential field and virtual-proxy force was implemented to produce the haptic interaction that allowed users to feel the virtual environments. We provide the haptic interaction forces of both ambient and contact interactions to improve usability. The proposed system includes an image-based 3D haptic rendering algorithm, which reconstructs artificial 3D objects by reflecting dynamic shape changes of the planar objects for practical haptic interaction. The 2D image was transmitted remotely (real-time transmission between George Washington University in Washington, D.C. and Southern Methodist University in Dallas, Texas, approx. 2,138 km apart) from magnetic tweezer system, with multiple arbitrarily shaped objects within the field-of-view, to create real-time haptic force feedback and enable the manipulation of microrobots. The notable contributions of this work includes:

1) Haptic interactions for near-optimal path following, object contact interaction with proxy-force, and object ambient interaction with an artificial potential field are implemented to assist microrobot controls.

2) Dynamic path planning is applied based on the user's intended haptic operation, in which the effective path with obstacle avoidance is dynamically generated and updated.

3) 3D object reconstruction is accomplished by reflecting dynamic shape changes of the objects in a 2D planar image using the model-free haptic rendering.

4) A closed-loop teleoperation system is achieved with a wireless communication between the magnetic tweezer system and the haptic interface system.

5) The practical system is implemented and tested with a commercial haptic device in macroscale and a magnetic tweezer in microscale under practical distance data communications.

5.1.2 Illustration of Haptic and Magnetic Tweezer System

The integration of a magnetic tweezer system with a haptic interface is illustrated in Fig. 5-1, where the two systems communicate with a TCP/IP network communication protocol. The haptic interface generates the haptic feedback force based on the motion of microrobots and environmental objects, which is received from the magnetic tweezer system. The control command is then sent back to microrobots for navigation. Haptic rendering, image processing, path planning, and network communication were developed in C++, while the magnetic tweezer control, microscopic image processing, and network communication were established in MATLAB.

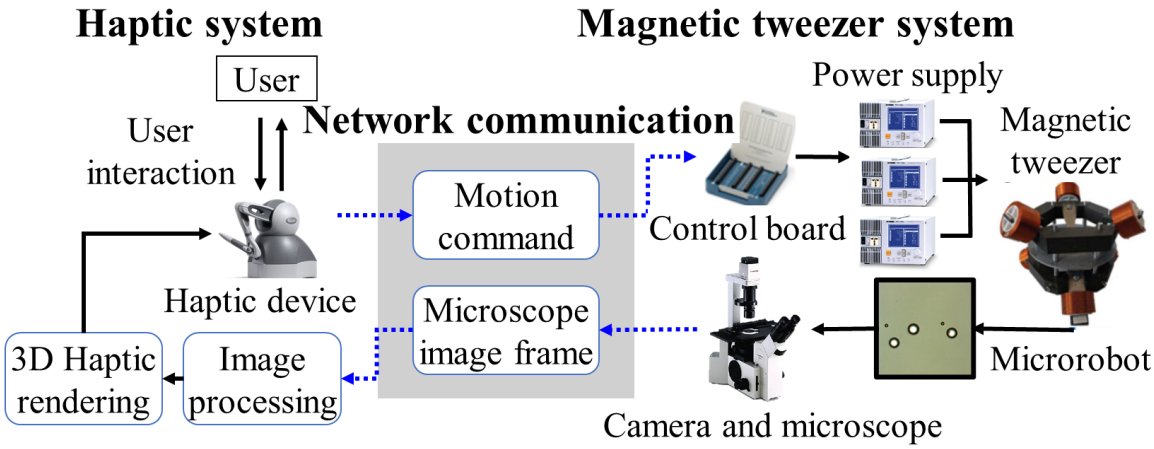

Fig. 5-1. Microrobot haptic interaction system. The left part is a haptic interface, and the right part is a magnetic tweezer system. Data flow of image frames and control commands are shown as arrow directions.

The haptic interface (Geomagic touch haptic device, 3D Systems, Rock Hill, SC) is operated by a 6-DOF (degree of freedom) pen-type stylus gripper, which is serially connected to the haptic device body. The device can measure the 6-DOF position and orientation of the user's operation and generate 3-DOF force feedback in *x*, *y*, and *z* directions. The haptic control software is developed using the open-source haptic library CHAI3D to ensure the compatibility over the multiple operating systems and diverse haptic device platforms.

5.1.3 Teleoperation Controls

5.1.3.1 Teleoperation Scheme

The haptic-microrobot teleoperation system was designed by an impedance control scheme with a position-based force rendering. The impedance control measures the motion of the haptic device to manipulate the force of the magnetic tweezer. It has relatively low inertia and is highly back-drivable compared to admittance control. The equation of motion of the microrobot in 3D space can be derived as:

$$m\ddot{\vec{x}} - \vec{f}_d = \vec{f}_m \tag{5-1}$$

where m is the mass of the microrobot, and $\vec{f}_d$ and $\vec{f}_m$ are drag and magnetic forces, respectively. Since the force applied to the microrobot are determined by the displacement of the haptic interface, the magnitude of the magnetic force $\vec{f}_m = K\vec{x}_h$, where $\vec{x}_h$ is the haptic device displacement in 3D. $K = 1$ is the scaling constant to map the magnetic tweezer pixel workspace to the haptic interface virtual workspace, and the projection between haptic device's stylus in physical world and virtual environment is determined by the platform automatically. Gravity was negligible as high concentration NaCl solution (20% w/v) was used to prevent sedimentation. Adhesive force

resulting from Tween 20 on the substrate surface is included in the drag force term ($\vec{f}_d$) of the NaCl solution, and friction is negligible because the microrobots are moving above the glass slide.

Reliable operations for the teleoperation environments can be assumed since the communication was fast enough for the microrobots' operation via the haptic device (average time delay = 45.47 ms/frame with SD (standard deviation) = 27.02 ms/frame for transmitting series of 512×512 color images). The microrobots were operated at a micro-scaled workspace with relatively slow speed (approx. 2~3 $\mu m/s$ with maximum magnetic force) compared to the haptic operation. The slower speed was based on the power limit preset in the magnetic tweezer system. Therefore, we can guarantee the *in-situ* perception of the haptic feedback for navigation and transportation of the microrobots wirelessly by referring the fact that f_m is zero when x_h is zero, so that the drag force f_d in Eq. (5-1) will dissipate the energy completely. The acceleration term in Eq. (5-1) will be negligible due to the extremely small mass, and very slow and steady speed of the microrobots, which will cause the acceleration to be practically zero. On top of that, a viscosity force feedback was implemented to the haptic device to reduce the instability and limit the control input speed of the haptic operation by preventing abrupt motions of the haptic user.

5.1.3.2 Network Communication

Sufficient speed and reliability of the data communication are important for the stable operation of a bilateral haptic-microrobot interaction system. The network communication scheme of our proposed system is displayed in Fig. 5-1. Microrobot haptic interaction system. The left part is a haptic interface, and the right part is a magnetic tweezer system. Data flow of image frames and control commands are shown as arrow directions. Fig. 5-1with blue dot lines. The raw color image data from the magnetic tweezer was encoded into JPEG format to compress the data size

dramatically while minimizing the compression time. The communication data packet from the magnetic tweezer system to the haptic interface side was designed with three sub-components—header, body, and end bits—to ensure the correct reception of data in real-time. Header bits contain the position of the user-selected microrobot, and body bits encompass the compressed image data. Since the binary format data size of the encoded color image varies based on each image frame, the size of the binary format data is communicated prior to the binary image data in the body bits. The end bits are transmitted to notify the end of each packet. The binary format data of the color image is then decoded to rebuild the color image at the receiver side. In the opposite direction, the control command by the haptic device is transmitted to the magnetic tweezer side. The control command is composed of a 3D direction vector and a scalar for the force magnitude. To guarantee the reliability of the bidirectional communication, data packet check and confirmation protocols are applied. The communication data update rate is fixed as 10 frames/s by considering the stable communication and continuous haptic operations for intuitive control of the teleoperation system.

5.1.4 Haptic Feedback Implementation

5.1.4.1 Object Classification and 3D Volume Reconstruction

After receiving the raw image, the haptic interface side classifies all objects by their size information obtained through image processing. The diameter of a single bead microrobot is approximately 10.6 μm while that of the environmental objects ranged from 27.0 to 32.0 μm. Note that a color detection by the HSV (Hue, Saturation, Value) image was deployed at the haptics interface side for the swarm operation of the microrobots in Experiment 3 in section 5.1.6.

As the received image is in 2D, the visually identified objects (microrobots and obstacles) need to be reconstructed to 3D objects for the spatial haptic rendering. Using positions and

diameters of the microrobots in the 2D image, the 3D volume reconstruction was processed by converting 2D circular objects to 3D spherical objects located at the same position on the *x-y* plane with initial *z*-depth as zero, and the *z*-depth information of the microrobot was updated from magnetic tweezer side as the experiment proceeded using the relationship between area size and *z*-depth determined in section 4.2.4. The 3D volumized environmental objects are reconstructed using ellipsoidal 3D cloud points. Although the environmental objects used in the experiments are assumed as spheres, the ellipsoid was used as a potential extension for general applications. By adjusting the radius on the *z*-axis, the different shapes of the environmental objects can be reconstructed more effectively in the general case. Cloud points, which represent components of the surface of a 3D ellipsoid, are generated at the same position of the 2D environmental objects with a circular radius on the *x-y* plane. Radius of environmental object in virtual environment on *x-y* plane is set to be larger than that in actual environment to ensure early intervention of path planning and obstacle avoidance operations. The radius of the ellipsoid on the *z*-axis is defined as a quarter of the circular radius to prevent any presence of a large empty space of the 3D reconstructed points. Part of the 3D ellipsoid points is excluded by filtering out the points that are

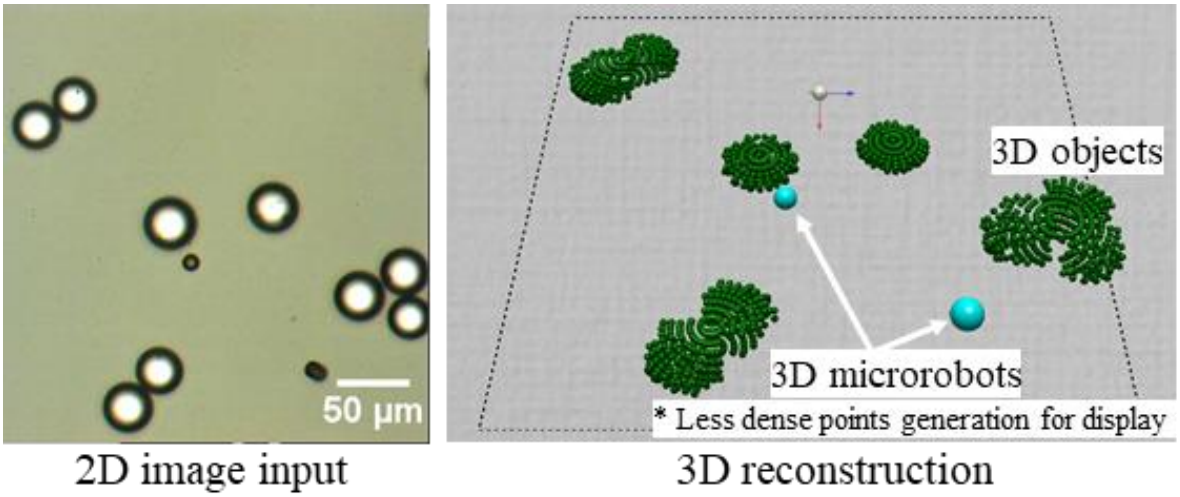

Fig. 5-2. 3D volume reconstruction (microrobots and environmental objects). 3D cloud points reconstruction by 2D microscope input image.

not overlaid on the 2D object (Fig. 5-2). This procedure upgrades the environmental objects in the 2D image to a higher degree (3D) objects by reflecting different objects' shape, making haptic rendering in 3D space possible.

5.1.4.2 Artificial Potential Field Force

The haptic force feedback consists of two different forces, the ambient force near the environmental objects and the contact force. Ambient force is generated by a repulsive artificial potential field while the contact force is generated by a virtual proxy force. Users can feel the haptic feedback when the haptic probe enters the potential field of the objects. The haptic workspace is treated as a 3D grid where the 3D cloud points of the environmental objects are superimposed. Each grid cell occupied by the point contributes to a repulsive potential field.

Fig. 5-3 illustrates the 3D potential fields around single particles for the haptic motion control space. The repulsive haptic forces are designed to be centered inside the obstacle in order

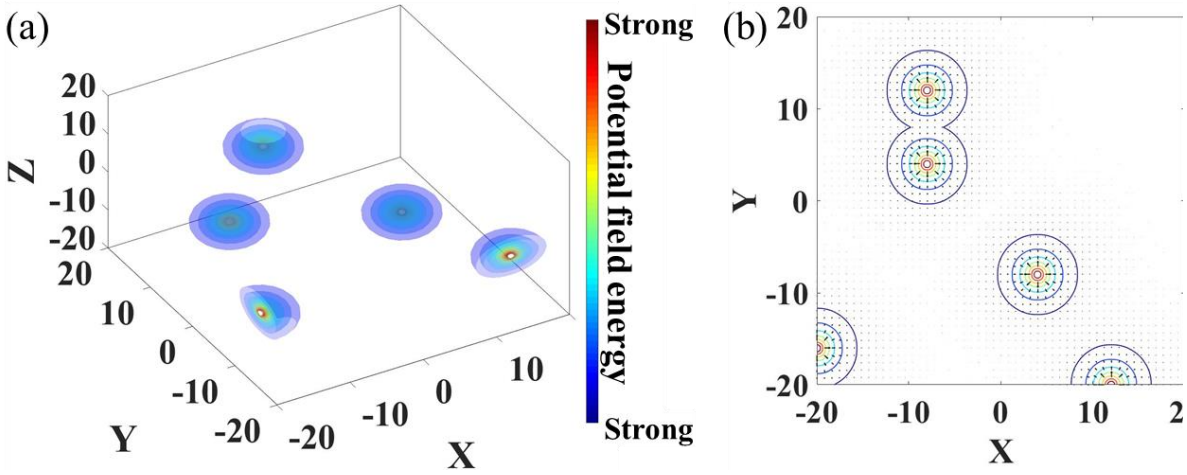

Fig. 5-3. Illustrations of the repulsive potential field around 3D objects. (a) 3D repulsive potential fields and (b) potential fields as seen on the *x*-*y* plane.

to prevent the haptic probe penetrating the virtual space inside of the obstacle in the mapped haptic workspace. The repulsive potential field U_{ref} can be generated by occupied cells p_i as:

$$U_{ref}(x, x_{pi}) = \begin{cases} \frac{1}{2}\eta\left(\frac{1}{\|x - x_{pi}\|} - \frac{1}{\rho_0}\right), & \|x - x_{pi}\| \le \rho_0 \\ 0, & otherwise \end{cases} \tag{5-2}$$

where x is the position of the haptic probe, x_{pi} is the position of occupied cells, η is a positive scaling factor, and ρ_0 is the range of influence. The force is computed by the negative gradient of the potential field. The repulsive force F_i exerted by each cell p_i and the total repulsive potential field U of all occupied cells can be written as:

$$F_i(x, x_{pi}) = -\nabla U_{ref}(x, x_{pi}) \tag{5-3}$$

$$U = \sum_{p_i} U_{ref}(x, x_{pi}) \tag{5-4}$$

Therefore, the total repulsive force on the haptic probe by the 3D occupied cells can be calculated as:

$$F = -\sum_{p_i} \nabla U_{ref}(x, x_{pi}) \tag{5-5}$$

The center of mass of the occupied grid cells, within a search boundary set arbitrarily by user from the haptic probe, is used to compute the direction vector and magnitude for the potential field force. Fig. 5-4 shows the potential field force generation strategy.

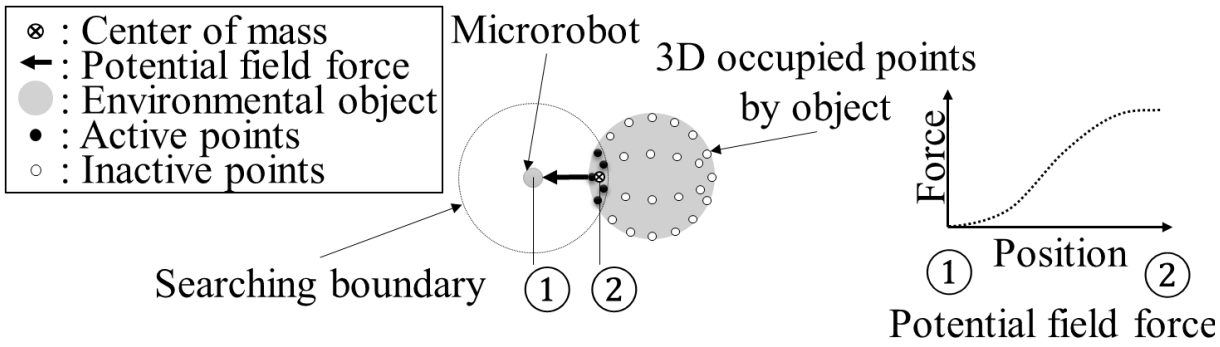

Fig. 5-4. Potential field force generation with active occupied points.

5.1.4.3 Virtual-Proxy Force

The proxy-based haptic interaction is employed to generate a contact force from the surface of the objects that feels like a relatively stiff surface to the user. This approach, which uses the notion of a virtual proxy, is widely used in haptic interactions [117-119]. The force response, $\vec{f}_f$, of the haptic device in 3D using the spring-damper model that connects the virtual proxy and the haptic probe can be written as:

$$\vec{f}_f = k(\vec{x}_{proxy} - \vec{x}_{probe}) + d(\vec{v}_{proxy} - \vec{v}_{probe}) \tag{5-6}$$

where $\vec{x}_{probe}$ and $\vec{x}_{proxy}$ are the positions of the haptic probe and the virtual proxy in 3D while $\vec{v}_{probe}$ and $\vec{v}_{proxy}$ are the velocities of the virtual proxy and the haptic probe in 3D, respectively. k is the stiffness constant and d is the damping constant. Empirical parameters of $k = 280\ \mathrm{N/mm}$ and $d = 2\ \mathrm{N \cdot s/mm}$ were selected for the best performance and user experience of the teleoperation control of the proposed system.

Forces by the potential field and virtual proxy on the 3D environmental objects are transmitted to the haptic interface side to generate the haptic feedback force when the haptic probe is approaching and touching the environmental objects. Once the haptic probe enters the potential field area, the user starts to feel the repulsive forces increasing proportionally as the haptic probe is getting into the high gradient region of the object's potential field. Moreover, when the haptic probe touches the surface of the environmental objects, the proxy force is added to produce a stiff contact force for better intuitive haptic interaction.

5.1.4.4 Computational Complexity Reduction Strategy

To provide seamless haptic interaction (quality of service) while enhancing the networked teleoperation performances, a computational cost reduction strategy with efficient search algorithm was applied to achieve smooth operations and intuitive usability. Any environmental objects within a certain spherical boundary from the haptic probe are explored rather than searching the full range of the workspace to detect the objects. Moreover, a region-of-interest (ROI) based local computations are employed that utilizes only part of the 3D points of the active environmental objects (active points in Fig. 5-4) when they are within a search boundary from the haptic probe. These strategies reduce the computational complexity to ensure continuous and fast operation.

5.1.5 Dynamic Path Planning with Haptic Operation

Dynamic path planning of the haptic-microrobot system produces an effective path adaptively in the realistic haptic environment. An instant target is created based on the dynamic movement of the haptic device so that the near-optimal path from the current haptic position to the instant target is dynamically generated by reflecting the user's intention of the haptic control. When the haptic device moves, the near-optimal path is locally generated in the *x*-*y* plane, and the path following force for the haptic device is activated. In the path following feature that the haptic device guides microrobot automatically, *z*-direction motion is assumed to be zero.

5.1.5.1 Path Planning Field Generation

A path planning workspace is modeled as a finite number of identical square cells based on the pixel coordinates of the received image. The square cells are occupied with environmental objects or empty. The repulsive force field by the environmental objects is implemented using the

Gaussian filtering so that image depth of the pixel values of the Gaussian blurred image can be

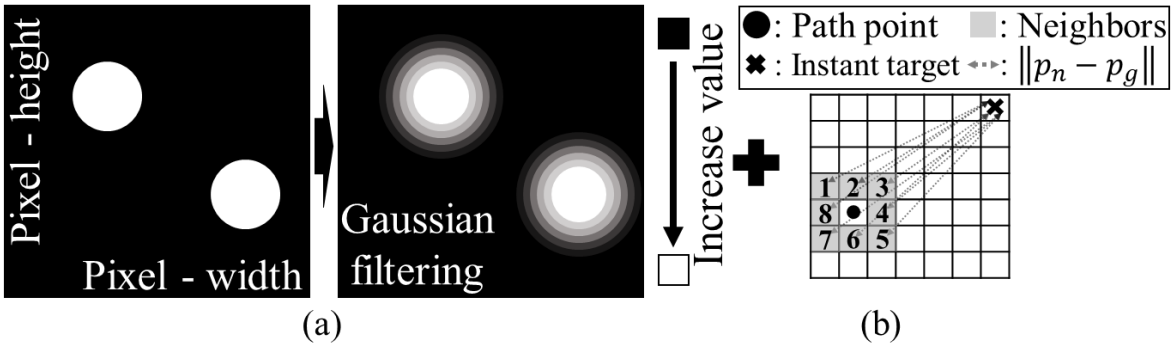

Fig. 5-5. Force field for the path generation. (a) Repulsive force field generated by Gaussian filtering on obstacles and (b) attractive force field by the instant target.

treated as the magnitude of the repulsive force field. The attractive force field U_a to the instant target is defined by the distance between a neighbor cells p_n of the current way point p_c and instant target p_g as:

$$U_a = \frac{1}{2}\xi \cdot \|p_n - p_g\|^2, \;\; p_n \in N, neighbors\ of\ p_c \tag{5-7}$$

where ξ is the magnification constant. The force field for path planning is the combination of the repulsive and attractive force fields as shown in Fig. 5-5.

5.1.5.2 Instant Target Creation

The real-time path generation reflecting the user's intentions of the haptic operation is processed by dynamically creating an instant target. We assume that the user is mostly aiming to keep the haptic movement in the direction similar to previous motions. Fig. 5-6(a) represents the instant target creation. The position history of the haptic device is recorded, and differences of the position by time are averaged to estimate the future location of the haptic motion. Instant target p_{it} is a certain step $(\alpha \cdot v_c)$ forward from current haptic position p_t. Fig. 5-6(b) illustrates the instant target creation outside of any environmental objects, with which the algorithm avoids the

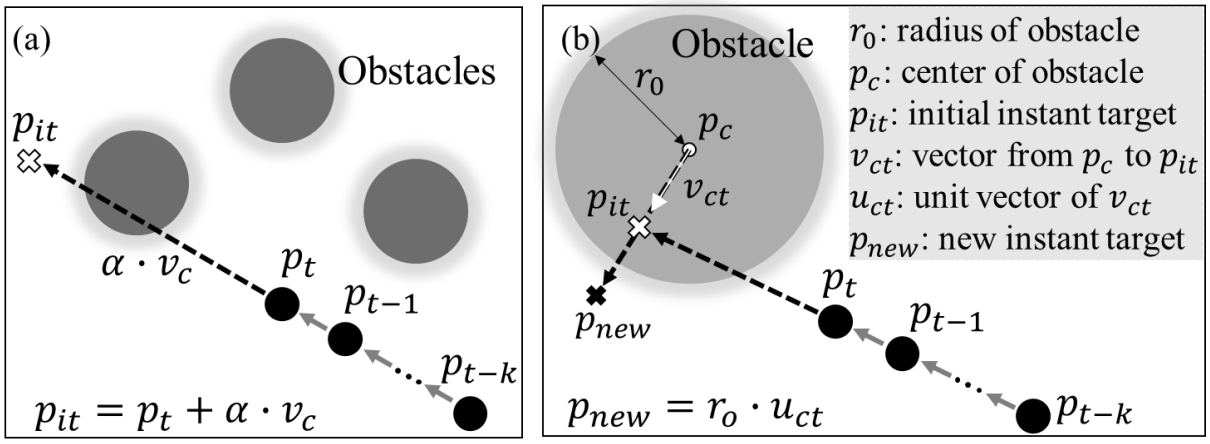

Fig. 5-6. Instant target creation. (a) Instant target creation strategy and (b) target creation outside of environmental object.

path generation directing to the collision course with the environmental objects. If an instant target is created inside of the obstacle during the instant target creation process, a new target is recreated at the closest boundary of the obstacle using the original target point (p_{it}), radius (r_0), and center position (p_c) of the related obstacle, and then replaced with the p_{it} to create the instant target outside of the obstacle as shown in Fig. 5-6(b). Additionally, the instant target generation is temporarily paused when the user closely detours the environmental objects since the algorithm can create an unintended target due to the circular detouring motion of the haptic operation.

5.1.5.3 Path Planning

After creating the instant target, the path planning algorithm generates a guidance path from the current haptic position to the target while avoiding environmental objects. Each intermediate path point is selected among the neighbors of the current path point. The neighbors of the current path point are defined with 12 grid cells, with consideration of the computational cost and path smoothness, as shown in Fig. 5-7(a). The path generation algorithm iteratively selects

the next path point until the instant target is reached. The next path point p_f is selected by minimizing a cost as:

$$p_f = \underset{p_n \in N}{\operatorname{argmin}}\{w_t \cdot U_a(p_n) + w_o \cdot U_r(p_n)\} \tag{5-8}$$

where N is all neighbors of current path point p_c, and p_n is neighbors $(p_n^1, p_n^2, \dots, p_n^{12})$. The cost is defined by the repulsive and attractive force fields by the environmental objects and instant target with adjustable weights. $U_a(x)$ and $U_r(x)$ are attractive and repulsive force fields, respectively. Fig. 5-7(b-c) illustrates the path planning steps and path generation.

Due to the discretization of workspace in the proposed path planning, the path can be trapped in certain grids by repeatedly selecting the next path with the same sequence. The proposed

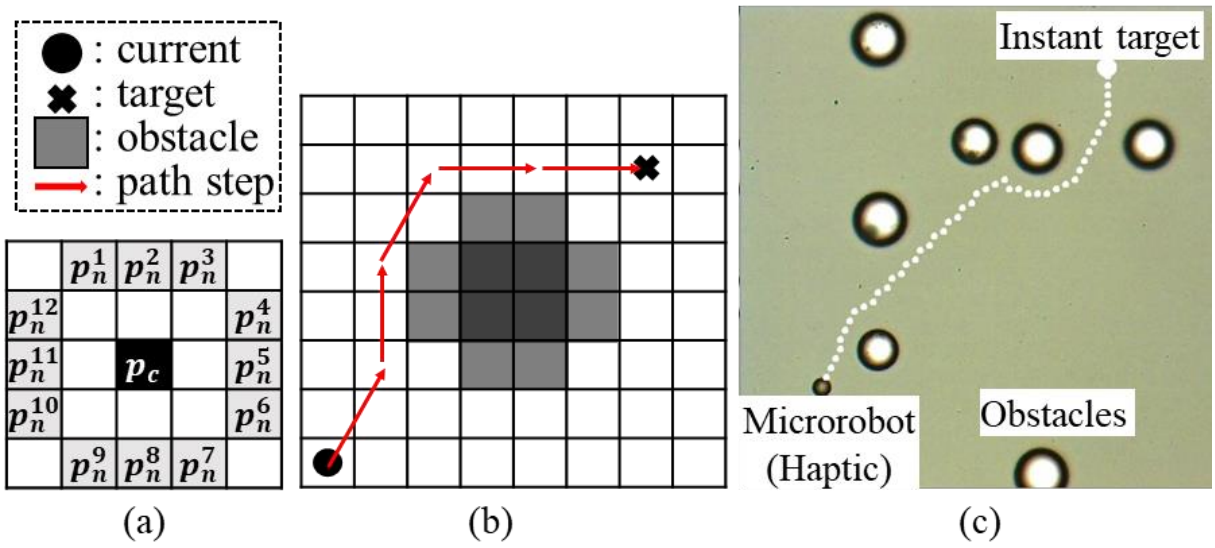

Fig. 5-7. Dynamic path planning of the microrobot navigation. (a) Defined neighbors, $n = 12$. (b) Path step from the start to a target and (c) path generation example.

algorithm processes a random selection of the next path if the path selection memory shows only repeated transits between two neighbors and does not reduce the distance to the target. Haptic force guidance to follow the effective path assists the user to operate the microrobot with the haptic feedback. In the dynamic path planning, the intermediate path point is gradually generated from

the current haptic position to the target. At that time, an attractive force is applied to the haptic device to minimize the distance from the current haptic position to the intermediate path point. Eventually, the user can feel the haptic guidance force during path generation until the haptic probe reaches the target. If a new instant target is generated during the path following, then a new path planning from the current haptic position to the new target is triggered.

5.1.6 Experiments and Results

The experimental design and processes are described as follows. Three experiments were designed to evaluate the proposed framework: (1) microrobot manipulation with haptic feedback, (2) dynamic path planning with the path following force, and (3) micro-object transportation. In all experiments, a user-selected microrobot in the workspace was tracked in real-time, and the position information and real-time microscopic images were transmitted to the haptic interface side, where the above-described haptic interaction forces were calculated, and the haptic control command were sent back to the magnetic tweezer system.

Microrobots (10.6 μm average diameter) were mixed with deionized water to produce a 1% w/v solution. Environmental objects are non-magnetic glass microparticles (SLGMS-2.5 27-32 μm diameter, Cospheric LLC) with 1% w/v concentration. The experiment chamber is made from polydimethylsiloxane (PDMS) with a diameter of 3 mm. To decrease the surface friction of microrobots close to the substrate, a 20% w/v concentration of Tween 20 surfactant solution was introduced into the sample medium. 20% w/v NaCl solution was also used for Experiment 1 to mitigate gravitational effect of the microrobots.

5.1.6.1 Microrobot Manipulation with Haptic Feedback

The haptic operator was assisted by the haptic feedback to operate microrobots in 3D space. Since the 3D positions of a selected microrobot were synchronized with the haptic probe via artificial stiff spring and damper model, the motion of the selected microrobot was reflected by the operation of the haptic device and vice versa. Experimental demonstration is shown in Fig. 5-8, in which the microrobot navigated as controlled in 3D workspace to follow user-controlled trajectories with haptic feedback. Note that the motion of the microrobot on the *z*-axis followed the haptic control with delay due to the gravity and the viscous conditions of Tween 20 on the surface of the experimental chamber, the performance can be improved by setting a high gain parameter in magnetic tweezer system control part at the beginning to elevate the performance in high viscosity area of Tween 20 and then modifying the gain value back to normal after microrobot escapes from the bottom.

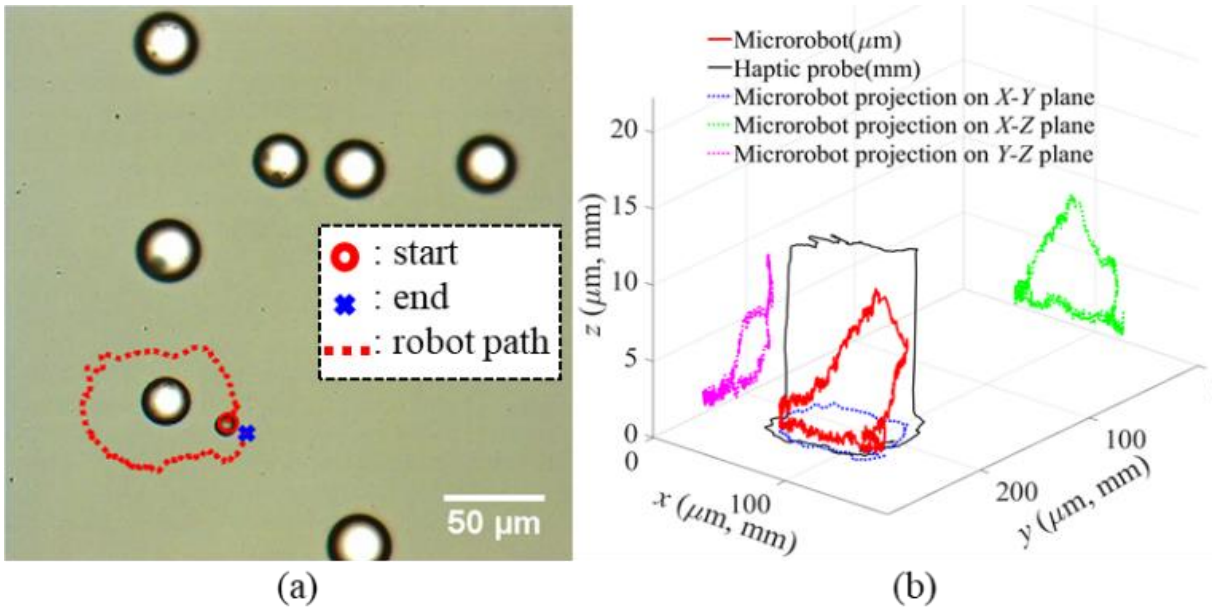

Fig. 5-8. Experiment 1: single microrobot manipulation with haptic feedback in 3D space. (a) Microrobot path by the haptic control for obstacle avoidance. (b) 3D motion of microrobot and haptic probe.

5.1.6.2 Dynamic Path Planning with the Path Following Force

When the path planning function was activated, the near-optimal path was displayed on the real-time interface, and path following force was applied to the haptic device. An effective path from the current haptic position to an estimated target was dynamically generated by reflecting the haptic user′s intended haptic operation. Fig. 5-9(a) shows the dynamic path generation and microrobot operation by the path following force. In this experiment, the user only held the haptic stylus lightly and let the microrobot reach the target through the dynamic path with the path following force. While the haptic device followed the path by itself, the user could still force the

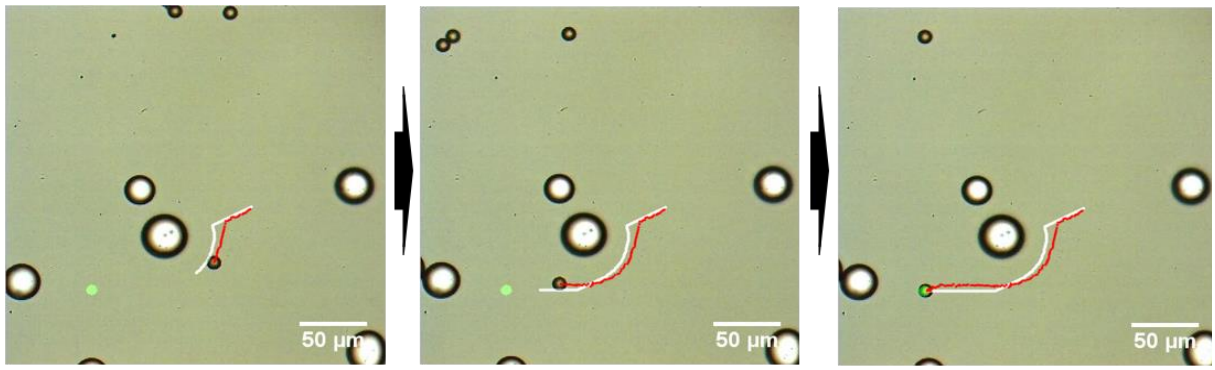

optimal path (white dot), microrobot (red dot), instant target (green dot)

(a) Experiment 2: dynamic motion planning and path following

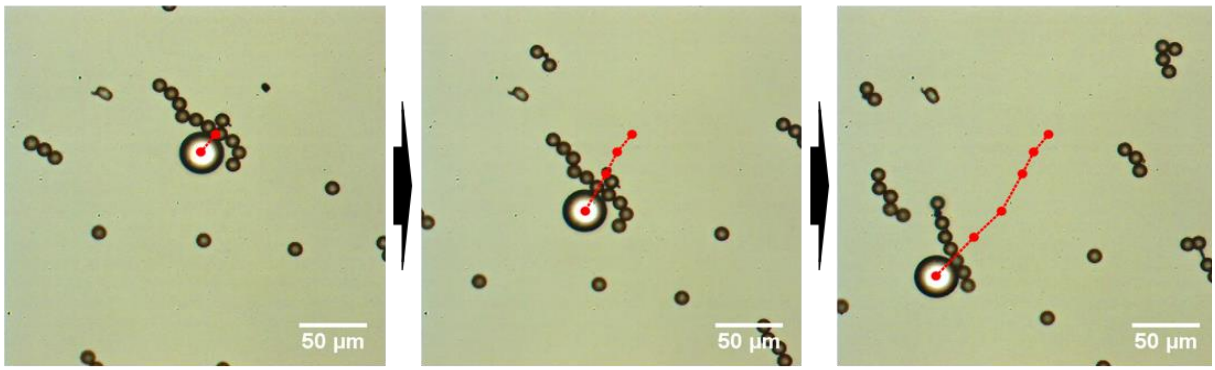

(b) Experiment 3: Micro object transportation with swarm control

Fig. 5-9. Path following and swarm experiments. (a) Experiment 2: dynamic motion generation and microrobot path by the haptic control with the path following force. (b) Experiment 3: micro-object transportation with swarm control of the microrobots.

haptic probe to move to another direction against the path following force to generate a new dynamic path.

5.1.6.3 Micro Object Transportation

The haptic-microrobot system could perform object transportation with haptic assistance in planar space. Since the magnetic force was applied to the global field, all microrobots were actuated by the same directional force. Swarm motion of the multiple microrobots aggregated them together to transport an object with the assistance of the haptic feedback. Fig. 5-9(b) shows the operation of the microrobot swarm for object transportation. The haptic device was virtually coupled to the center of mass of the microrobot swarm, while all swarm elements moved in the same direction by the haptic operation due to the global magnetic force field.

5.1.7 Conclusion

A magnetic force-driven microrobot manipulation system with haptic assistance is developed. A large volume data communication strategy is employed to achieve *in situ* real-time teleoperation between two systems in remote locations. The 3D haptic interaction between microrobot and the surrounding environment is implemented by combining ambient and contact forces. To improve the control and tracking accuracy, the effective, near-optimal path is dynamically generated based on the user′s haptic control tendency with the path following force. Eventually, a combination of the attraction force to the selected microrobot, force feedback by the environmental objects, path following force, and real-time visual feedback can improve the navigation performance and path tracking accuracy of the haptic operation for the microrobot controls. The developed system is verified with three potential applications in a practical

environment by locating two systems in remote locations, Washington, D.C. and Dallas, Texas, approximately 2,138 km apart.

5.2 Magnetically and Chemically Actuated Janus Particles for Micromanipulation

5.2.1 Introduction

Other than the microrobot actuation strategy with single power source using magnetic gradient field discussed previously, some other interesting methods can also be applied to bring diverse and flexible control ability into microrobot manipulation, such as chemically driven microrobots. Janus particles have gained significant interest due to the diverse configurations that can arise during their fabrication. Janus particles are fabricated to consist of two hemispheres: one side has a magnetic coating, such as cobalt, while the other side is coated with platinum. When the particles are suspended inside a hydrogen peroxide solution, the platinum will act as a catalyst and

$$2H_2O_2 \xrightarrow{\text{Pt}} 2H_2O + O_2 \tag{5-9}$$

decompose any surrounding hydrogen peroxide as described in Eq. (5-9); this causes a Janus particle to self-propel within the solution [120]. As the magnetic field in this work only acts as guidance for the particle alignment, we used a static magnetic field controller (electromagnetic coil system) that can generate a uniform magnetic field within its working space to make sure Janus particle will not be propelled by any magnetic gradient field using this magnetic field, the particles can be reoriented to create non-trivial trajectories. This has been discussed in several published works [120-123]. However, due to differences in magnetization, the magnetic orientation of a Janus particle may not coincide with the propulsion direction as shown in Fig. 5-10.While open loop control of Janus particles with randomly oriented magnetization direction was discussed in [121] and closed loop control of coincidental magnetization has been discussed in [122]; there has been no effort yet to develop or understand the effects of closed loop performance with randomly oriented particles. In this work collaborating with my colleague Dr.

Louis William Rogowski, we applied a closed loop controller to Janus particles that possessed misaligned magnetic orientations to the propulsion vector and compare their responses when performing simple trajectories. We examined particles with magnetization offset angles of only a few degrees all the way to a perfectly perpendicular offset of 90°.

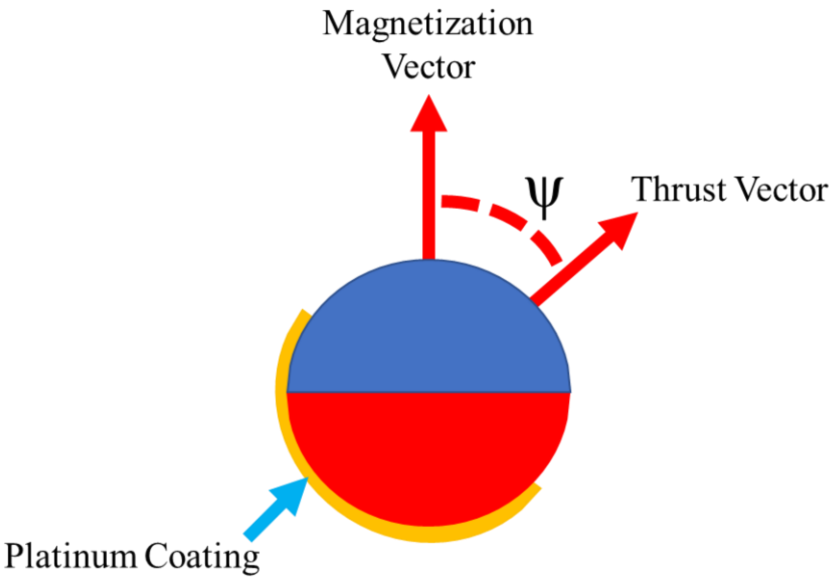

Fig. 5-10. 2D Schematic of a Janus particle consisting of a cobalt magnetic core and a platinum coating. ψ represents the offset angle between magnetization vector and thrust vector. The blue and red parts of the sphere represent the north and south poles, respectively.

5.2.2 Janus Particle Fabrication

Fig. 5-11(a) shows the Janus particle fabrication process from initial etching of the polystyrene beads to the multilayer coatings of both platinum (Pt) and cobalt (Co). A 0.5%(w/w) polystyrene bead water solution was prepared using polystyrene beads (Spherotech, 5 μm in diameter). The solution was then distributed onto a glass slide, whose surface was cleaned using UV-Ozone. The UV-Ozone treatment makes the glass surface hydrophilic, allowing the aqueous solution to spread out evenly along the slide's surface, making all beads form a monolayer with each bead touching side by side in a cluster through a self-assembled monolayer (SAM) effect

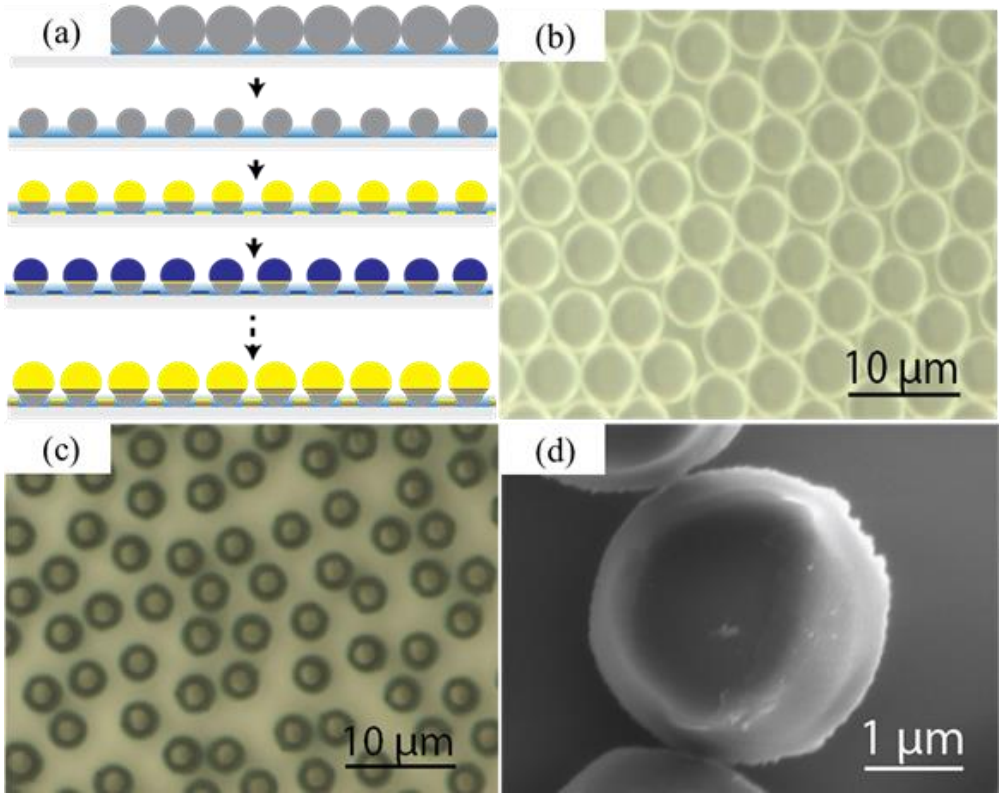

Fig. 5-11. (a) Multilayer Janus particle fabrication steps using Co/Pt layers. (b) Clustered polystyrene beads in a monolayer. (c) Separate multilayer Janus particles after RIE and Co/Pt capping. (d) SEM image of multilayer Janus particle.

when water solution is fully vaporized, which can be seen in Fig. 5-11(b). The beads were not individually distributed on the surface. As all beads were touching each other within the monolayer, reactive ion etching (RIE) was applied by etching the bead surface uniformly and the result is shown in Fig. 5-11(c). The final diameter of beads after etching is around 2.5 μm, which is about the half of the original size. To fabricate Janus particles that possessed both characteristics of magnetism and catalytic propulsion, both Co and Pt were coated on each half of the beads using an e-beam thermal evaporator (Temescal CV-8 e-beam evaporator). A glass substrate covered with microbeads was fixed on the coating plate in the evaporator facing downwards. A laser was used to evaporate the specific sample material for coating, which was then radially diffused onto the microbeads. The result was only half of the sphere was coated with the desired material. The

coating plate could be adjusted to have a different angle facing to the evaporated material for different coating combinations with different materials. A total of 5 layers were applied to the beads in the sequence of Pt 3 nm, Co 3 nm, Pt 3 nm, Co 3 nm, and Pt 3 nm to create stronger magnetism effects [124]. The Pt and Co were evaporated at a slow rate of 0.02 nm/sec to ensure the high-quality deposition. For our work, only half of the surface was coated with platinum, and the coated Co layers generated randomly distributed magnetic dipoles on the microbeads resulting in different offset angles with the thrust vector. The final Janus particles can be seen in Fig. 5-11(c). The attached beads were then detached from the glass surface by gently washing with water and brushing with a paint brush. The scanning electron microscopy (SEM) image of the coated Janus particles is shown in Fig. 5-11(d). The final size of the Janus particles is approximately 2.5-4 μm.

5.2.3 Experimental Setup

An approximate electromagnetic Helmholtz coil system was used to produce static magnetic fields to orient the Janus particles. The governing equations for the magnetic field for 2D control can be seen in Eq. (5-10), where θ is the orientation direction and B_s is the magnitude

$$\boldsymbol{B} = \begin{bmatrix} -B_S \cos(\theta) \\ B_s \sin(\theta) \\ 0 \end{bmatrix} \tag{5-10}$$

of the static magnetic field as shown in Fig. 5-12. For all tests discussed in this work, 5 Volts were applied to the magnetic coils, which resulted in a static field of 8 mT within the working space. This magnetic field was only used to orient the particles and did not create any magnetic field gradients.

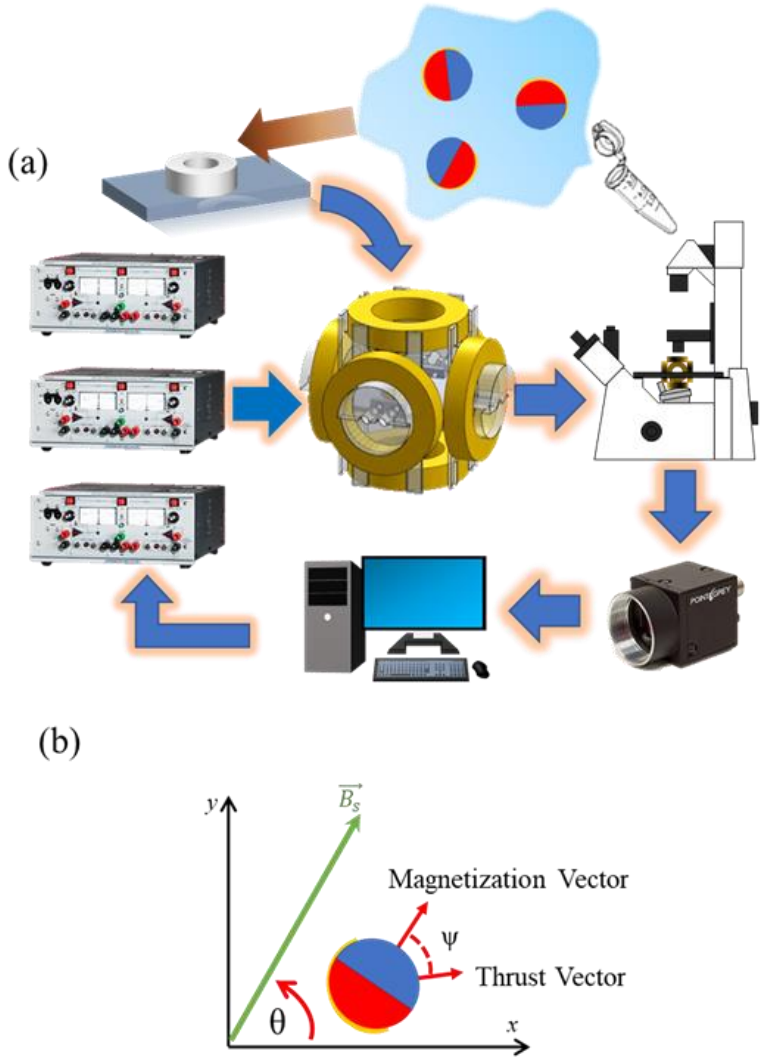

Fig. 5-12. (a) Overview of experimental set up including Helmholtz coil system, sample chamber with Janus particles. (b) Illustration of how Janus particle naturally orient its magnetization vector to the static magnetic field vector.

Janus particles of 4 μm diameter were inserted into a Polydimethylsiloxane (PDMS) chamber approximately 2 mm in diameter and 1 mm thick, which was bonded to a glass slide. A 5 μL solution of concentrated Janus particles was placed into the chamber and then mixed with a diluted 10% H_2O_2 solution (Sigma Aldrich). A cover slide was then applied to enclose the sample chamber to minimize external vaporization. The chamber was then placed in the center of the approximate Helmholtz coil system. Using three programmable power supplies (KEPCO, BOP

36-6M) interfaced with two digital acquisition control boards (BNC-2110), and a customized LabVIEW program, the particles could be manipulated based on the formulas presented in Eq. (5-10). All experiment videos were captured and processed using a CMOS camera at 30 frames per second (fps). The experimental setup can be seen in Fig. 5-12(a) while the effect θ has on the static magnetic field can be seen in Fig. 5-12(b). Due to the decomposition of H_2O_2, the chamber would fill with bubbles and interfere with image capturing over time. All samples were used until bubbles made it impossible to clearly view Janus particles or no usable Janus Particles could be located.

5.2.4 Kinematics Modeling

To model the kinematics of Janus particles, we must first consider a Janus particle in a 2D plane with an offset angle ψ, measured counterclockwise, from its magnetic moment axis to its velocity vector. Given an external magnetic field with the orientation angle *θ(t)*, the Janus particle aligns to its magnetic moment with the external field, and the simplified kinematics at time *t* is described by Eq. (5-11), where $x(t) \in \mathbb{R}^{2x1}$ denotes the position, and $\mathbf{v}(t) \in \mathbb{R}^{2x1}$ as seen in Eq. (5-12) denotes the velocity, and *v* represents the magnitude.

$$\mathbf{x}(t + \Delta t) = \mathbf{x}(t) + \mathbf{v}(t)\Delta t \tag{5-11}$$

$$\mathbf{v}(t) = v \begin{bmatrix} \cos(\theta(t) + \psi) \\ \sin(\theta(t) + \psi) \end{bmatrix} \tag{5-12}$$

Note the offset angle ψ is constant for each Janus particle, but this angle can be different between individual particles. To identify the velocity magnitude *v* and the offset angle ψ of a Janus particle, three experiments were performed with more than 10000 data points acquired from trajectory information extracted from image processing. Fig. 5-13 shows the histograms of velocity

magnitude distribution and offset angle distributions. Based on their statistics, the average velocity magnitude is approximated as 0.72 μm/s with a standard deviation of 0.24 μm/s and the average offset angle was identified as 49.45° with a standard deviation of 21.13°.

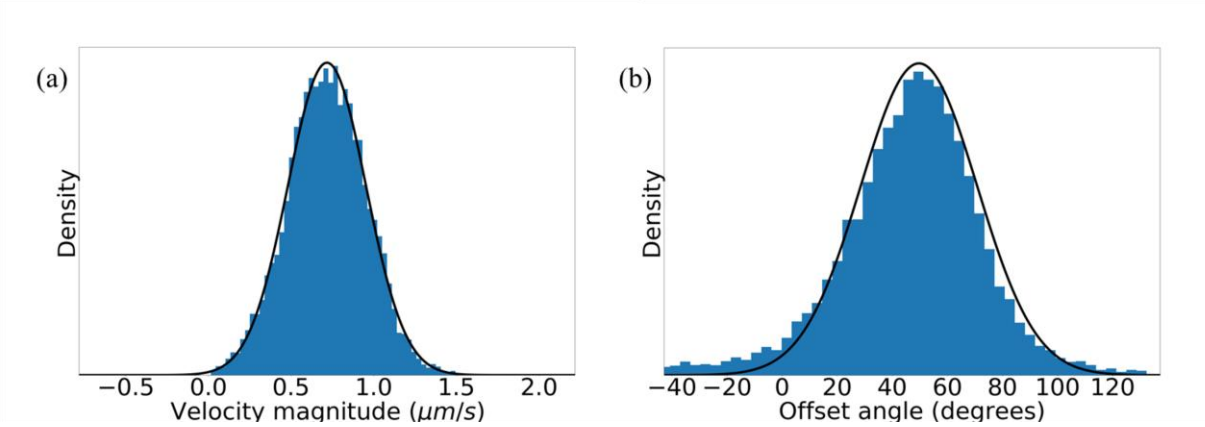

Fig. 5-13. (a) Velocity magnitude distribution of sampled Janus particles. (b) Offset angle distribution of sampled Janus Particles.

To validate the kinematics model, the simulation results were compared with experiment data, Fig. 5-14 demonstrates a particle with same offset angle and similar velocity as the one predicted by the statistical model, the controlled particle closely matched the predictions given in the statistical analysis. By estimating this offset angle, Janus particle motion can be predicted with a high degree of accuracy.

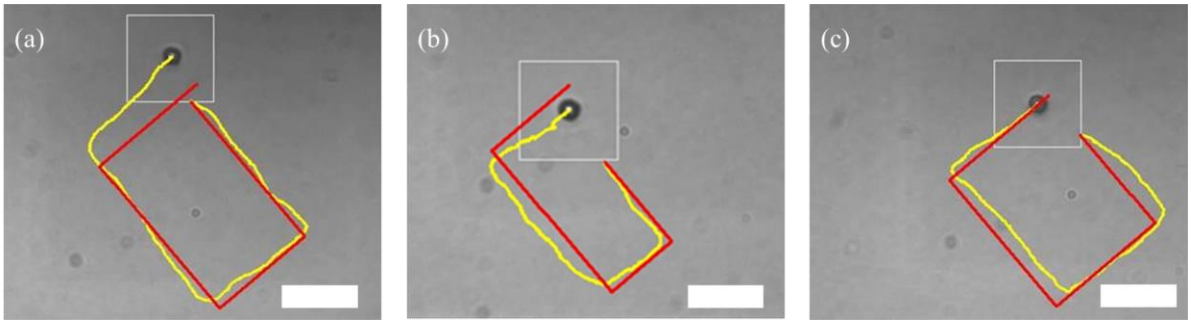

Fig. 5-14. (a-c) The simulated trajectories of the particle are illustrated by the red line while the actual path of the particle is shown in the yellow line. Scale bars are 10 μm.

5.2.5 Feedback Control Dynamics

The feedback control used in this work is identical to the one utilized to maneuver achiral microrobots in BAST lab's previous research [36, 51], however, in this case, it is significantly simplified to only care about the change in θ. This simplification was performed since the Janus particles would move with a quasi-constant velocity when exposed to H_2O_2 and did not rely on rotational dynamics to move through the fluid medium. φ is the angle for vector from Janus particle location to target location. Janus particle location information was extracted from images through real-time image processing. The vector between the desired position and current position is obtained and thus the angle φ is known. The time derivative of θ is shown in Eq. (5-13), where k

$$\dot{\theta} = k\alpha \tag{5-13}$$

$$\alpha = \varphi - \theta \tag{5-14}$$

is a gain parameter. α in Eq. (5-14) is the difference between angle φ and the magnetic heading angle θ of the Janus particle. The proportional controller keeps minimizing the angle difference α to update the magnetic field heading angle θ for correcting the trajectory. Throughout our experiments, k was set to a constant value of 5.

5.2.6 Experiment Results

Two experiments were conducted to demonstrate the maneuverability of Janus particles. The first one will discuss homogeneous Janus particles, where the magnetization vector was closely aligned to the propulsion vector, the second will discuss heterogeneous particles where a larger offset angle was present.

5.2.6.1 Homogeneous Particles

Homogeneous particles performed exceptionally well when exposed to static magnetic fields and their motion was highly consistent with the magnetic field direction. In Fig. 5-15, we

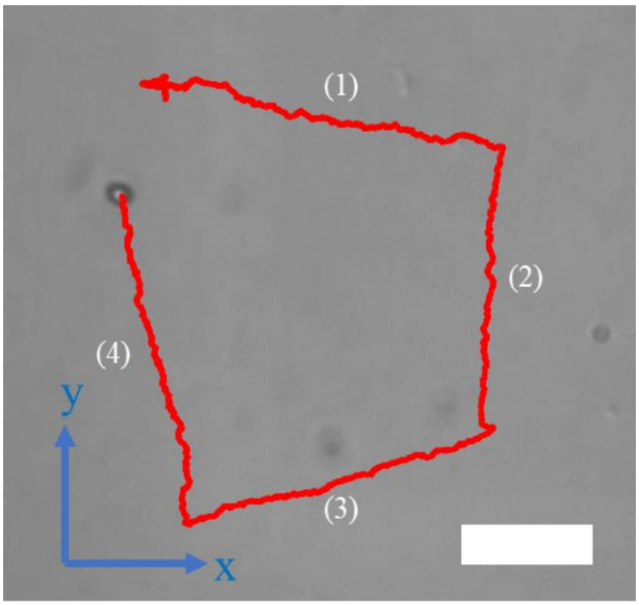

Fig. 5-15. Trajectory of a heterogeneous particle with a small offset angle. The static magnetic fields applied are oriented to 0°, 90°, 180°, and 270° at points (1-4) respectively. The particle could reliably follow the static magnetic field direction. Scale bar is 10μm.

demonstrate a particle moving in a box pattern when exposed to static magnetic fields applied at the angles 0°, 90°, 180°, and 270° using open loop control. While there is a slight offset angle present, the particle could still move in the intended direction with only small variation. When a similar particle was controlled using the discussed feedback controller, it displayed high accuracy, especially when asked to perform arbitrary trajectories. An example of these trajectories can be seen in Fig. 5-16, where the particle could easily navigate towards the intended targets without issue. When examined for trajectory repeatability, the particle was directed to perform a box pattern with target points positioned 16 μm apart. An example of this trajectory can be seen in Fig. 5-17(a). While the example does not perfectly follow the desired direction, it does indeed reach

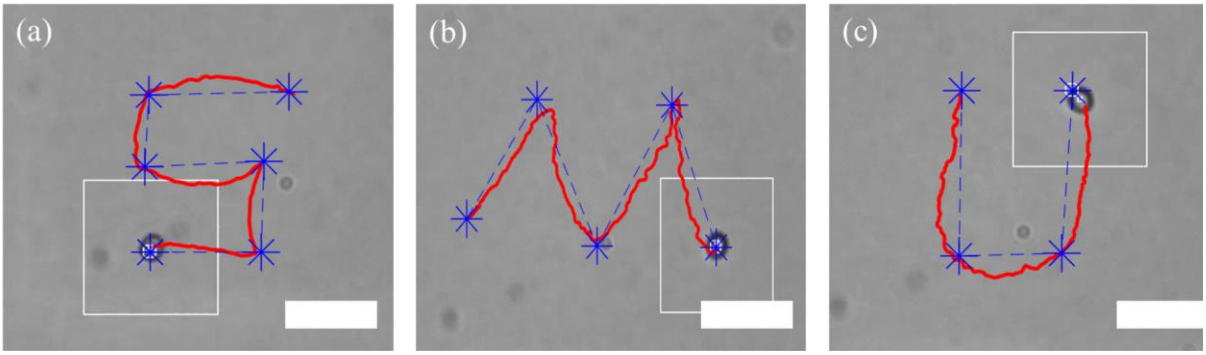

Fig. 5-16. Closed loop trajectories of a Janus particle with small offset angle. The blue dots represent the target points, dashed blue lines show the connection between each pair of target points the dashed lines represent the desired trajectory, and the red sold line shows the actual trajectory. The white box is used to track the particle. The scale bars are 10 µm.

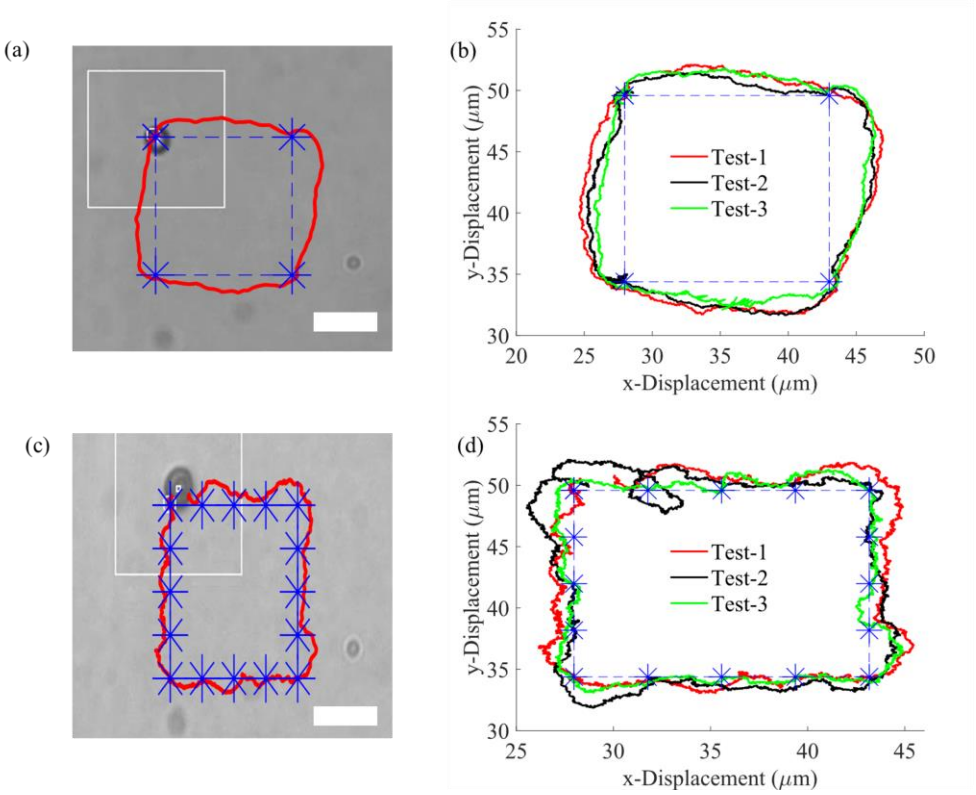

Fig. 5-17. (a) Closed loop control of Janus particle to form a box shape pattern. The blue dashed line represents the desired path and blue stars represent target points. The solid red line indicates the actual path followed by the particle. The particle started at the top left point and proceeded counterclockwise to each target point. (b) Three independent trajectories of the Janus particle under the same control inputs and similar starting conditions. (c) Trajectory of the same size as (a) but with 16 target points. (d) Trajectories of the Janus particle navigating the box outlined in (c). Scale bars in (a) and (c) are 10 µm.

each of the target destinations without significant issue. Three independent tests were performed, and each test produced nearly identical trajectory results and can be seen in Fig. 5-17(b); any variations were caused by slight differences in initial starting position and tracking failures using real time image processing. When these trajectories were increased from 4 points to 16 points, with a 4 μm gap between each point, the particle trajectory accuracy was greatly improved as can be seen in Fig. 5-17(c). However, as can be seen in Fig. 5-17(d), the results were not without their issues. Test-2 in Fig. 5-17(d) was particularly deviant, where the Janus particle often strayed far from the desired trajectory and in one case completely circling the target point. This can be attributed to error in the timing associated with incrementing the target positions after the Janus particle finished approaching the previous target. In the other two cases though, the particle was close enough in proximity to the desired path to be considered acceptable. Similar results were obtainable for other Janus particles with low offset angles.

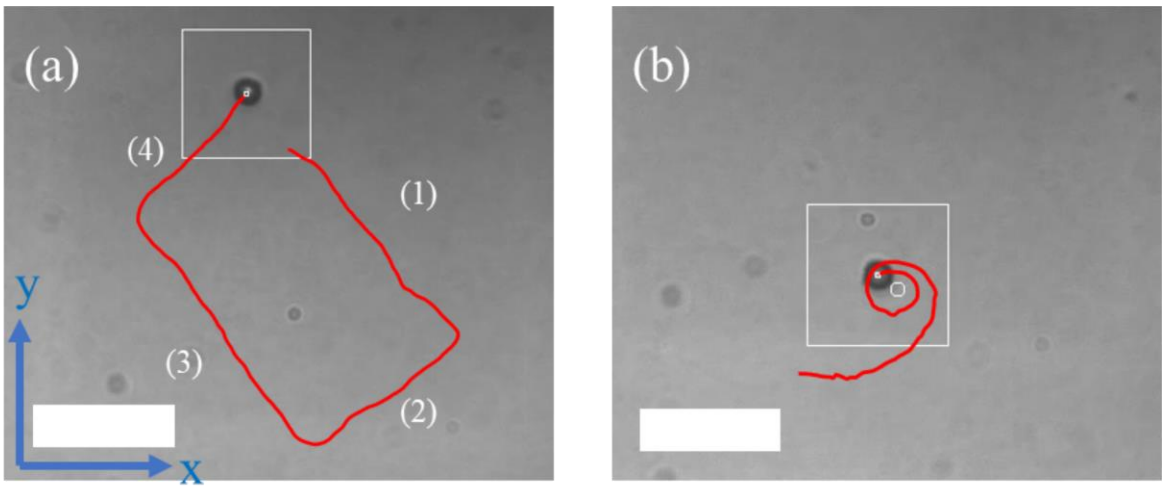

Fig. 5-18. (a) Arbitrary closed loop trajectories of a Janus particle with a large offset angle of approximately 45°. The static magnetic fields applied are oriented to 0°, 90°, 180°, and 270° at points (1-4) respectively. (b) Closed loop control of the particle. The white box is used to track the particle. The scale bars are 10 μm.

5.2.6.2 Heterogeneous Particles

A heterogeneous particle with an approximate offset angle of 45° was pre-identified through open loop control as illustrated in 5.2.4. Using open loop control, a static magnetic field direction of 0°, 90°,180°, and 270° was applied. The resulting trajectory can be seen in Fig. 5-18(a). Since the trajectory produced was tilted, ≈45º offset angle was estimated to have caused the deviation. For Fig. 5-18(b), the closed loop control algorithm was applied to a single point and a spiral towards the target point was obtained. While the offset angle prevents the Janus particle

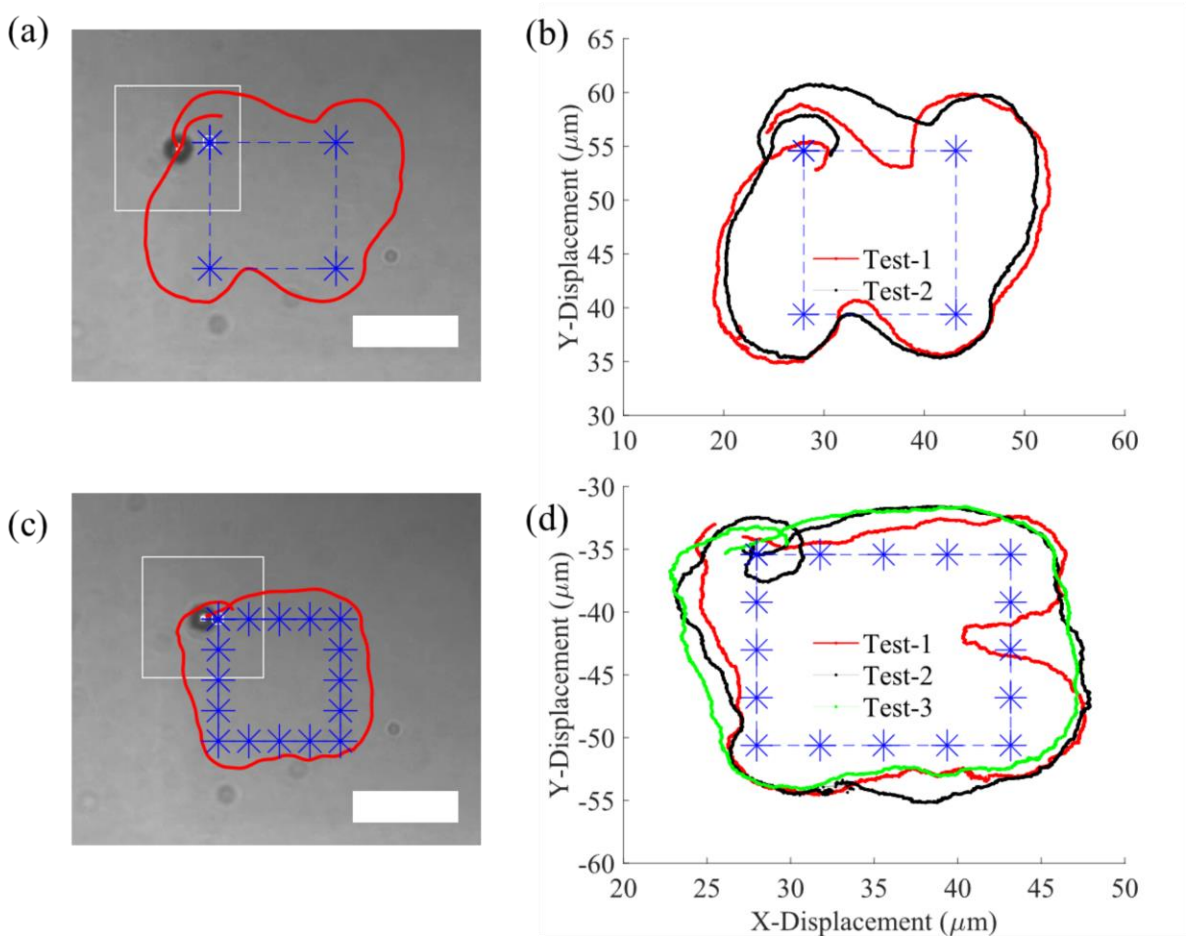

Fig. 5-19. (a) Closed loop control of a Janus particle with a 45° offset forming a box shape pattern. Blue dashed line represents desired path and blue stars represent target points. Solid red line indicates the actual path of the particle. The particle started at the top left point and proceeded counterclockwise to each target point. (b) Two independent trajectories of the Janus Particle under same control inputs and similar starting conditions. (c) A box trajectory of the same size as (a) but with 16 points bounding the box. (d) Trajectories of the Janus particle navigating the box outlined in (c). Scale bar in (a) is 10 μm.

from directly reaching the target; given enough time, the particle's spiral will decay and allow for proximity to the target. While this is not optimal, it can still create interesting effects when directed to perform the same box trajectories carried out using the homogeneous particle. These trajectories can be seen in Fig. 5-19(a-b) for four target point locations and Fig. 5-19(c-d) for 16 target points. The points had to be iterated fast enough to prevent the particle from spiraling around any given target point. Interestingly, while the four-point box in Fig. 5-19(a) was inaccurate, the particle performed very similar trajectories between the independent trials in Fig. 5-19(b). Going from a four-point box to a 16-point box greatly improved the trajectory accuracy of the particle, but the offset angle made directly reaching the targets, without spiraling unlikely. Only one noticeable discrepancy happened in Test-1 as shown in Fig. 5-19(d), where the particle overshot the target and went inside the box. The particle in 16 points box trajectories had improved accuracy in

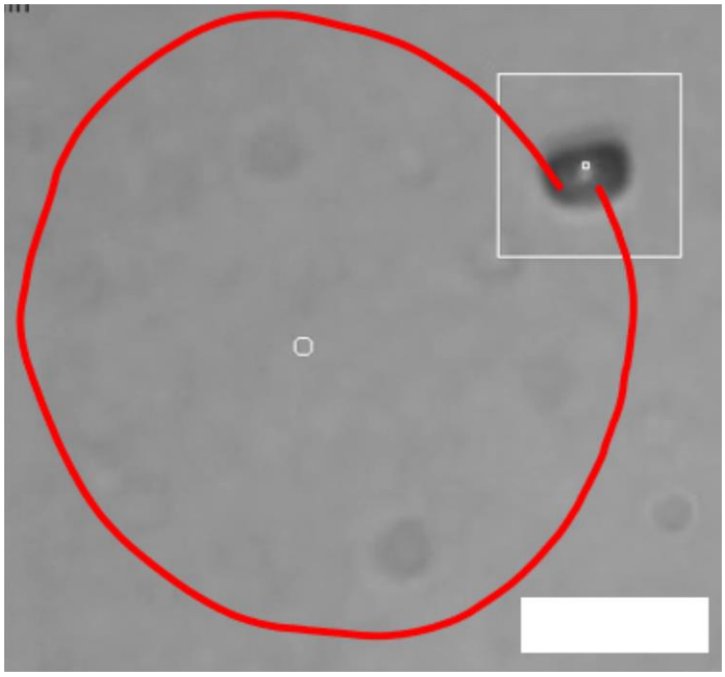

Fig. 5-20**.** A Janus particle with a 90° magnetization offset to the thrust vector. This particle will never reach the target point indicated by the white circle, and instead will orbit almost perfectly around it. The scale bar is 10 μm and the white box tracks the particle.

following the intended trajectory between each pair of way points comparing to that in four point trajectories.

In another experiment, a particle was identified with a large offset angle of approximately 90° in relation to the thrust vector as shown in Fig. 5-20. Under closed loop control, the particle almost perfectly orbited around the white target point and never approached.

5.2.7 Conclusion

In conclusion, we demonstrated that homogeneous and heterogeneous Janus particles can be manipulated using open loop and closed loop control to perform specific trajectories. For the feedback control, the magnetization angle played a huge impact on how well the Janus particles could reach their target destinations. If the magnetization angle is close to the propulsion vector, the particle could reach the intended target with little hinderance. However, if the offset angle is significant, the particle would take considerably longer effort to reach the target and proceed towards it in a spiral motion. When the offset angle is 90°, the particle will almost perfectly orbit the intended target position. When the particles were directed to perform a box pattern, heterogeneous particles could perform the intended trajectories, with improving accuracy as the number of points bounding the box trajectory increased. Of course, in both Janus particles with large and small offset angles, there were abnormal cases where issues in tracking or variations in starting conditions caused the particles to behave unexpectedly. The progress presented in this section is at the very early stage of the project, there are several things that should be addressed to improve the performance of the controller. In future work, we plan to implement a feedback controller which can retroactively account for the magnetization angle difference and perform 3D feedback control of heterogeneous Janus particles, the offset angle ψ can also be taken into account in Eq. (5-14) to correct the controller for the offset and thus improve the motion control

performance. The user can estimate this offset angle in advance to obtain this offset angle for feedback control. Alternatively, an adaptive controller that can adjust the motion deviation gradually to correct the offset angle is also viable.

CHAPTER 6 CONCLUSIONS

In conclusion, this thesis illustrated the design, development, force mechanism, implementation, and performance evaluation of a novel 3D magnetic tweezer system. This system is the first in its kind to utilize 3D printing for fabrication of many of the components with new design to make sample placement and retraction more convenient. The generation ability of magnetic gradient field was validated with simulation and experimental data. Moreover, the performance was also demonstrated using the studied force modeling in terms of 3D mobility.

At the early development stage, several experiments including directional control for 2D motion were conducted and the feasibility of microrobot manipulation under multiple direction magnetic forces was demonstrated in Newtonian and non-Newtonian fluid environments with open loop control. The velocity and current relationship was also obtained for a single bead microrobot under the magnetic force induced in the same location by single magnetic pole functionalization. The velocity of microrobots could be changed by adjusting the input current. For microrobots in the central area of the working space, the force superposition method is a very effective approximation, however, this estimation becomes invalid if microrobots approach too close to any of those magnetic poles as magnetic gradient field is not linearly distributed at the proximity of magnetic pole tip, which leads to a large difference in the magnetic field gradient strength around that area. Thus, we limited our working space in a small volume in the center of the hexagonal shape, while it still outperforms all other designs in terms of size of the working volume as well as on magnetic field generation ability aspect. The difference between number of magnetic microparticles in microrobots also causes different velocities as those that assembled with more

magnetic microparticles had a relatively stronger magnetic dipole moment. After the relationship between microrobot area size and *z*-depth was established, post processing of trajectory for single bead microrobot moving in 3D under arbitrary magnetic force was achieved, which allowed the more complicated 3D motion control for our system.

On software level, the modeling and experimental application of closed loop control algorithm for 3D micromanipulation was then developed. Experiments for both 2D and 3D control were conducted and analyzed to illustrate the flexible controllability. 3D trajectories of microrobot motion were generated by deploying the area size relationship mentioned above for *z*-motion tracking in real-time experiment. The force generation ability was shown through analysis of microrobot velocity using the equilibrium between magnetic force and viscous force from Stoke's law.

Experiment, and analysis for closed loop 2D/3D swarm control of microrobots were also conducted. Experiment conducted with our system is the first to extensively investigate microrobot performance with 2D/3D motion control under open loop and closed loop control strategies for different tasks, such as achieving 3D complex trajectory, obstacle avoidance in non-Newtonian fluid environment, and moving against microflow. The high magnetic force generation ability also enables our system to achieve swarm control of microrobots in 3D, which works from other groups cannot achieve. Demonstrations from our experiments show that microrobots with similar properties can act homogeneously under a uniform input to reliably perform complex operations such as arbitrary 3D motion even with the presence of microflow. The results provide guidance for future development of control systems for microrobotics and will advance toward practically controllable magnetically actuated microrobots in *in vivo* applications such as drug delivery and cell therapy applications.

Haptics integration with a magnetic tweezer system was later investigated. A large volume of data communication between long distance in real-time was achieved. During operation, the effective and near-optimal path was dynamically generated based on the user's haptic control input, while the combination of the attraction force from the selected microrobot, force feedback given by the environmental objects, and path following force enabled the haptic operation to have high accuracy microrobot control. Real-time visual feedback can also improve the navigation performance and path tracking accuracy. Three experiments representing potential applications were conducted, in which two systems were locate in Washington, D.C. and Dallas, Texas (approximately 2,138 km apart), respectively. The demonstration of this remote control of the microrobot application with haptic interaction is crucial to extending the utility of microrobotics for future remote therapy and surgery scenarios.

The collaborative work on manipulation of homogeneous and heterogeneous Janus microparticles using open loop and closed loop control was conducted to perform specific trajectories. The effect of magnetization angle on Janus particle motion was investigated. This work will be developed to have a feedback controller with the adaption of the magnetization angle difference and will perform 3D feedback control.

CHAPTER 7 FUTURE WORK

While the magnetic tweezer system illustrated in this thesis can perform as a powerful scientific tool for microrobot applications, the next essential step is to test its motion performance in an *in vivo* environment, such as cell penetration experiments to manipulate microrobots within complex cell environment for cell therapy, and *in vivo* swarm control of microrobots towards target location with specific drug payload onboard for drug delivery. These tasks lead to another challenging but necessary objectives: non-vision-based image acquisition, as the ordinary imaging technique will not be able to extract location and state information of microrobot through the skin or vessel membrane. Non-vision-based image acquisition is an essential part to have this work developed for *in vivo* environments. It may not be limited to only in the scope of magnetic tweezer system specifically, but it is necessary for the broader development of microrobotics for *in vivo* applications, from which magnetic tweezer system will also benefit. Possible ways for achieving this objective include, but are not limited to, constructing a magnetic field sensor array to cover overall workspace in 3D for microrobot detection, and microrobot fabrication with preprocessing of fluorescence for real-time detection under fluorescent microscopy. Also, the workspace and power output should be extended if the subject involved in animal experiment is relatively large or specific experiments require high power for stronger magnetic force.

For microrobot fabrication, more robust and reliable methods rather than random mixing is desired to produce qualified microrobots in bulk. One possible way is through microfabrication with several layers of templated patterns, which will enable the bulk production of microrobot with diverse shapes and functions that can be customized during preparation stage. Also, bio-

compatible or bio-degradable material is in demand for implementing microrobots into living experiment samples to fulfill safety requirements. Currently, most microrobots are fabricated with magnetic metal material like iron alloy, cobalt, and nickel, which cannot be easily discharged from animal body or effectively degraded inside it. Thus, it is crucial to conduct interdisciplinary collaboration to utilize novel material that meets the safety requirement to further push the project for practical application.

The haptics integration with the magnetic tweezer system can also be further improved for fully 3D operation with 3D path planning and force feedback. Stability analysis can be conducted using the passivity of the bilateral system with consideration of the practical time delay, which helps the system to monitor and predict any delay during operation and make corresponding compensation for it. This is necessary for long distance teleoperation architecture. On the software level, dynamic path planning can also be improved by learning the arbitrary experienced human user′s haptic operation with deep learning approaches such as long-short-term-memory (LSTM). This approach will help improve tasks such as training course for surgery, remote surgery, and error prevention feature to aid user on forming correct operation procedures to avoid potential damage to patient or other subjects. New users can be guided through a series of training courses by a highly skilled expert to get familiar with surgery procedures, which can save significant time on training and build up standard regulations for specific surgeries. Also, though communication delay in our experiment is not observed, it is still necessary to develop the system in a manner that it can anticipate a doctor’s movement and respond to connection delay or offline with proper actions during an actual surgery process. On the other hand, doctors can still be guided by the system for each procedure and can be corrected if mistake or dangerous move is made.

REFERENCES

[1] R. P. Feynman, "Plenty of Room at the Bottom," in *APS Annual Meeting*, 1959.

[2] D. Jang, J. Jeong, H. Song, and S. K. Chung, "Targeted drug delivery technology using untethered microrobots: A review," *Journal of Micromechanics and Microengineering*, vol. 29, no. 5, p. 053002, 2019.

[3] S. Palagi and P. Fischer, "Bioinspired microrobots," *Nature Reviews Materials*, vol. 3, no. 6, pp. 113-124, 2018.

[4] S. Yu and B. J. Nelson, "Microrobotic cell injection," in *Proceedings 2001 ICRA. IEEE International Conference on Robotics and Automation (Cat. No. 01CH37164)*, 2001, vol. 1, pp. 620-625.

[5] J. Jeong, D. Jang, D. Kim, D. Lee, and S. K. Chung, "Acoustic bubble-based drug manipulation: Carrying, releasing and penetrating for targeted drug delivery using an electromagnetically actuated microrobot," *Sensors and Actuators A: Physical*, vol. 306, p. 111973, 2020.

[6] C. K. Schmidt, M. Medina-Sánchez, R. J. Edmondson, and O. G. Schmidt, "Engineering microrobots for targeted cancer therapies from a medical perspective," *Nature Communications*, vol. 11, no. 1, pp. 1-18, 2020.

[7] X. Liu, K. Kim, Y. Zhang, and Y. Sun, "Nanonewton force sensing and control in microrobotic cell manipulation," *The International Journal of Robotics Research*, vol. 28, no. 8, pp. 1065-1076, 2009.

[8] H. Lu, Y. Yang, X. Lin, P. Shi, and Y. Shen, "Low‐Invasive Cell Injection based on Rotational Microrobot," *Advanced Biosystems*, vol. 3, no. 7, p. 1800274, 2019.

[9] F. Ongaro, D. Niehoff, S. Mohanty, and S. Misra, "A contactless and biocompatible approach for 3d active microrobotic targeted drug delivery," *Micromachines*, vol. 10, no. 8, p. 504, 2019.

[10] D.-i. Kim, H. Lee, S.-h. Kwon, H. Choi, and S. Park, "Magnetic nano-particles retrievable biodegradable hydrogel microrobot," *Sensors and Actuators B: Chemical*, vol. 289, pp. 65-77, 2019.

[11] K. T. Nguyen, G. Go, Z. Jin, B. A. Darmawan, A. Yoo, S. Kim, M. Nan, S. B. Lee, B. Kang, and C. S. Kim, "A Magnetically Guided Self‐Rolled Microrobot for Targeted Drug Delivery, Real‐Time X‐Ray Imaging, and Microrobot Retrieval," *Advanced Healthcare Materials*, vol. 10, no. 6, p. 2001681, 2021.

[12] S. Fusco, F. Ullrich, J. Pokki, G. Chatzipirpiridis, B. Özkale, K. M. Sivaraman, O. Ergeneman, S. Pane, and B. J. Nelson, "Microrobots: a new era in ocular drug delivery," *Expert Opinion on Drug Delivery*, vol. 11, no. 11, pp. 1815-1826, 2014.

[13] K. Villa, L. Krejčová, F. Novotný, Z. Heger, Z. Sofer, and M. Pumera, "Cooperative multifunctional self‐propelled paramagnetic microrobots with chemical handles for cell manipulation and drug delivery," *Advanced Functional Materials*, vol. 28, no. 43, p. 1804343, 2018.

[14] K. T. Nguyen, M. C. Hoang, E. Choi, B. Kang, J.-O. Park, and C.-S. Kim, "Medical microrobot—A drug delivery capsule endoscope with active locomotion and drug release mechanism: Proof of concept," *International Journal of Control, Automation and Systems*, vol. 18, no. 1, pp. 65-75, 2020.

[15] S. Fusco, H.-W. Huang, K. E. Peyer, C. Peters, M. Häberli, A. Ulbers, A. Spyrogianni, E. Pellicer, J. Sort, and S. E. Pratsinis, "Shape-switching microrobots for medical applications: The influence of shape in drug delivery and locomotion," *ACS Applied Materials & Interfaces,* vol. 7, no. 12, pp. 6803-6811, 2015.

[16] S. Lee, J. y. Kim, J. Kim, A. K. Hoshiar, J. Park, S. Lee, J. Kim, S. Pané, B. J. Nelson, and H. Choi, "A Needle‐Type Microrobot for Targeted Drug Delivery by Affixing to a Microtissue," *Advanced Healthcare Materials,* vol. 9, no. 7, p. 1901697, 2020.

[17] A. Vikram Singh and M. Sitti, "Targeted drug delivery and imaging using mobile milli/microrobots: A promising future towards theranostic pharmaceutical design," *Current Pharmaceutical Design,* vol. 22, no. 11, pp. 1418-1428, 2016.

[18] H. Li, G. Go, S. Y. Ko, J.-O. Park, and S. Park, "Magnetic actuated pH-responsive hydrogel-based soft micro-robot for targeted drug delivery," *Smart Materials and Structures,* vol. 25, no. 2, p. 027001, 2016.

[19] H. Li, J. Tan, and M. Zhang, "Dynamics modeling and analysis of a swimming microrobot for controlled drug delivery," *IEEE Transactions on Automation Science and Engineering,* vol. 6, no. 2, pp. 220-227, 2008.

[20] Y. Bailly, Y. Amirat, and G. Fried, "Modeling and control of a continuum style microrobot for endovascular surgery," *IEEE Transactions on Robotics,* vol. 27, no. 5, pp. 1024-1030, 2011.

[21] Y. Zhou, Y. Quan, K. Yoshinaka, and K. Ikeuchi, "A new medical microrobot for minimal invasive surgery," *Proceedings of the Institution of Mechanical Engineers, Part H: Journal of Engineering in Medicine,* vol. 215, no. 2, pp. 215-220, 2001.

[22] B. J. Nelson, I. K. Kaliakatsos, and J. J. Abbott, "Microrobots for minimally invasive medicine," *Annual Review of Biomedical Engineering,* vol. 12, pp. 55-85, 2010.

[23] F. Ullrich, C. Bergeles, J. Pokki, O. Ergeneman, S. Erni, G. Chatzipirpiridis, S. Pané, C. Framme, and B. J. Nelson, "Mobility experiments with microrobots for minimally invasive intraocular surgery," *Investigative Ophthalmology & Visual Science,* vol. 54, no. 4, pp. 2853-2863, 2013.

[24] P. A. York, R. Peña, D. Kent, and R. J. Wood, "Microrobotic laser steering for minimally invasive surgery," *Science Robotics,* vol. 6, no. 50, 2021.

[25] U. Kei Cheang, K. Lee, A. A. Julius, and M. J. Kim, "Multiple-robot drug delivery strategy through coordinated teams of microswimmers," *Applied Physics Letters,* vol. 105, no. 8, p. 083705, 2014.

[26] B. G. Hosu, K. Jakab, P. Bánki, F. I. Tóth, and G. Forgacs, "Magnetic tweezers for intracellular applications," *Review of Scientific Instruments,* vol. 74, no. 9, pp. 4158-4163, 2003.

[27] C. Haber and D. Wirtz, "Magnetic tweezers for DNA micromanipulation," *Review of Scientific instruments,* vol. 71, no. 12, pp. 4561-4570, 2000.

[28] D. Kilinc and G. U. Lee, "Advances in magnetic tweezers for single molecule and cell biophysics," *Integrative Biology,* vol. 6, no. 1, pp. 27-34, 2014.

[29] S. Fusco, G. Chatzipirpiridis, K. M. Sivaraman, O. Ergeneman, B. J. Nelson, and S. Pané, "Chitosan electrodeposition for microrobotic drug delivery," *Advanced Healthcare Materials,* vol. 2, no. 7, pp. 1037-1044, 2013.

[30] E. B. Steager, M. S. Sakar, D. H. Kim, V. Kumar, G. J. Pappas, and M. J. Kim, "Electrokinetic and optical control of bacterial microrobots," *Journal of Micromechanics and Microengineering,* vol. 21, no. 3, p. 035001, 2011.

[31] A. Ferreira, J. Agnus, N. Chaillet, and J.-M. Breguet, "A smart microrobot on chip: Design, identification, and control," *IEEE/ASME Transactions on Mechatronics,* vol. 9, no. 3, pp. 508-519, 2004.

[32] G. Dogangil, O. Ergeneman, J. J. Abbott, S. Pané, H. Hall, S. Muntwyler, and B. J. Nelson, "Toward targeted retinal drug delivery with wireless magnetic microrobots," in *2008 IEEE/RSJ International Conference on Intelligent Robots and Systems*, 2008, pp. 1921-1926.

[33] A. R. Bausch, W. Möller, and E. Sackmann, "Measurement of local viscoelasticity and forces in living cells by magnetic tweezers," *Biophysical Journal,* vol. 76, no. 1, pp. 573-579, 1999.

[34] K. C. Neuman and A. Nagy, "Single-molecule force spectroscopy: optical tweezers, magnetic tweezers and atomic force microscopy," *Nature Methods,* vol. 5, no. 6, pp. 491-505, 2008.

[35] X. Wang, M. Luo, C. Ho, Z. Zhang, Q. Zhao, C. Dai, and Y. Sun, "Robotic intracellular manipulation: 3D navigation and measurement inside a single cell," in *2018 IEEE International Conference on Robotics and Automation (ICRA)*, 2018, pp. 2716-2721.

[36] U. K. Cheang, M. Dejan, J. Choi, and M. Kim, "Towards model-based control of achiral microswimmers," in *ASME 2014 Dynamic Systems and Control Conference*, 2014.

[37] U. K. Cheang, F. Meshkati, D. Kim, M. J. Kim, and H. C. Fu, "Minimal geometric requirements for micropropulsion via magnetic rotation," *Physical Review E,* vol. 90, no. 3, p. 033007, 2014.

[38] D. Matsuura, H. Aoki, and Y. Takeda, "Development of a 3D-magnetic tweezer system having magnetic pole positioning mechanism," in *2016 IEEE International Conference on Robotics and Automation (ICRA)*, 2016, pp. 1745-1750.

[39] X. Zhang, H. Kim, and M. J. Kim, "Design, implementation, and analysis of a 3-D magnetic tweezer system with high magnetic field gradient," *IEEE Transactions on Instrumentation and Measurement,* vol. 68, no. 3, pp. 680-687, 2018.

[40] X. Zhang, H. Kim, L. W. Rogowski, S. Sheckman, and M. J. Kim, "Novel 3D magnetic tweezer system for microswimmer manipulations," in *2017 14th International Conference on Ubiquitous Robots and Ambient Intelligence (URAI)*, 2017, pp. 382-387.

[41] X. Zhang, L. W. Rogowski, and M. J. Kim, "Closed-loop control using high power hexapole magnetic tweezers for 3d micromanipulation," *Journal of Bionic Engineering,* vol. 17, no. 1, pp. 113-122, 2020.

[42] H. Zhang and K.-K. Liu, "Optical tweezers for single cells," *Journal of the Royal Society interface,* vol. 5, no. 24, pp. 671-690, 2008.

[43] J. R. Moffitt, Y. R. Chemla, S. B. Smith, and C. Bustamante, "Recent advances in optical tweezers," *Annual Review of Biochemistry,* vol. 77, pp. 205-228, 2008.

[44] D. J. Müller, J. B. Heymann, F. Oesterhelt, C. Möller, H. Gaub, G. Büldt, and A. Engel, "Atomic force microscopy of native purple membrane," *Biochimica et Biophysica Acta (BBA)-Bioenergetics,* vol. 1460, no. 1, pp. 27-38, 2000.

[45] G. D. Wright, J. Arlt, W. C. Poon, and N. D. Read, "Optical tweezer micromanipulation of filamentous fungi," *Fungal Genetics and Biology,* vol. 44, no. 1, pp. 1-13, 2007.

[46] M. Sitti and D. S. Wiersma, "Pros and cons: Magnetic versus optical microrobots," *Advanced Materials,* vol. 32, no. 20, p. 1906766, 2020.

[47] A. de Vries, "High force magnetic tweezers for molecular manipulation inside living cells," University of Twente, Enschede, The Netherlands, University of Twente, 2004.

[48] G. Astarita, G. Marrucci, and D. Joseph, "Principles of non-Newtonian fluid mechanics," *Journal of Applied Mechanics,* vol. 42, no. 3, p. 750, 1975.

[49] H. Fu, L. Rogowski, J. Ali, X. Zhang, and M. Kim, "Propulsion of spherical microparticles through spontaneous symmetry breaking in mucus," in *APS Division of Fluid Dynamics Meeting Abstracts*, 2019, p. C35. 003.

[50] Z. Ye, S. Régnier, and M. Sitti, "Rotating magnetic miniature swimming robots with multiple flexible flagella," *IEEE Transactions on Robotics,* vol. 30, no. 1, pp. 3-13, 2013.

[51] U. K. Cheang, H. Kim, D. Milutinović, J. Choi, L. Rogowski, and M. J. Kim, "Feedback control of three-bead achiral robotic microswimmers," in *2015 12th International Conference on Ubiquitous Robots and Ambient Intelligence (URAI)*, 2015, pp. 518-523.

[52] U. K. Cheang and M. J. Kim, "Self-assembly of robotic micro-and nanoswimmers using magnetic nanoparticles," *Journal of Nanoparticle Research,* vol. 17, no. 3, pp. 1-11, 2015.

[53] U. K. Cheang, D. Roy, J. H. Lee, and M. J. Kim, "Fabrication and magnetic control of bacteria-inspired robotic microswimmers," *Applied Physics Letters,* vol. 97, no. 21, p. 213704, 2010.

[54] L. Rogowski, J. Ali, X. Zhang, H. Fu, and M. J. Kim, "Propulsion of microparticles in nonlinearly viscoelastic fluids through symmetry breaking," *Bulletin of the American Physical Society,* 2020.

[55] L. Rogowski, J. Tang, X. Zhang, M. Oxner, and M. J. Kim, "Flagellated Janus particles for swimming and catalytic propulsion," *Bulletin of the American Physical Society,* 2020.

[56] L. W. Rogowski, C. Bubel, X. Zhang, and M. J. Kim, "Innovations in microrobotics and their implications in a digital world," in *Handbook of Digital Innovation*, 2020.

[57] L. W. Rogowski, H. Kim, X. Zhang, S. Sheckman, D. Kim, and M. J. Kim, "Swimming in synthetic mucus," in *2017 14th International Conference on Ubiquitous Robots and Ambient Intelligence (URAI)*, 2017, pp. 512-516.

[58] S. Tottori, L. Zhang, F. Qiu, K. K. Krawczyk, A. Franco‐Obregón, and B. J. Nelson, "Magnetic helical micromachines: fabrication, controlled swimming, and cargo transport," *Advanced Materials*, vol. 24, no. 6, pp. 811-816, 2012.

[59] X. Yan, Q. Zhou, J. Yu, T. Xu, Y. Deng, T. Tang, Q. Feng, L. Bian, Y. Zhang, and A. Ferreira, "Magnetite nanostructured porous hollow helical microswimmers for targeted delivery," *Advanced Functional Materials*, vol. 25, no. 33, pp. 5333-5342, 2015.

[60] J. Tang, L. W. Rogowski, X. Zhang, and M. J. Kim, "Flagellar nanorobot with kinetic behavior investigation and 3D motion," *Nanoscale,* vol. 12, no. 22, pp. 12154-12164, 2020.

[61] L. W. Rogowski, J. Ali, X. Zhang, J. N. Wilking, H. C. Fu, and M. J. Kim, "Symmetry breaking propulsion of magnetic microspheres in nonlinearly viscoelastic fluids," *Nature Communications,* vol. 12, no. 1, pp. 1-11, 2021.

[62] A. Bhattacharjee, L. W. Rogowski, X. Zhang, and M. J. Kim, "Untethered Soft Millirobot with Magnetic Actuation," in *2020 IEEE International Conference on Robotics and Automation (ICRA)*, 2020, pp. 3792-3798.

[63] M. P. Kummer, J. J. Abbott, B. E. Kratochvil, R. Borer, A. Sengul, and B. J. Nelson, "OctoMag: An electromagnetic system for 5-DOF wireless micromanipulation," *IEEE Transactions on Robotics*, vol. 26, no. 6, pp. 1006-1017, 2010.

[64] N. Ribeck and O. A. Saleh, "Multiplexed single-molecule measurements with magnetic tweezers," *Review of Scientific Instruments*, vol. 79, no. 9, p. 094301, 2008.

[65] C.-S. Chen, R.-F. Shiu, Y.-Y. Hsieh, C. Xu, C. I. Vazquez, Y. Cui, I. C. Hsu, A. Quigg, P. H. Santschi, and W.-C. Chin, "Stickiness of extracellular polymeric substances on different surfaces via magnetic tweezers," *Science of The Total Environment*, vol. 757, p. 143766, 2021.

[66] I. De Vlaminck and C. Dekker, "Recent advances in magnetic tweezers," *Annual Review of Biophysics*, vol. 41, pp. 453-472, 2012.

[67] X. Tang, X. Liu, P. Li, D. Liu, M. Kojima, Q. Huang, and T. Arai, "Efficient Single-Cell Mechanical Measurement by Integrating a Cell Arraying Microfluidic Device With Magnetic Tweezer," *IEEE Robotics and Automation Letters*, vol. 6, no. 2, pp. 2978-2984, 2021.

[68] E. Kim, M. Takeuchi, T. Kozuka, T. Nomura, A. Hasegawa, A. Ichikawa, Q. Huang, and T. Fukuda, "Assembly of Multilayered Hepatic Lobule-like Vascular Network by using Heptapole Magnetic Tweezer," in *2019 International Conference on Robotics and Automation (ICRA)*, 2019, pp. 6200-6205.

[69] B. M. Lansdorp, S. J. Tabrizi, A. Dittmore, and O. A. Saleh, "A high-speed magnetic tweezer beyond 10,000 frames per second," *Review of Scientific Instruments,* vol. 84, no. 4, p. 044301, 2013.

[70] E. M. Purcell, "Life at low Reynolds number," *American Journal of Physics,* vol. 45, no. 1, pp. 3-11, 1977.

[71] Z. Zhang and C.-H. Menq, "Design and modeling of a 3-D magnetic actuator for magnetic microbead manipulation," *IEEE/ASME Transactions on Mechatronics,* vol. 16, no. 3, pp. 421-430, 2011.

[72] F. J. Alenghat, B. Fabry, K. Y. Tsai, W. H. Goldmann, and D. E. Ingber, "Analysis of cell mechanics in single vinculin-deficient cells using a magnetic tweezer," *Biochemical and Biophysical Research Communications,* vol. 277, no. 1, pp. 93-99, 2000.

[73] P. Kollmannsberger and B. Fabry, "BaHigh-force magnetic tweezers with force feedback for biological applications," *Review of Scientific Instruments,* vol. 78, no. 11, p. 114301, 2007.

[74] K. Kim and O. A. Saleh, "A high-resolution magnetic tweezer for single-molecule measurements," *Nucleic Acids Research,* vol. 37, no. 20, pp. e136-e136, 2009.

[75] D. Robert, D. Fayol, C. Le Visage, G. Frasca, S. Brule, C. Menager, F. Gazeau, D. Letourneur, and C. Wilhelm, "Magnetic micro-manipulations to probe the local physical properties of porous scaffolds and to confine stem cells," *Biomaterials,* vol. 31, no. 7, pp. 1586-1595, 2010.

[76] L. Chen, A. Offenhäusser, and H.-J. Krause, "Magnetic tweezers with high permeability electromagnets for fast actuation of magnetic beads," *Review of scientific instruments,* vol. 86, no. 4, p. 044701, 2015.

[77] C. Gosse and V. Croquette, "Magnetic tweezers: micromanipulation and force measurement at the molecular level," *Biophysical Journal,* vol. 82, no. 6, pp. 3314-3329, 2002.

[78] L. Chang, M. Howdyshell, W. C. Liao, C. L. Chiang, D. Gallego‐Perez, Z. Yang, W. Lu, J. C. Byrd, N. Muthusamy, and L. J. Lee, "Magnetic tweezers‐based 3D microchannel electroporation for high‐throughput gene transfection in living cells," *Small,* vol. 11, no. 15, pp. 1818-1828, 2015.

[79] A. H. De Vries, B. E. Krenn, R. van Driel, and J. S. Kanger, "Micro magnetic tweezers for nanomanipulation inside live cells," *Biophysical Journal,* vol. 88, no. 3, pp. 2137-2144, 2005.

[80] J. Yan, D. Skoko, and J. F. Marko, "Near-field-magnetic-tweezer manipulation of single DNA molecules," *Physical Review E,* vol. 70, no. 1, p. 011905, 2004.

[81] C.-H. Chiou, Y.-Y. Huang, M.-H. Chiang, H.-H. Lee, and G.-B. Lee, "New magnetic tweezers for investigation of the mechanical properties of single DNA molecules," *Nanotechnology,* vol. 17, no. 5, p. 1217, 2006.

[82] L. Chen, V. Maybeck, A. Offenhäusser, and H.-J. Krause, "Implementation and application of a novel 2D magnetic twisting cytometry based on multi-pole electromagnet," *Review of Scientific Instruments,* vol. 87, no. 6, p. 064301, 2016.

[83] F. Amblard, B. Yurke, A. Pargellis, and S. Leibler, "A magnetic manipulator for studying local rheology and micromechanical properties of biological systems," *Review of Scientific Instruments,* vol. 67, no. 3, pp. 818-827, 1996.

[84] F. Niu, W. Ma, X. Li, H. K. Chu, J. Yang, H. Ji, and D. Sun, "Modeling and development of a magnetically actuated system for micro-particle manipulation," in *14th IEEE International Conference on Nanotechnology*, 2014, pp. 127-130.

[85] Z. Zhang, K. Huang, and C.-H. Menq, "Design, implementation, and force modeling of quadrupole magnetic tweezers," *IEEE/ASME Transactions on Mechatronics*, vol. 15, no. 5, pp. 704-713, 2009.

[86] X. Zhang, H. Kim, L. W. Rogowski, S. Sheckman, and M. JunKim, "Development and Implementation of High Power Hexapole Magnetic Tweezer System for Micromanipulations," in *2018 IEEE International Conference on Robotics and Automation (ICRA)*, 2018, pp. 2670-2675.

[87] F. Long, D. Matsuura, and C.-H. Menq, "Actively controlled hexapole electromagnetic actuating system enabling 3-D force manipulation in aqueous solutions," *IEEE/ASME Transactions on Mechatronics*, vol. 21, no. 3, pp. 1540-1551, 2015.

[88] J. K. Fisher, J. Cribb, K. V. Desai, L. Vicci, B. Wilde, K. Keller, R. M. Taylor, J. Haase, K. Bloom, and E. T. O'Brien, "Thin-foil magnetic force system for high-numerical-aperture microscopy," *Review of Scientific Instruments*, vol. 77, no. 2, p. 023702, 2006.

[89] X. Zhang, L. W. Rogowski, and M. J. Kim, "3D micromanipulation of particle swarm using a hexapole magnetic tweezer," in *2019 IEEE/RSJ International Conference on Intelligent Robots and Systems (IROS)*, 2019.

[90] M. Wu, J. W. Roberts, and M. Buckley, "Three-dimensional fluorescent particle tracking at micron-scale using a single camera," *Experiments in Fluids*, vol. 38, no. 4, pp. 461-465, 2005.

[91] T. H. Boyer, "The force on a magnetic dipole," *American Journal of Physics*, vol. 56, no. 8, pp. 688-692, 1988.

[92] L. W. Rogowski, H. Kim, X. Zhang, and M. J. Kim, "Microsnowman propagation and robotics inside synthetic mucus," in *2018 15th International Conference on Ubiquitous Robots (UR)*, 2018, pp. 5-10.

[93] M. Wu, J. W. Roberts, S. Kim, D. L. Koch, and M. P. DeLisa, "Collective bacterial dynamics revealed using a three-dimensional population-scale defocused particle tracking technique," *Applied and Environmental Microbiology*, vol. 72, no. 7, pp. 4987-4994, 2006.

[94] C. Pacchierotti, L. Meli, F. Chinello, M. Malvezzi, and D. Prattichizzo, "Cutaneous haptic feedback to ensure the stability of robotic teleoperation systems," *The International Journal of Robotics Research*, vol. 34, no. 14, pp. 1773-1787, 2015.

[95] A. M. Okamura, "Methods for haptic feedback in teleoperated robot‐assisted surgery," *Industrial Robot: An International Journal*, vol. 31, no. 6, pp. 499-508, 2004.

[96] A. Bolopion, H. Xie, D. S. Haliyo, and S. Régnier, "Haptic teleoperation for 3-D microassembly of spherical objects," *IEEE/ASME Transactions on Mechatronics*, vol. 17, no. 1, pp. 116-127, 2010.

[97] R. Muradore and P. Fiorini, "A review of bilateral teleoperation algorithms," *Acta Polytechnica Hungarica*, vol. 13, no. 1, pp. 191-208, 2016.

[98] D. Lee, A. Franchi, P. R. Giordano, H. I. Son, and H. H. Bülthoff, "Haptic teleoperation of multiple unmanned aerial vehicles over the internet," in *2011 IEEE International Conference on Robotics and Automation*, 2011, pp. 1341-1347.

[99] J. Park and O. Khatib, "A haptic teleoperation approach based on contact force control," *The International Journal of Robotics Research,* vol. 25, no. 5-6, pp. 575-591, 2006.

[100] S. Lee, G. Sukhatme, G. J. Kim, and C.-M. Park, "Haptic teleoperation of a mobile robot: A user study," *Presence: Teleoperators & Virtual Environments,* vol. 14, no. 3, pp. 345-365, 2005.

[101] M. Tavakoli, A. Aziminejad, R. V. Patel, and M. Moallem, "High-fidelity bilateral teleoperation systems and the effect of multimodal haptics," *IEEE Transactions on Systems, Man, and Cybernetics, Part B (Cybernetics),* vol. 37, no. 6, pp. 1512-1528, 2007.

[102] S. Hirche and M. Buss, "Human-oriented control for haptic teleoperation," *Proceedings of the IEEE,* vol. 100, no. 3, pp. 623-647, 2012.

[103] C. W. Kennedy, T. Hu, J. P. Desai, A. S. Wechsler, and J. Y. Kresh, "A novel approach to robotic cardiac surgery using haptics and vision," *Cardiovascular Engineering: An International Journal,* vol. 2, no. 1, pp. 15-22, 2002.

[104] C. W. Kennedy, T. Hu, and J. P. Desai, "Combining haptic and visual servoing for cardiothoracic surgery," in *Proceedings 2002 IEEE International Conference on Robotics and Automation (Cat. No. 02CH37292)*, 2002, vol. 2, pp. 2106-2111.

[105] S. E. Salcudean, S. Ku, and G. Bell, "Performance measurement in scaled teleoperation for microsurgery," in *CVRMed-MRCAS'97*, 1997, vol. 1205, pp. 789-798.

[106] A. Kazi, "Operator performance in surgical telemanipulation," *Presence: Teleoperators & Virtual Environments,* vol. 10, no. 5, pp. 495-510, 2001.

[107] H. Ding, H. Mitake, and S. Hasegawa, "Continuous collision detection for virtual proxy haptic rendering of deformable triangular mesh models," *IEEE Transactions on Haptics*, vol. 12, no. 4, pp. 624-634, 2019.

[108] A. Pillarisetti, M. Pekarev, A. D. Brooks, and J. P. Desai, "Evaluating the effect of force feedback in cell injection," *IEEE Transactions on Automation Science and Engineering*, vol. 4, no. 3, pp. 322-331, 2007.

[109] A. Ghanbari, B. Horan, S. Nahavandi, X. Chen, and W. Wang, "Haptic microrobotic cell injection system," *IEEE Systems Journal*, vol. 8, no. 2, pp. 371-383, 2012.

[110] C. Pacchierotti, S. Scheggi, D. Prattichizzo, and S. Misra, "Haptic feedback for microrobotics applications: A review," *Frontiers in Robotics and AI*, vol. 3, p. 53, 2016.

[111] C. Pacchierotti, V. Magdanz, M. Medina-Sánchez, O. G. Schmidt, D. Prattichizzo, and S. Misra, "Intuitive control of self-propelled microjets with haptic feedback," *Journal of Micro-bio Robotics*, vol. 10, no. 1, pp. 37-53, 2015.

[112] A. Bolopion and S. Régnier, "A review of haptic feedback teleoperation systems for micromanipulation and microassembly," *IEEE Transactions on Automation Science and Engineering*, vol. 10, no. 3, pp. 496-502, 2013.

[113] C. Pacchierotti, F. Ongaro, F. van den Brink, C. Yoon, D. Prattichizzo, D. H. Gracias, and S. Misra, "Steering and control of miniaturized untethered soft magnetic grippers with haptic assistance," *IEEE transactions on automation science and engineering*, vol. 15, no. 1, pp. 290-306, 2017.

[114] M. Asgari, A. Ghanbari, and S. Nahavandi, "3D particle-based cell modelling for haptic microrobotic cell injection," in *ICMT 2011: Proceedings of the 15th International*

Conference on Mechatronics Technology: Precision Mechatronics for Advanced Manufacturing, Service, and Medical Sectors, 2011, pp. 1-6.

[115] S. Faroque, B. Horan, M. Mortimer, and M. Pangestu, "Towards large-scale haptic virtual reality training for micro-robotic cell injection," in *2016 5th International Conference on Wireless Networks and Embedded Systems (WECON)*, 2016, pp. 1-5.

[116] J. Lee, X. Zhang, C. H. Park, and M. Kim, "Real-time Teleoperation of Magnetic Force-driven Microrobots with 3D Haptic Force Feedback for Micro-navigation and Micro-transportation," *IEEE Robotics and Automation Letters*, vol. 6, no. 2, pp. 1769 - 1776, 2021.

[117] C. H. Park and A. M. Howard, "Real-time haptic rendering and haptic telepresence robotic system for the visually impaired," in *2013 World Haptics Conference (WHC)*, 2013, pp. 229-234.

[118] M. S. Sakar, E. B. Steager, D. H. Kim, M. J. Kim, G. J. Pappas, and V. Kumar, "Single cell manipulation using ferromagnetic composite microtransporters," *Applied Physics Letters*, vol. 96, no. 4, p. 043705, 2010.

[119] M. A. Oskouie and P. Boulanger, "Using proxy haptic for a pointing task in the virtual world: A usability study," in *International Conference on Augmented Reality, Virtual Reality and Computer Graphics*, 2019, vol. 11613, pp. 292-299.

[120] S. Das, E. B. Steager, K. J. Stebe, and V. Kumar, "Simultaneous control of spherical microrobots using catalytic and magnetic actuation," in *2017 International Conference on Manipulation, Automation and Robotics at Small Scales (MARSS)*, 2017, pp. 1-6.

[121] S. Das, E. B. Steager, M. A. Hsieh, K. J. Stebe, and V. Kumar, "Experiments and open-loop control of multiple catalytic microrobots," *Journal of Micro-Bio Robotics,* vol. 14, no. 1, pp. 25-34, 2018.

[122] I. S. Khalil, V. Magdanz, S. Sanchez, O. G. Schmidt, and S. Misra, "Precise localization and control of catalytic Janus micromotors using weak magnetic fields," *International journal of advanced robotic systems,* vol. 12, no. 1, p. 2, 2015.

[123] S. Das, A. Garg, A. I. Campbell, J. Howse, A. Sen, D. Velegol, R. Golestanian, and S. J. Ebbens, "Boundaries can steer active Janus spheres," *Nature communications,* vol. 6, no. 1, pp. 1-10, 2015.

[124] L. Baraban, D. Makarov, R. Streubel, I. Monch, D. Grimm, S. Sanchez, and O. G. Schmidt, "Catalytic Janus motors on microfluidic chip: deterministic motion for targeted cargo delivery," *ACS nano,* vol. 6, no. 4, pp. 3383-3389, 2012.